1998

Assessing sedimentary architecture using ground-penetrating radar : Cretaceous (Albian) Bootlegger Member Blackleaf Formation central Montana

Timothy Ashworth Meckel
The University of Montana

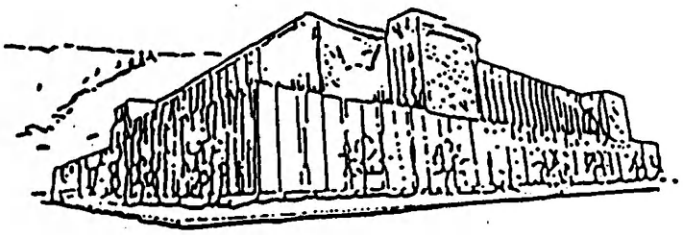

Maureen and Mike
MANSFIELD LIBRARY

The University of **MONTANA**

*** Please check "Yes" or "No" and provide signature ***

Yes, I grant permission X
No, I do not grant permission _____

Author's Signature M Meckel

Date 12/5/98

ASSESSING SEDIMENTARY ARCHITECTURE USING GROUND-PENETRATING RADAR: CRETACEOUS (ALBIAN) BOOTLEGGER MEMBER, BLACKLEAF FORMATION, CENTRAL MONTANA

by

Timothy Ashworth Meckel

B.A., Colby College, 1995

presented in partial fulfillment of the requirements

for the degree of

Master of Science

The University of Montana

1998

Approved by:

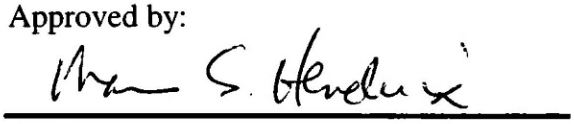

Chairperson

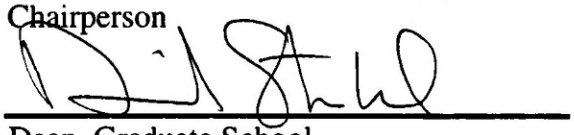

Dean, Graduate School

12-3-98

Date

ProQuest LLC.
789 East Eisenhower Parkway
P.O. Box 1346
Ann Arbor, MI 48106 - 1346

Meckel, Timothy A., M.S., December, 1998 Geology

Assessing Sedimentary Architecture Using Ground-Penetrating Radar: Cretaceous (Albian) Bootlegger Member, Central Montana (123 p.)

Director: Marc S. Hendrix MSH

Small-scale sedimentologic and geophysical investigations of the upper sandstones of the Bootlegger Member of the upper Lower Cretaceous Blackleaf Formation in central Montana provide an opportunity to assess the ability of Ground-penetrating Radar (GPR) to image sedimentary architecture in a consolidated sandstone environment. Previous studies using GPR have focused on its ability to image unconsolidated deposits with sub-meter resolution.

The sedimentologic data was used to characterize the internal architecture of the exposure and to generate a model for the depositional environment. Results from lateral and vertical profiling indicate an internal shingling of identified facies consistent with migration during deposition with some component toward the west. Extensive bioturbation, hummocky cross-stratification (HCS), and paleocurrent data suggest a shallow offshore depositional environment dominated by NW/SE flow conditions. Combined with the facies architecture, these observations suggest that deposition occurred during the northwestward (shoreward) migration of an offshore sand body on the shallow shelf.

Goals of the geophysical work were to illustrate the degree to which GPR can image sedimentary architecture in a consolidated sandstone environment, and to gain an understanding of the causes for reflections. Results from comparisons of the GPR profile with the lateral profile of sedimentary architecture indicate that GPR can image sharp facies contacts within the deposit at the frequency used (50 MHz), but that this frequency can not image with resolution greater than 80 cm. Comparisons of reflection coefficients generated from adjacent permitivity measurements of 15 samples from one vertical profile with changes of petrographic characteristics between the same samples indicate that framework composition correlates most significantly with reflection coefficients. Porosity, percent cementation, and changes in percent saturation characteristics for completely saturated specimens can not be correlated with confidence.

ACKNOWLEDGMENTS

This project could not have taken place without the interest, support, and continual help of Marc Hendrix, my advisor. His patience and efforts to ensure the quality of this work are commendable. I would also like to thank my other committee members, Steve Sherriff and Eijiro Uchimoto, for providing computing facilities, commenting on the manuscript, and their help with various problems I encountered.

Secondly, I owe a debt of gratitude to Bruce Douglass and Indiana University for providing me with an opportunity to use their GPR unit, for housing me at their field station while I practiced, and for continually providing challenging opportunities to test my geologic skills. Appreciation is also given to Montana State Parks and The Department of Natural Resources and Conservation for granting access to the field site chosen for this study. Special thanks are given to the Billings Geophysical Society for awarding me with their annual scholarship, allowing me to continue my education.

Others that I encountered during this project deserve equal thanks, for without their influence I would be a different person. Ever since meeting on a field trip during a week that was arguably too snowy to look at rocks, Don Winston has been my unfailing mentor and friend. Thanks Don, I'll always feel the impact you have made on me, geologically and otherwise. My colleagues, especially Dave Goodwin, Eric Roberts, Mary Beck, and Jeannie Yarnell, also deserve my thanks. Without your support and encouragement I would have been lost from the beginning.

Finally, I'd like to thank my family and loved ones for their support and faith in me. Most importantly, I cannot express the happiness and energy that I have been surrounded with since meeting Amanda Ward. You have provided me with the peace and strength that allows me to be the person I am. Thanks for everything, especially moving to Austin.

Any success I encounter is an indication of the support and guidance I have received over the last 25 years.

TABLE OF CONTENTS

LIST OF FIGURES

CHAPTER 1

Introduction

This thesis presents the results from work in a consolidated sandstone deposit using traditional interpretation methods combined with visualization techniques provided by Ground Penetrating Radar (GPR). As such, it is one of a few similarly guided, recent works that form the basis for understanding of the behavior of ground based radar in consolidated sandstone environments. GPR was originally designed to investigate structural problems associated with the engineering of earthen dams and roads. In the past decade however, geologists have integrated the small-scale resolution afforded by GPR with sedimentary models developed during the twentieth century. It has been most successfully applied to unconsolidated deposits such as modern beaches and spits, illustrating the internal structure of these deposits with long-sought detail (Meyers, 1994; Smith and Jol, 1992b; Jol and others, 1996). Few GPR studies have been conducted in consolidated sandstone environments, but recent work (McMechan and others, 1997) suggests that GPR may be useful for illustrating the internal architecture in these environments with comparable detail. This thesis pursues this topic. With the establishment of literature focusing on the behavior of radar in exposed sandstone deposits, the future utility of GPR techniques for the subsurface analysis of sandstone reservoirs can be determined based on these analogs (McMechan and others, 1997).

This thesis consists of two parallel investigations. Exposures of the Bootlegger at Taft Hill provide an excellent opportunity to document sedimentary architecture using classic mapping techniques and to compare those results to profiles generated with GPR. By acquiring GPR data at the top of the cliff, the GPR signal could be directly compared to an architectural cross-section generated from the outcrop. Such comparison provided the basis for interpretations of the characteristics of the deposit that most significantly affected the GPR response. To facilitate direct comparison between observations of facies on the cliff and GPR imaging of equivalent strata, measurements of the dielectric constant were made on samples from the measured section that displayed the most diverse suite of facies. These measurements allowed reflection coefficients to be

calculated between adjacent specimens for that measured section. Calculated coefficients were compared to the GPR profile and used as a proxy for the reflections seen in the profile. In order to determine possible influences of GPR reflectors near this section, calculated reflection coefficients were then compared to associated changes in petrographic properties of the samples recorded during thin section analysis and the stratigraphy of the measured section. Calculated reflection coefficients, measured stratigraphy, and GPR profile characteristics correlate in an encouraging way. Some radar reflections can be correlated to major bounding surfaces between lithologic facies, and corroborate similar claims made by Stephens (1991) and McMechan and others (1997). Calculated reflection coefficients seem to correlate most significantly with changes in framework composition between adjacent specimens.

Sedimentologic study of the Taft Hill exposure and parallel GPR research are developed in 3 chapters in this thesis. The first chapter presents a sedimentologic analysis of the study area, including facies analysis and interpretation of the origin of internal architecture and depositional environment. The second chapter focuses on the GPR imaging of subsurface equivalents at Taft Hill. Conclusions from the two methods of study are integrated and discussed in the context of previous investigation of these strata in the final chapter.

CHAPTER 2

Sedimentologic Analysis of Taft Hill

2.1 Location of the study area

The rocks investigated in this study are located 15 kilometers west of Great Falls, Montana, in a region named Taft Hill (Figure 1). The exposures crop out along a south-facing bluff that begins in the Ulm Pishkin State Monument and continue west for a little over 1.6 km into land administered by The Department of Natural Resources and Conservation (Figure 2). Permission was granted by both the state monument and DNRC to conduct research on the land. The state monument commemorates a buffalo jump that was used by the Plains Indians at various times over the last few thousand years. Access to the site is possible from Great Falls, Ulm, and Vaughn.

The bluff trends generally N85W, ranges in height from 1-10 meters, and is continuously exposed over the 1.6 kilometer of outcrop used for this study. The top of the exposure is essentially flat. Within 5-10 meters of the cliff, the upper surface of the Bootlegger sandstones is exposed. The Taft Hill site was chosen for study because the vertical cliff face exposure presents an excellent opportunity to document the lateral architecture and sedimentology of the deposit, and the upper surface is ideal for conducting a GPR survey for comparison. There are no trees in the study area, and the only structures that could influence the radar survey are a couple of fences that run perpendicular to the cliff face (Figure 2).

2.2 Geologic setting

The rocks of this study belong to the Bootlegger Member of the Lower Cretaceous Blackleaf Formation (Cobban and others, 1959; Cobban and others, 1976; Figure 3). These marine sediments were deposited in a wide, asymmetric foreland basin developed in central and eastern Montana and flooded by the Cretaceous Interior Seaway

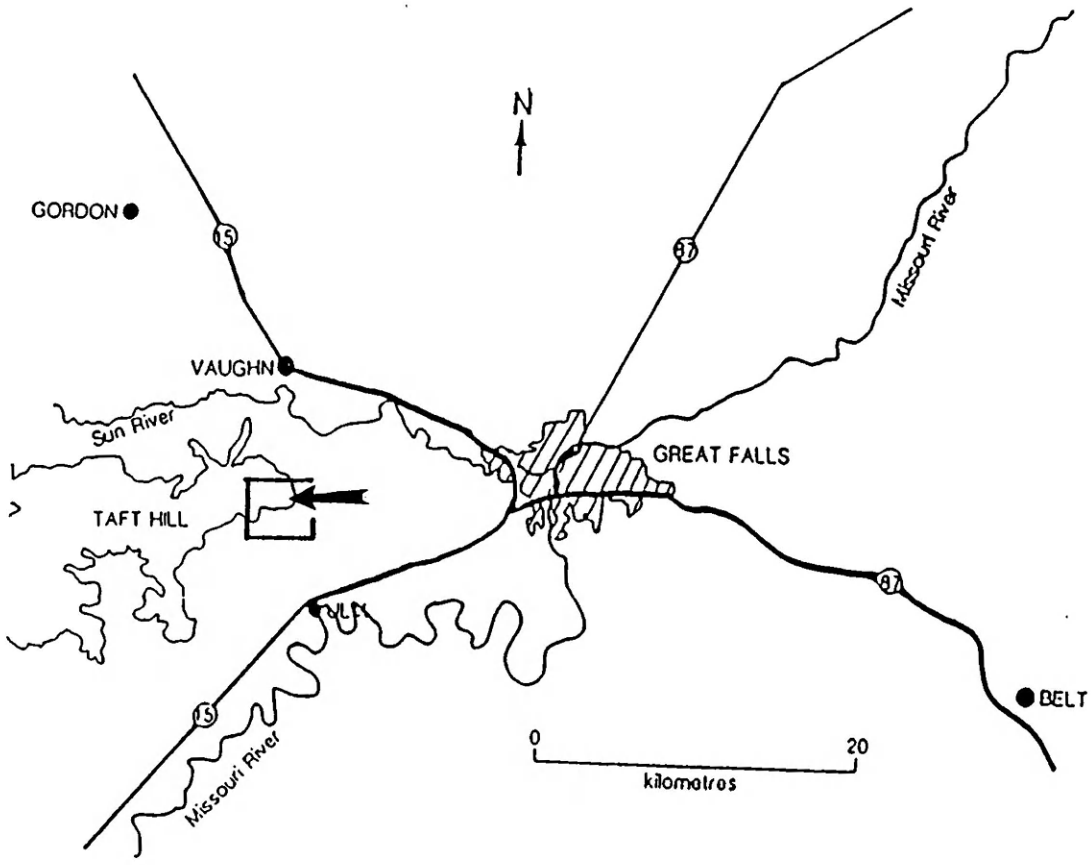

Figure 1: Location of the study area with respect to Great Falls. Arrow indicates the location of the Ulm Pishkin State Park on Taft Hill. Contour line denotes exposures Taft Hill. Box indicates the location of Figure 2. Taken from Arnott, 1987.

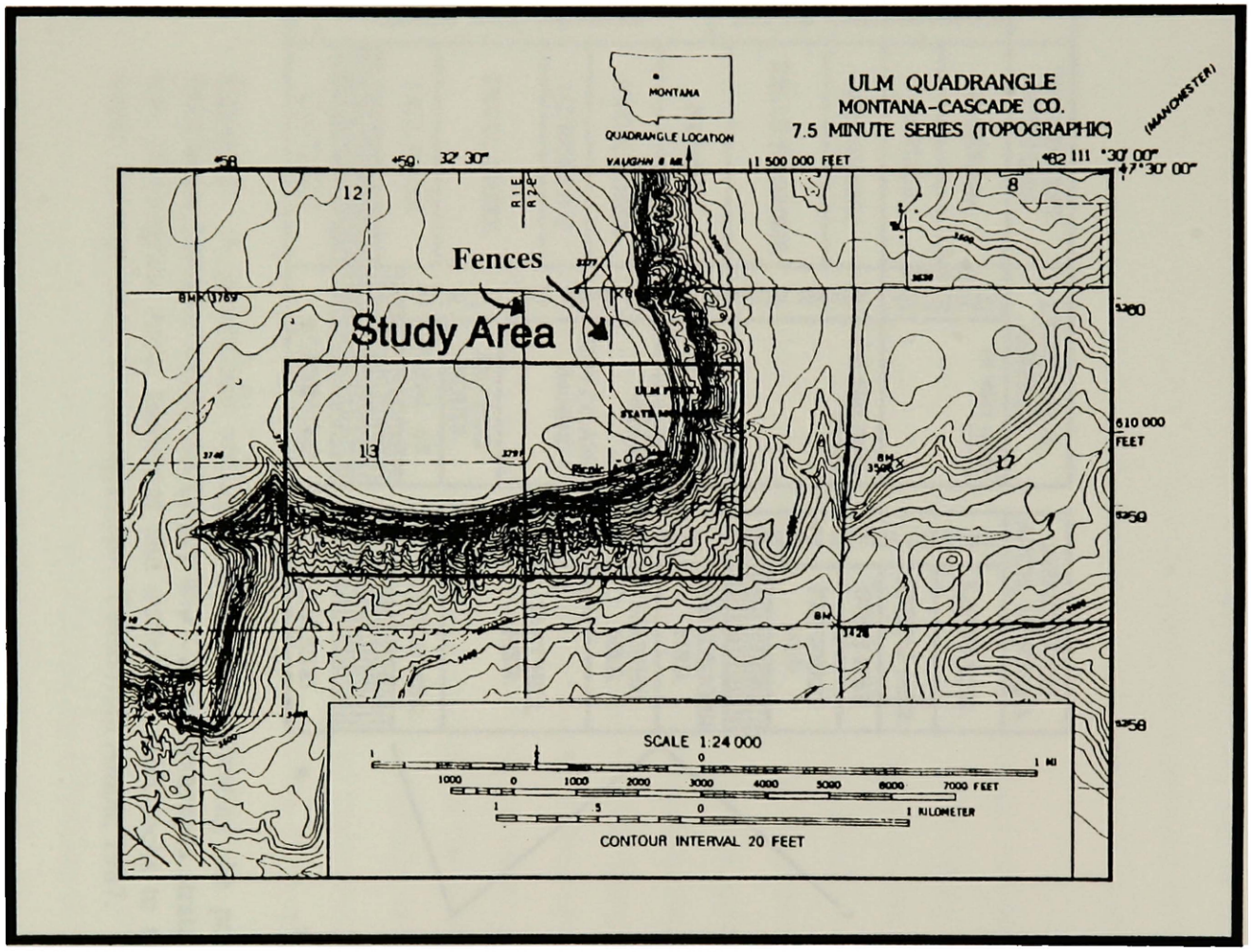

Figure 2: A reproduction of part of the 7.5 minute series topographic map for the Ulm quadrangle, illustrating the borders of the study area.

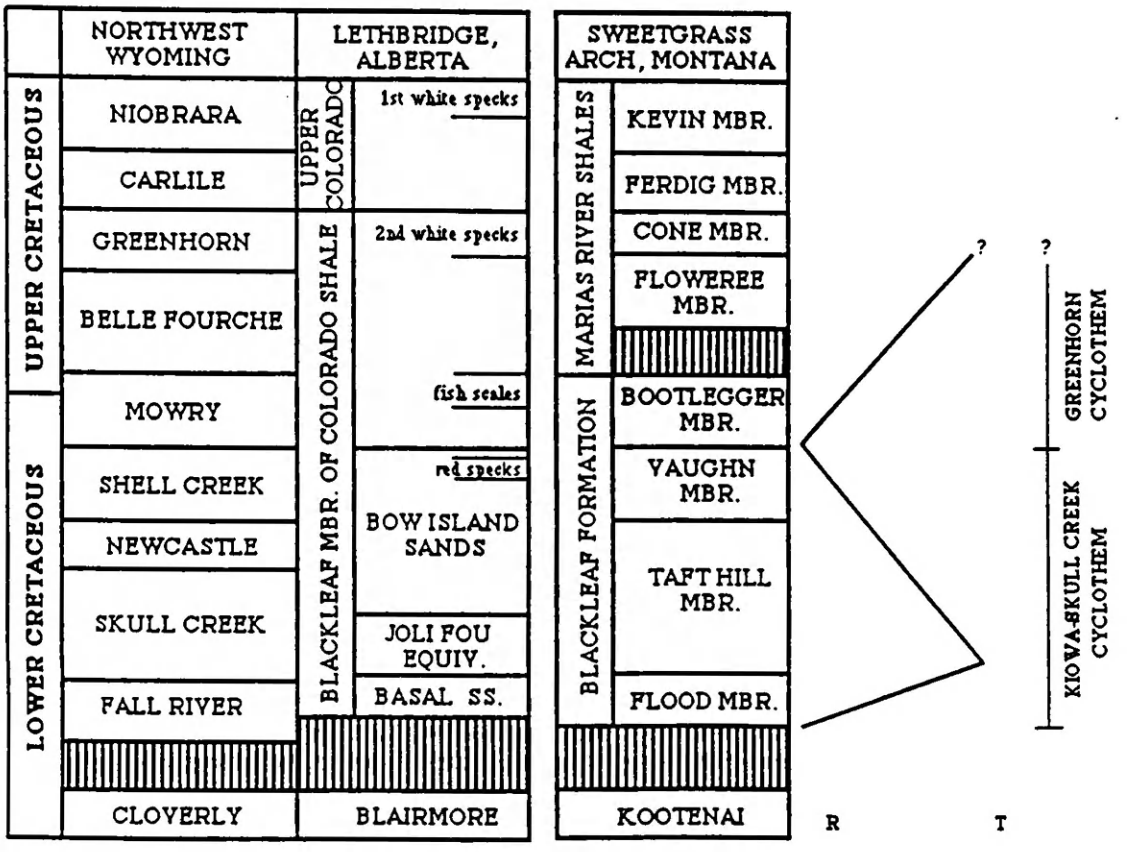

Figure 3: A generalized stratigraphic column indicating the position of the Bootlegger Member within the Lower and Upper Cretaceous strata in the study area (Sweetgrass Arch, Montana) and correlation with rocks to the north and south. R= regression, T= transgression. Taken from Arnott, 1987.

(McMannis, 1965). Deposition occurred between the Fold and Thrust Belt and the southern element of the Sweetgrass Arch (Figure 4).

The Bootlegger Member was deposited between late Albian and early Cenomanian time (Arnott, 1987). The older age constraint is provided by the occurrence of *Neogastropolites americanus*, dated at approximately 96 Ma in the Bootlegger (Folinsbee and others, 1963). The younger age constraint is provided by the Clay Spur bentonite, which occurs at the top of the overlying Mowry shale and is dated at 94 Ma (Folinsbee and others, 1963).

Relative sea level in the Western Interior Seaway changed substantially during this time interval (Haq and others, 1987; Davis and Byers, 1989; Lynch, 1994). The Bootlegger overlies the terrestrial Vaughn Member which represents the Kiowa-Skull Creek regression and underlies the basinal shales of the Floweree Member of the Marias River Formation which represents the transgressive stage of the Greenhorn Cyclothem (Arnott, 1987). In this stratigraphic framework, Arnott (1987) suggested that the Bootlegger records deposition during the initial transgression of the Greenhorn Sea.

The Bootlegger Member consists of five sequences, each being an upward-coarsening package of interbedded very fine sandstone and shale grading upward into fine to medium sandstone and overlain by an erosion surface (Arnott and others, 1995). Arnott and others (1995) suggested that the stacking of these packages is the result of episodic relative changes in sea level that may have been related to reactivation of the ancestral Sweetgrass Arch. Thus, the deposition of the rocks investigated in this study were likely influenced by three principal elements: the development of the fold and thrust belt, relative sea level fluctuations, and the activity of the Sweetgrass Arch.

This study focuses on the uppermost of the five Bootlegger sandstone sequences which is consistently around 10 meters thick in the study area (Figure 5). Regional dip in the study area due to tectonics is negligible. All observed dip of bedding in the study area is attributed to relief that existed during deposition (see section 2.5). The strata studied contain the uppermost portion of a siltstone facies, six overlying sandstone lithofacies, an erosional upper surface, and the overlying siltstone/shale.

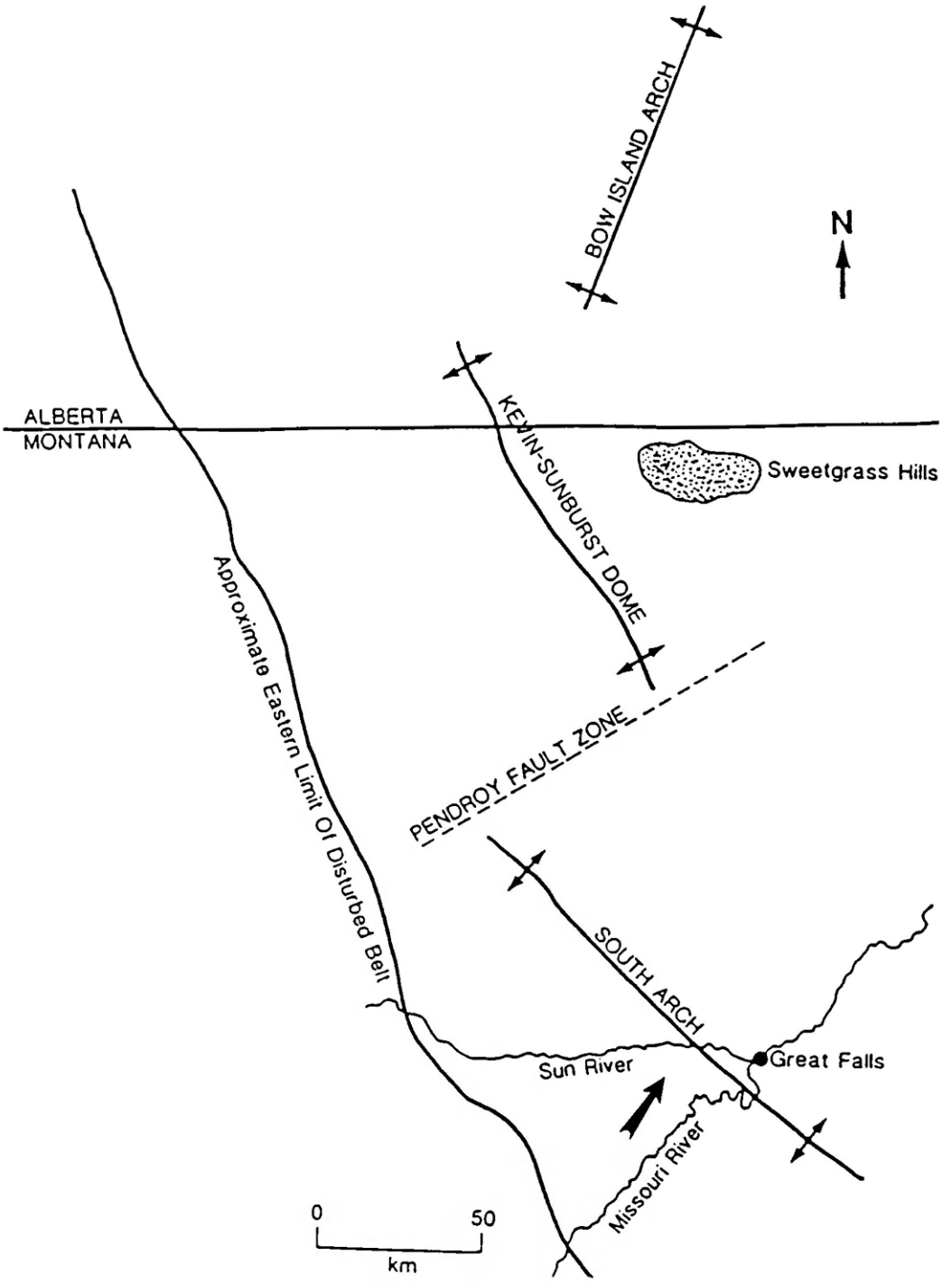

Figure 4: Map indicating the location of the study area with respect to the eastern limit of the fold and thrust belt (disturbed belt) and the Sweetgrass Arch (South Arch). Tip of arrow between the rivers indicates the approximate location of the field site. Taken from Arnott (1987).

Figure 5: Photograph illustrating the nature of the exposure of the rocks used for this study. The photograph is of the western part of the study area, taken from a helicopter looking east. Note the continuous exposure and flat upper surface, where the radar profile was collected.

2.3 Sedimentary Methods

This study focuses on several different sedimentary characteristics of the rocks in the study area. These include the lateral and vertical architecture, sedimentary and biogenic structures, grain size, paleofow indicators, framework grain composition, and sandstone porosity. Techniques used include facies mapping on a photo-mosaic-base, documentation of sedimentology in regularly-spaced stratigraphic sections, and optical thin section analyses. These techniques and the goals of the work are described below.

Facies architecture in the exposed cliff face was mapped in order to document structures that might be recorded by GPR and to aid in the interpretation of the depositional environment. A photo-mosaic was compiled from photographs taken from a helicopter and used to map prominent surfaces and individual beds throughout the bluff. This method was used to minimize distortion caused by photographic pans taken from the ground (Miall and Tyler, 1991). The prints were then prepared for field use by mounting adjacent photos on foam boards and by covering them with an acetate overlay. In the field, surfaces were mapped on the overlay. Features recorded on the photo-mosaic were approximately the same scale as the theoretical resolution of the GPR using 50 MHz antennae (i.e. 0.5 - 1m; Meyers, 1994). The only problem encountered during the photo-mosaic work was in some localities where the outcrop steps out or back several meters. In these localities some surfaces were difficult to carry smoothly on the overlay. Dashed lines were used wherever surfaces become difficult to correlate.

Measured sections were made to specifically document the vertical stratigraphy at numerous locations along the exposure to serve as control points for the radar profile and to aid in the recognition and distribution of different facies. Ten vertical sections (A-J) were used to document the stratigraphy at specific locations along the cliff (Figure 6). These profiles were measured with a tape measure hung from the top of the exposure. Each vertical profile was measured with five centimeter resolution. Documented sedimentologic attributes included grain size and composition, sedimentary structures, bedding characteristics, trace fossils, paleoflow indicators, and lithology. On profiles that exhibited transitions between multiple facies, samples were collected at 50 cm intervals.

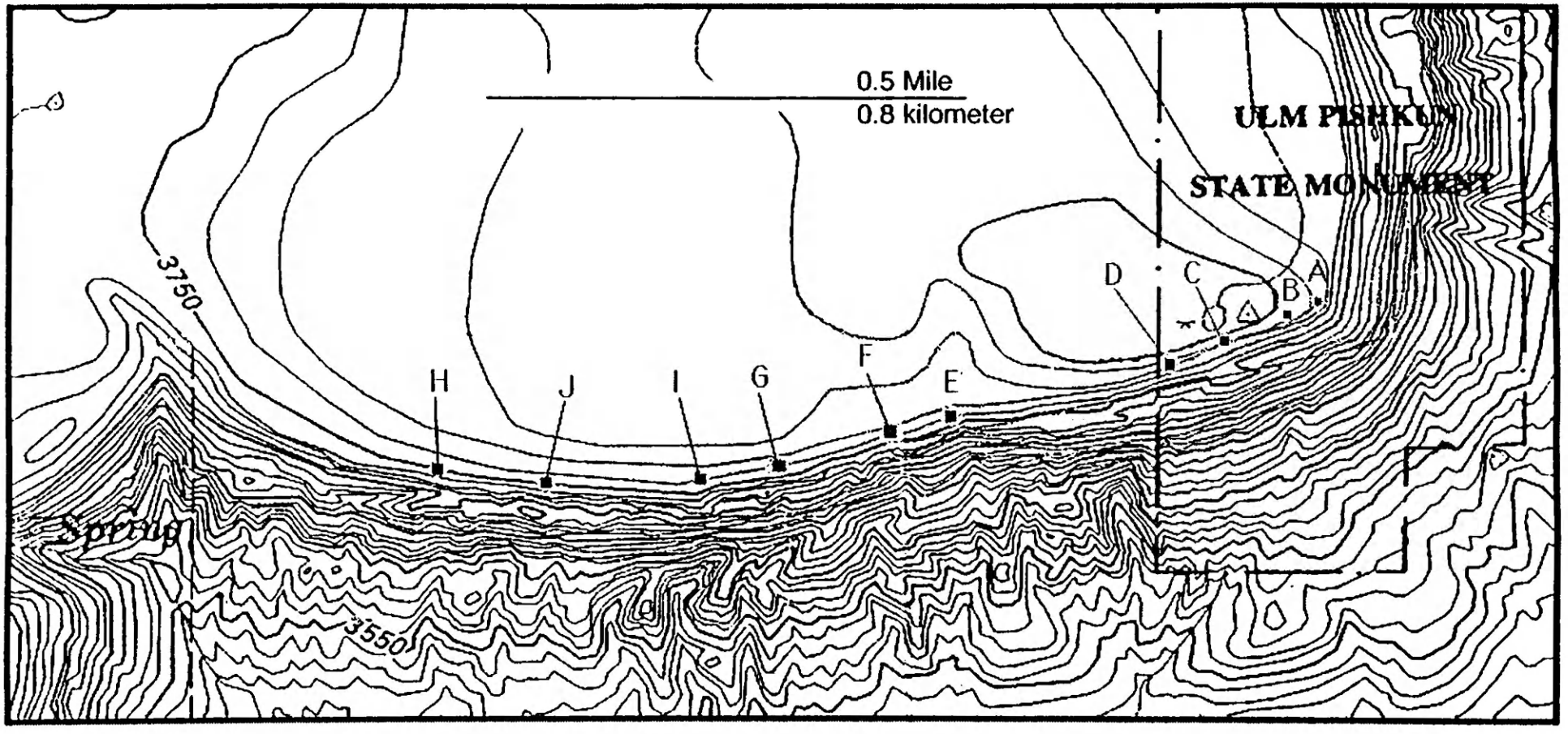

Figure 6: This map shows the location of the measured sections A through J. Note that Sections I and J are out of sequence. The stratigraphy of the measured sections can be found in Plate 1.

In order to document potential petrographic characteristics that may have been related to radar reflections, 15 samples from measured section G were used for petrographic analysis (Figure 7). Section G was chosen because it contained the most facies changes and interesting architecture. Cost considerations limited the number of samples submitted for analyses to those samples from Section G only. Work on these thin sections focused on composition, amount of cement, grain size, and porosity. Point counts were performed on all 15 slides. The mineral composition of 500 framework grains was recorded for each slide. The slides were stained for potassium feldspar and calcite to facilitate compositional determinations. Porosity estimates were made on each slide with the aid of blue epoxy impregnation. Porosity was counted separately and used to estimate the percent porosity for each slide.

2.4 Results from the sedimentary investigation

2.4.1 Introduction

In this section, I first describe the facies upon which my larger scale mapping of facies architecture rests. Subsequently, I present an interpretation of the depositional environment based on these facies descriptions and architectural mapping, and I compare these interpretations with previous analyses of these rocks.

2.4.2 Upper Bootlegger facies at the Ulm Pishkin site

Siltstone facies: This facies is a light greenish-gray to light gray on fresh surfaces but weathers tan and in blocky fashion. This facies is finely laminated, muddy and bentonitic with traces of biotite. The siltstone facies crops out both as a recessive interval below the Taft Hill cliff-forming sandstones, and at the top of the bluff, where it is typically vegetated. No trace fossils were observed in 5 locations where this facies was identified, though the crumbly nature of the facies precluded the examination of cut slabs or X radiography. Siltstone facies stratigraphically below the study rocks, and other related deposits described by Arnott (1987), exhibited the trace fossil *Teichichnus*. Only the uppermost meter where the

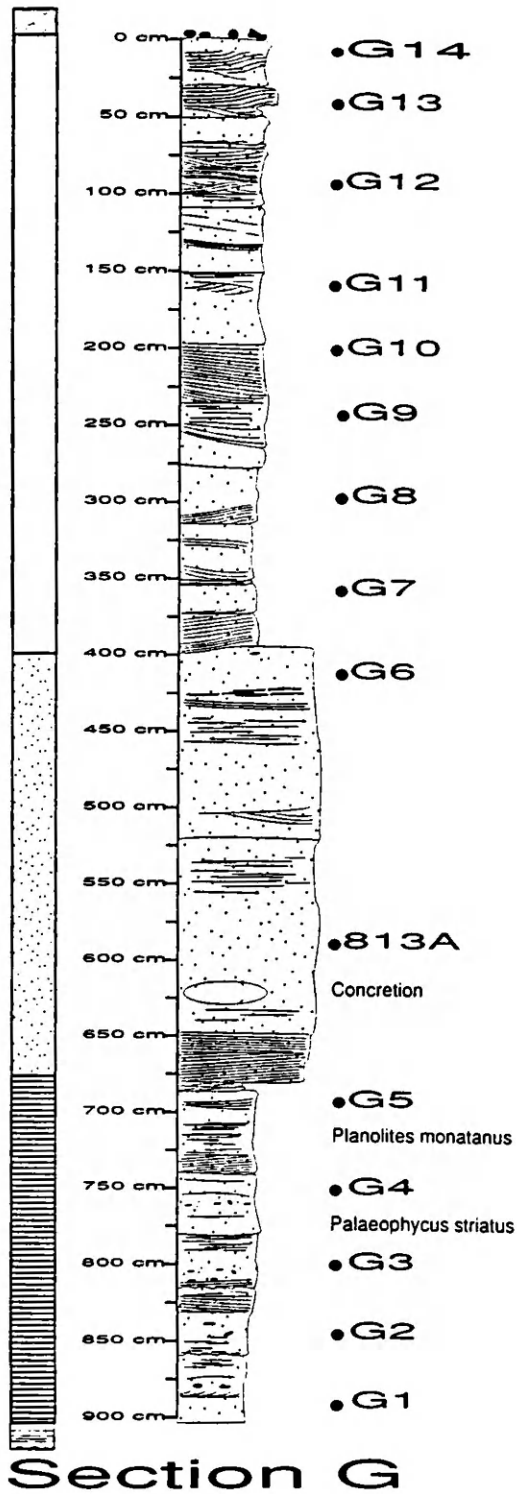

Figure 7: The location of the 15 samples from Section G used for petrographic and petrophysical analyses. The meaning of the symbols can be found in Plate 1.

Siltstone facies is in contact with the overlying sandstone facies at the base of the bluff was examined closely in this study (Figure 8). Bedding is apparently horizontal in this facies.

Trace fossils: No trace fossils were observed in this facies in this study, but see Arnott (1987).

Interpretation: This facies represents shallow offshore, shelfal deposition, with suspension fallout being the primary mode of deposition. Arnott (1993) reported that micropaleontologic data from the lower and upper shales at Taft Hill indicate deposition in an open marine environment. This facies corresponds to Lithofacies 1 of Arnott and others (1995).

Pinch and Swell Sandstone facies: This facies is dominated by grayish-tan to light-tan, lower-coarse to lower-medium, moderately-well to well-sorted quartz sandstone. In places, bedding ranges from 10-50 cm thick, is generally massive and laterally continuous on a meter scale. Sandstone beds contain internal scour and amalgamation surfaces with locally preserved ripples (Figure 9), and are extensively grazed (Figure 10), showing traces on lower contacts of many of the beds. Hummocky Cross Stratification (HCS) (deemed Quasi-Planar Laminated sandstone by Arnott, and others, 1995; Arnott, 1993) is common to abundant in the thicker sand bodies. Strong grading is absent in these beds. 5-10 cm wide gutters oriented NW/SE are present. Millimeter-scale lamination is common, with low angle (<10 degrees) truncation of laminae common. Locally, this facies includes trough-cross-bedding with 10-30 cm of relief. Mud rip-up clasts up to 7 cm are common in the lower portions of the troughs. Bi-directional, cm-scale cross-sets (similar to herringbone structures) were observed in Section A.

The Pinch and Swell Sandstone facies erosionally overlies the Siltstone facies, and the contact is sharp and erosive. West of section A, beds immediately above the basal contact are hummocky cross-stratified, contain fewer intraclasts, and are not cross bedded. Throughout this facies, the more massive beds of the lower trough cross-beds pass into 5-10 cm scale thickening and thinning (pinch

Figure 8: Photograph of the Siltstone facies in contact with the overlying Pinch and Swell Sandstone facies in the eastern part of the study area. Hammer for scale.

Figure 9: Photograph illustrating the bedding style characteristic of the Pinch and Swell Sandstone facies. Ruler is 17 cm long.

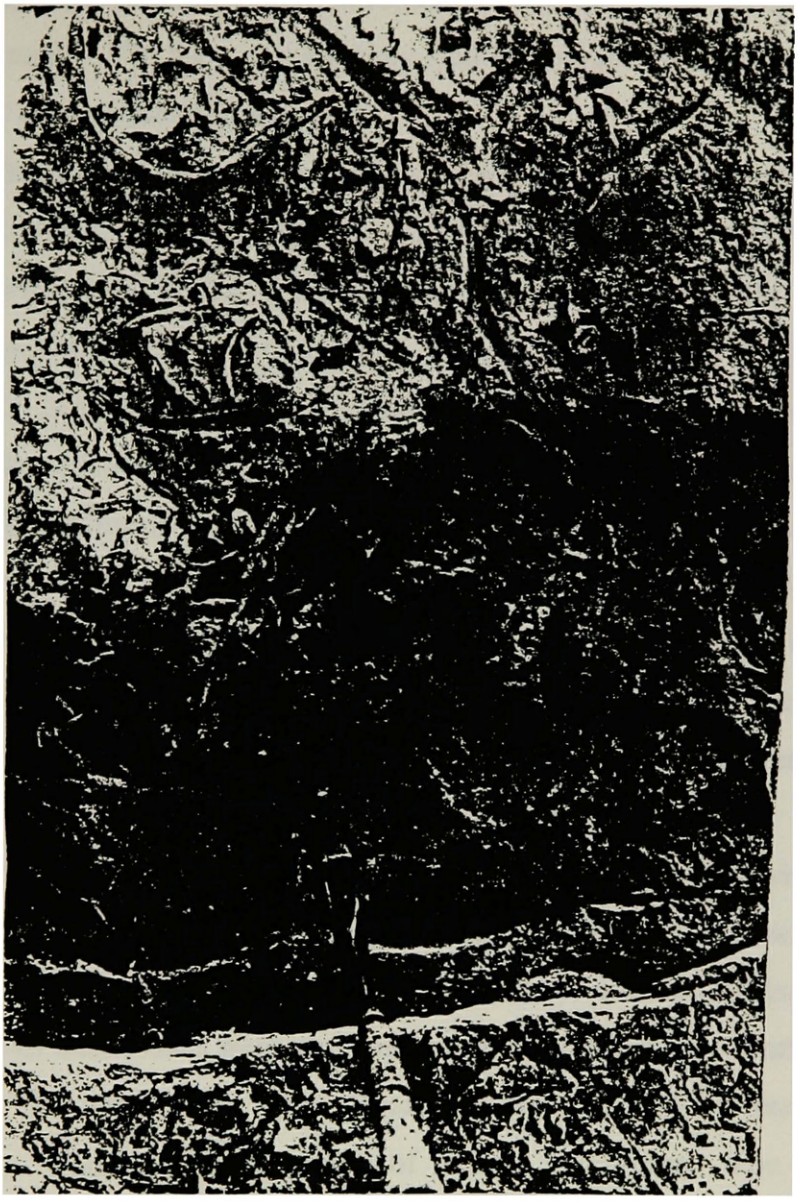

Figure 10: View of horizontal grazing traces on the base of a sandstone bed in the Pinch and Swell Sandstone facies. Hammer for scale.

and swell) beds of medium sand, alternating with millimeter- to centimeter-scale silts and muds. The tops of these beds typically exhibit 3-D, asymmetric ripples with 5-10 cm spacing (Figure 11).

The upper beds in this facies are generally 1-10 centimeters thick, and laterally become more discontinuous. Small channels oriented NW/SE are locally present throughout this facies and are usually 1-4 meters in width. Asymmetric ripples (stoss:6,8,5 cm; lee1.5,1,1 cm), occasional symmetric ripples (stoss 4.5 cm, lee 4.5 cm), 1 to 10 centimeter cross-sets, and mud clasts are all common.

The contact with the overlying Low Angle Cross-bedded to Planar Laminated Sandstone facies is gradational over a 2-4 meter interval, as tabular-planar and trough cross-beds become more prevalent. The total thickness of the Pinch and Swell Sandstone facies varies but is around 15 meters. This thickness is estimated to be larger than the overall height of the exposure because it dips around 3 degrees to the west. In addition, this facies thins to the west to around 2 meters.

Trace Fossils: Bioturbation consists dominantly of horizontal grazing, with occasional vertical, pencil-thick burrows (Figure 12). *Lockeia, Planolites, Baguaria, Monocraterion, Skolithos, Ophiomorpha, Arenicolites,* and *Palaeophycus* are present. All trace fossils were identified using descriptions by Arnott (1987).

Interpretation: The Pinch and Swell Sandstone facies seems to record episodic deposition, with intervening periods of relative quiescence. The lower trough cross-beds with mud rip-ups, ripples, grazing, and HCS all suggest deposition in a shallow offshore environment. Storm reworking of sediment was likely common, with intervening, quieter periods recorded by thin, muddy siltstone inter-beds. Pulses of sedimentation, as illustrated by a bioturbated sandstone sharply separated from a non-bioturbated sandstone by an amalgamation surface, removed some sand and overlying mud deposited during periods of minimal current activity. The dip of the facies is attributed to topographic relief in the depositional environment, and not to tectonic tilt. This interpretation is based on the occurrence of this facies between the Siltstone facies and the Chert Pebble facies,

Figure 11: Upper surface of a sandstone bed in the Pinch and Swell Sandstone facies illustrating unidirectional ripples. The paleoflow direction is to the northwest (lower left of photograph). Ruler is 17 cm long.

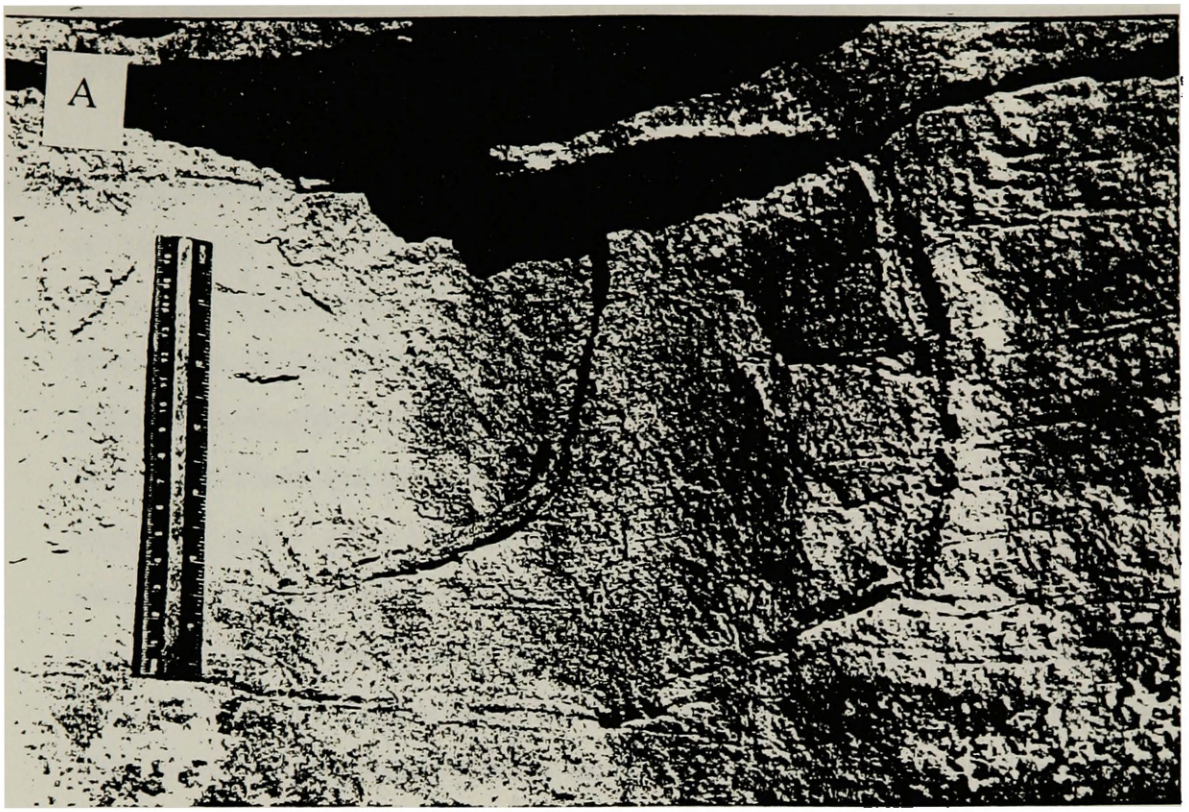

Figure 12: Vertical burrows (A) and bedding plane traces (B) seen in the Pinch and Swell Sandstone facies. Ruler is 17 cm long.

both of which are horizontal. The Pinch and Swell Sandstone facies corresponds to Lithofacies 2 of with Arnott and others (1995).

Low Angle Cross-bedded to Planar Laminated Sandstone facies: The main characteristic of this facies is the gradual domination of cm-scale beds that exist in sub-horizontal, tabular-planar to tabular-tangential, and trough cross-set packages of beds which are individually 0.5-5 cm, but up to 30 cm in thickness (Figure 13). These cross-stratified beds are commonly less continuous than the underlying beds in the Pinch and Swell Sandstone facies. Ripples are sparse, although 3-D ripples are preserved on the tops of some truncated foresets. Mud intraclasts are uncommon, are typically 1-10 cm (avg=3 cm) when present, and occur both at the toes of the foresets and scattered throughout the facies. Foreset toe angles average around 10 degrees. Upper plane bed lamination is also common in this facies. This facies is transitional between the Pinch and Swell Sandstone facies and Massive Sandstone facies. The contact with underlying Pinch and Swell Sandstone facies is gradational over a distance up to 4 m (seen best in Section E), with a gradual change from horizontal pinch and swell beds into planar tabular-planar and trough cross-stratified beds. Accompanying this transition is a definite decrease in the degree of bioturbation, especially in the abundance of vertical burrows. Above the contact with the underlying Pinch and Swell Sandstone facies, this facies does contain intervals of pinch and swell beds, but in general the bed-sets become thicker (20-50 cm) with fewer silty breaks. The most noticeable change accompanying the transition between facies is the decrease of bioturbation, specifically *Ophiomorpha* burrows and the domination of less continuous trough cross-stratified beds. This facies is estimated to be around 3 meters thick, but thins to the west to around 1 meter. This facies was seen in contact with the overlying Massive Sandstone facies and underlying Pinch and Swell Sandstone facies in all locations, although the lateral variability of all facies makes this determination difficult in places. Mapping of this facies indicates it dips to the west.

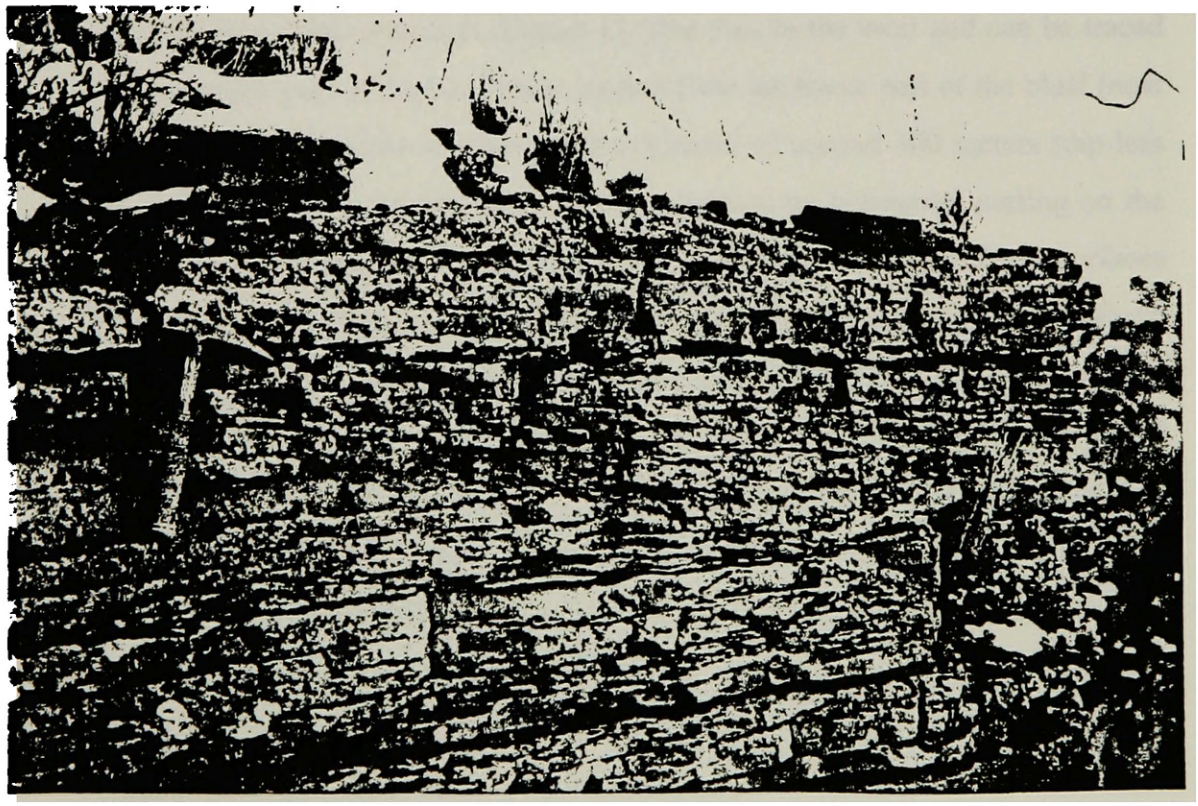

Figure 13: Representative views of the Low Angle Cross-bedded to Planar Laminated Sandstone facies, as seen near measured section E. Note cross-bedding characteristics. Hammer for scale.

Trace Fossils: *Palaeophycus, Skolithos, Lockeia,* and *Planolites* are present.

Interpretation: I interpret this to be a higher energy facies than the underlying Pinch and Swell facies. Maximum energy conditions are illustrated by the tabular and trough cross-beds, occasional large (up to 6 cm) mud clasts, and upper plane bed lamination. Minimum energy is recorded by local ripples and finer grained, suspension fallout layers. This environment still seems to be characterized by episodic sedimentation, but the less well established infauna makes this more difficult to demonstrate than in the underlying facies. The sedimentation events in this environment appear to record higher energy than the underlying layers, consistent with shallower depths and the lack of abundant grazing traces. This facies corresponds to Lithofacies 3 of Arnott and others (1995).

Massive Sandstone facies: This facies is a massive, upper-fine to lower-medium, moderately- to well-sorted sandstone, with planar to slightly undulating and low-angle truncated laminae (HCS; Figure 14). It exists primarily as a 2-3 meter thick, conspicuously continuous unit (Figure 15) that dips to the west and can be traced from the upper part of the bluff (near section F) to the lower part of the bluff (near Section G; 10-15 meters of relief) over a distance of around 300 meters (dip less than 3 degrees; Plate 2). The facies is characterized by horizontal parting on the mm to cm scale that is accentuated by weathering. Amalgamation surfaces ranging from 5 to 30 cm apart vertically and are continuous from 50 to 400 cm laterally. Finer grained interbeds are absent, and little bioturbation is preserved. In one measured section (Section G) this unit contains a concretion 2 meters in diameter. The top of this unit is locally scoured by 25 cm troughs that contain mud clasts up to 6 cm. This facies is not apparently described by Arnott and others (1995), perhaps because their more regional study did not find this facies to be common enough to warrant description.

Trace Fossils: *Planolites* and *Paleophycus* were observed on the base of the lowermost contact. No others were identified within the massive sand.

Interpretation: This unit is an anomaly introduced within an apparently shoaling upward

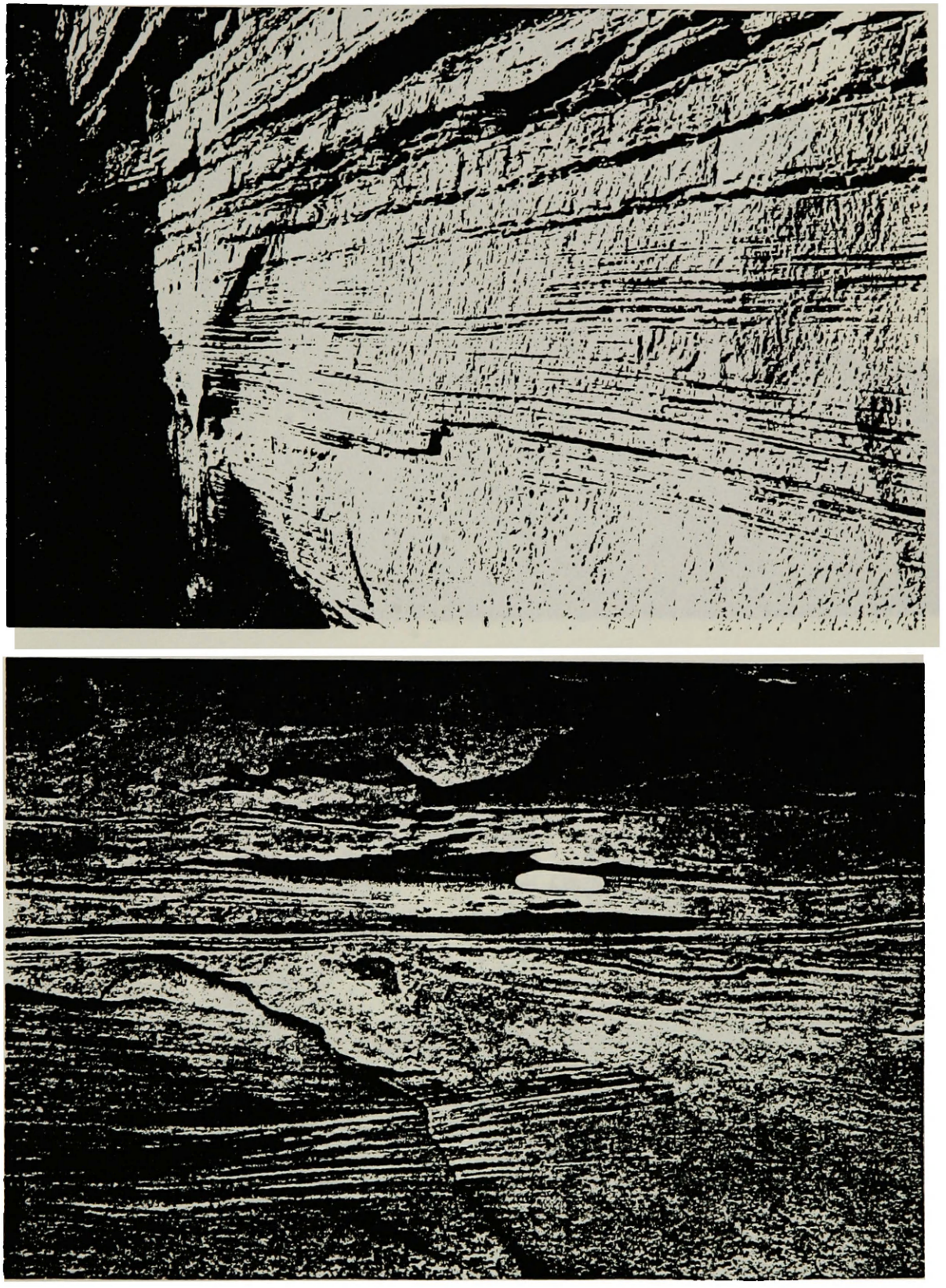

Figure 14: Views of Hummocky Cross-stratification (HCS) in the Massive Sandstone facies. Right margin of upper photograph is approximately 2 meters. Knife for scale in lower photograph.

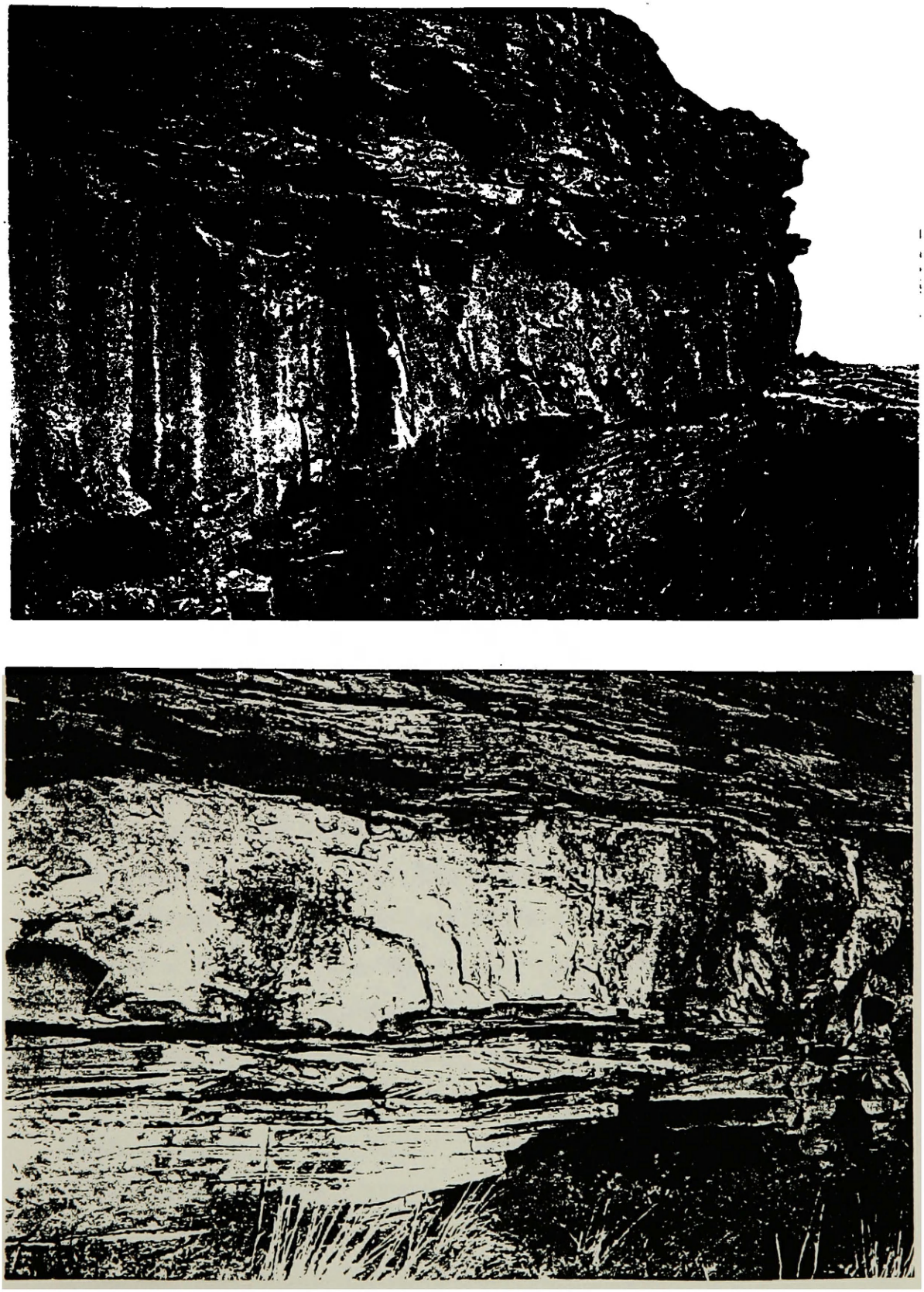

Figure 15: Views of the Massive Sandstone facies (~ 2 m thick) taken just east of measured section G. Note the constant thickness and massive appearance.

sequence. The amalgamation surfaces, upper plane beds, and hummocky cross-stratification are suggestive of storm deposition. Lack of significant bioturbation indicates a more energetic depositional system as well. In reviewed literature, few similar beds are described as part of modern or ancient shoreface depositional environments. Thus, this facies is difficult to integrate into current depositional models without invoking abnormal deposition. Rather, I interpret this facies as recording a single event and subsequent reworking of a washover fan in an offshore bar (Boyles and Scott (1982) and Brenner (1978); Figure 16). In a storm event, it is proposed that the uppermost topography of the sand bar was breached by westward-shoaling waves, allowing deposition on the shoreward side of the bar.

Muddy Trough Cross-stratified Sandstone facies: This facies lies above the Massive Sandstone facies in succession, and locally is scoured up to 3 meters into the underlying Massive Sandstone facies. It is dominated by troughs with abundant mud intraclasts in the toes of the cross-sets (Figure 17), although mud clasts may be localized and not found in all locations. These cross-beds are distinct from the Low Angle Cross-bedded to Planar Stratified Sandstone facies in that they generally contain more abundant mud rip-ups. Bedding is usually 20-60 cm thick with partings at 1 to 10 cm scale. Ripple preservation is moderate, with common 3-D, dominantly asymmetric (NW and SE flow direction) ripples with spacing on the order of 10-15 cm. Local fining upward sequences were observed over 5-15 cm intervals. This facies is dominated by amalgamation surfaces.

Trace Fossils: Bioturbation is present but not abundant, with notable *Scolicia* resting traces and local horizontal *Ophiomorpha* burrows. Other trace fossils identified include *Planolites,* and *Paleophycus.* Grazing and resting trace fossils are more common in this facies than burrowing traces.

Interpretation: The troughs and abundance of mud intraclasts are key to the interpretation of this unit. Deposition in this facies seems to record more storm influence than in underlying facies. The greater abundance of intraclasts and amalgamation

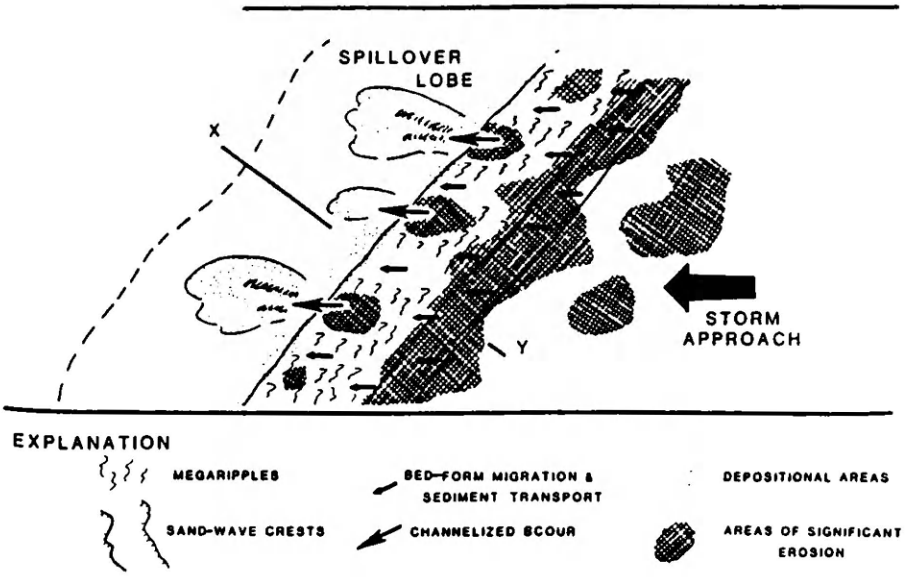

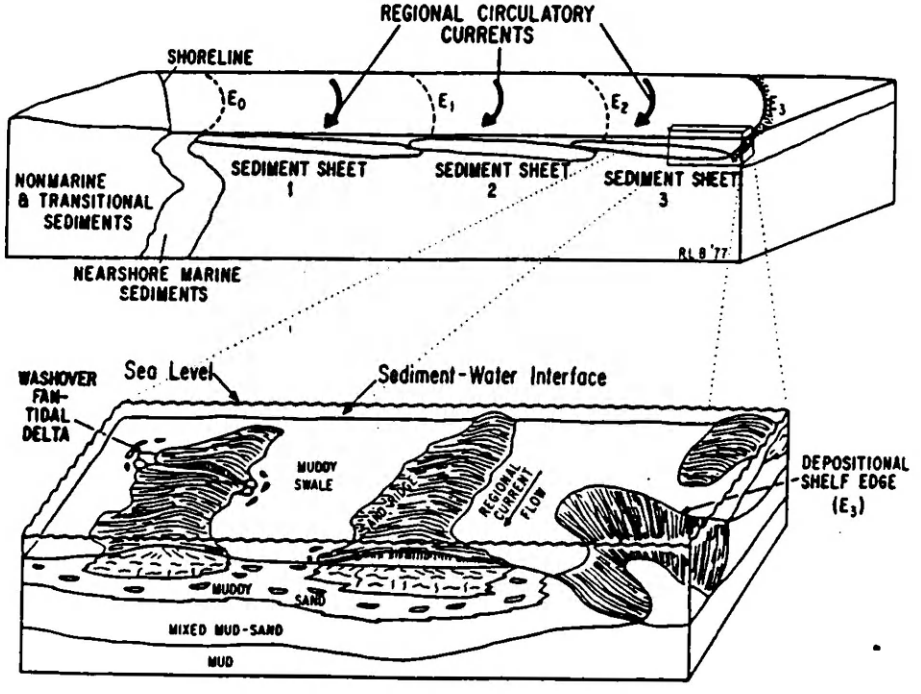

Figure 16: Diagrams from Boyles and Scott (1982) (upper figure) and Brenner (1978) (lower figure) illustrating the concept of a washover fan in an offshore sand body setting.

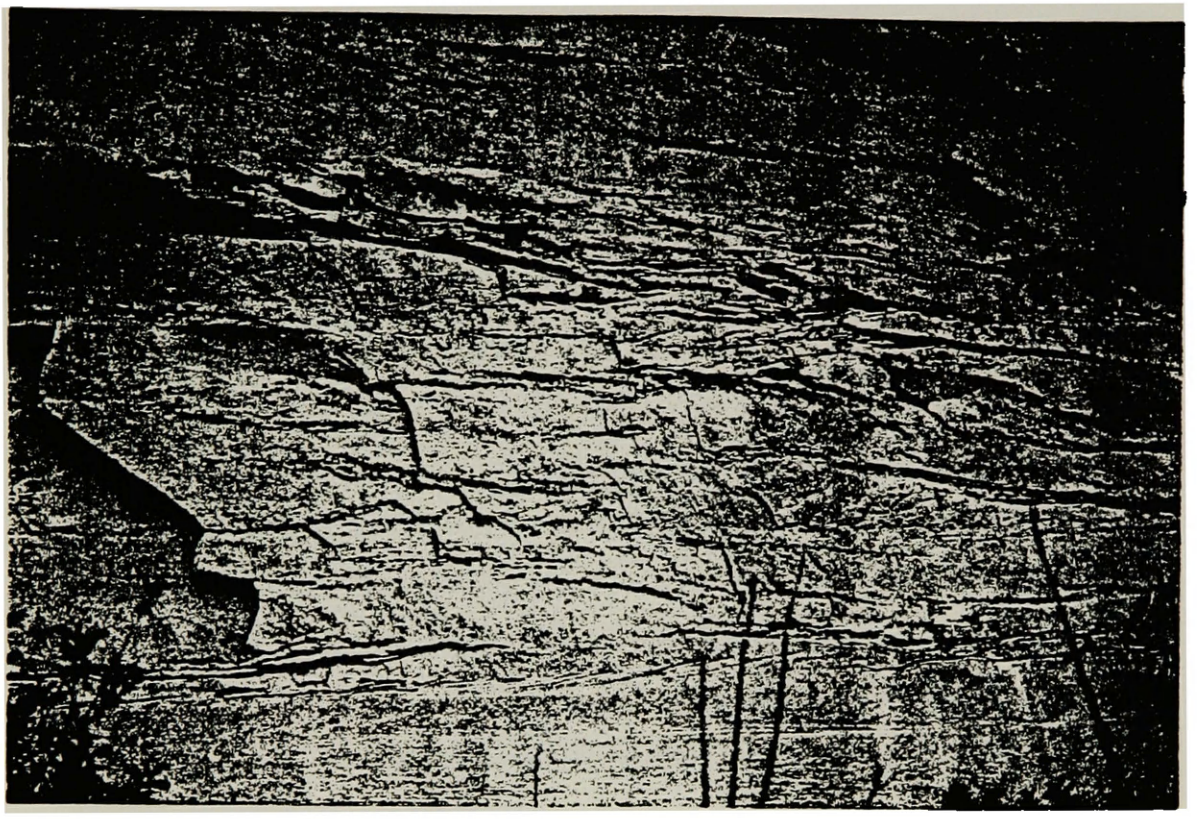

Figure 17: View of typical beds in the Muddy Trough Cross-stratified Sandstone facies. The mud clasts tend to weather recessively, leaving voids in the toes of the cross-sets. Height of the photograph is around 3 meters.

surfaces in this facies support this interpretation. This facies may indicate a shallower environment than the underlying facies, well within the reach of storm wave base. This facies corresponds to Lithofacies 4 of Arnott and others (1995).

Tabular Bedded Sandstone facies: This facies is noted for pseudo-tabular, blocky weathering 1-5 cm scale beds that are clearly more laterally extensive (greater than 5 meters commonly; Figure 18) than the underlying Muddy Trough Cross-Stratified facies. Upper surfaces of the beds are generally planar, lacking significant ripples. Parting lineation oriented NW/SE is common throughout this facies. Sets of these beds occur as 30-50 cm packages, some of which have low angle (<3 degree) dip with components both to the west and east, neither apparently more dominant. Unidirectional 3-D ripples on the top of the bluff that are included in this facies (Figure 19) have a paleoflow direction to the northwest (or apparently landward). Bioturbation is noticeably lacking in these beds. This unit was measured (Section H) to be 2.2 meters thick, although it was likely somewhat thicker, having been partially eroded. This facies continues to the west beyond the border of the study area.

Trace Fossils: Apparently none.

Interpretation: This unit has characteristics similar to foreshore deposits such as parallel lamination at low angle, thin bedding, little bioturbation, and lateral continuity of bedforms. I do not interpret these beds to represent the swash zone environment proposed by Arnott, and others (1995) due to the overall geometry of all the facies in the study area (Figure 20). I disagree with this interpretation based on the overall westward-dipping facies geometry in the deposit and the fact that not all parallel laminated sands are produced in a shoreface environment. The internal geometry of the facies indicates that these beds were not deposited on an eastward dipping surface, as one would expect on a shoreface migrating eastward (Vail and others, 1977). Rather, I interpret this facies as recording the upper portion of a migrating sand bar. The parallel lamination may have been generated from upper plane bed flow generated by storms (Reineck and Singh, 1972), and can be

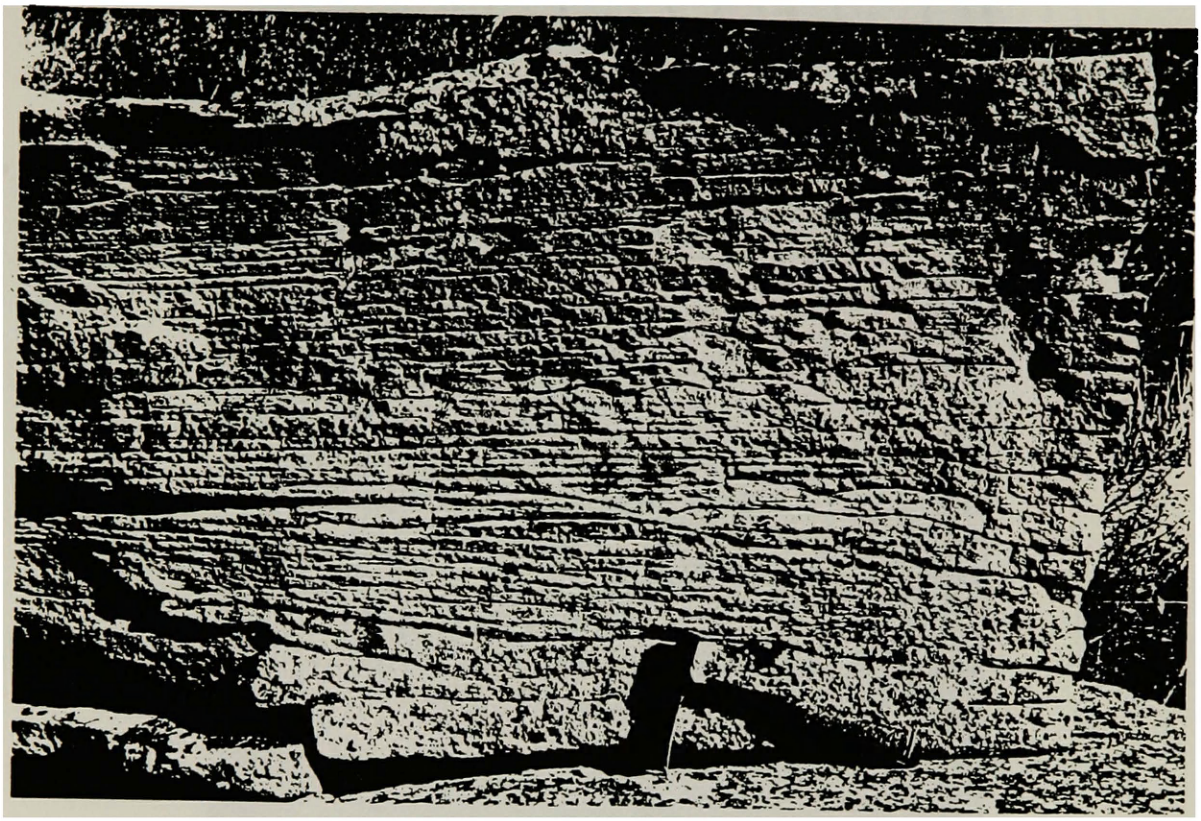

Figure 18: Photograph of the Tabular Bedded Sandstone facies as it appears near the top of measured section H. Note the thin and relatively continuous bedding with no silty interlayers.

Figure 19: Unidirectional 3-D ripples from the Tabular Bedded Sandstone facies illustrating paleoflow to the northwest (lower left in photograph). Ruler is 17 cm long.

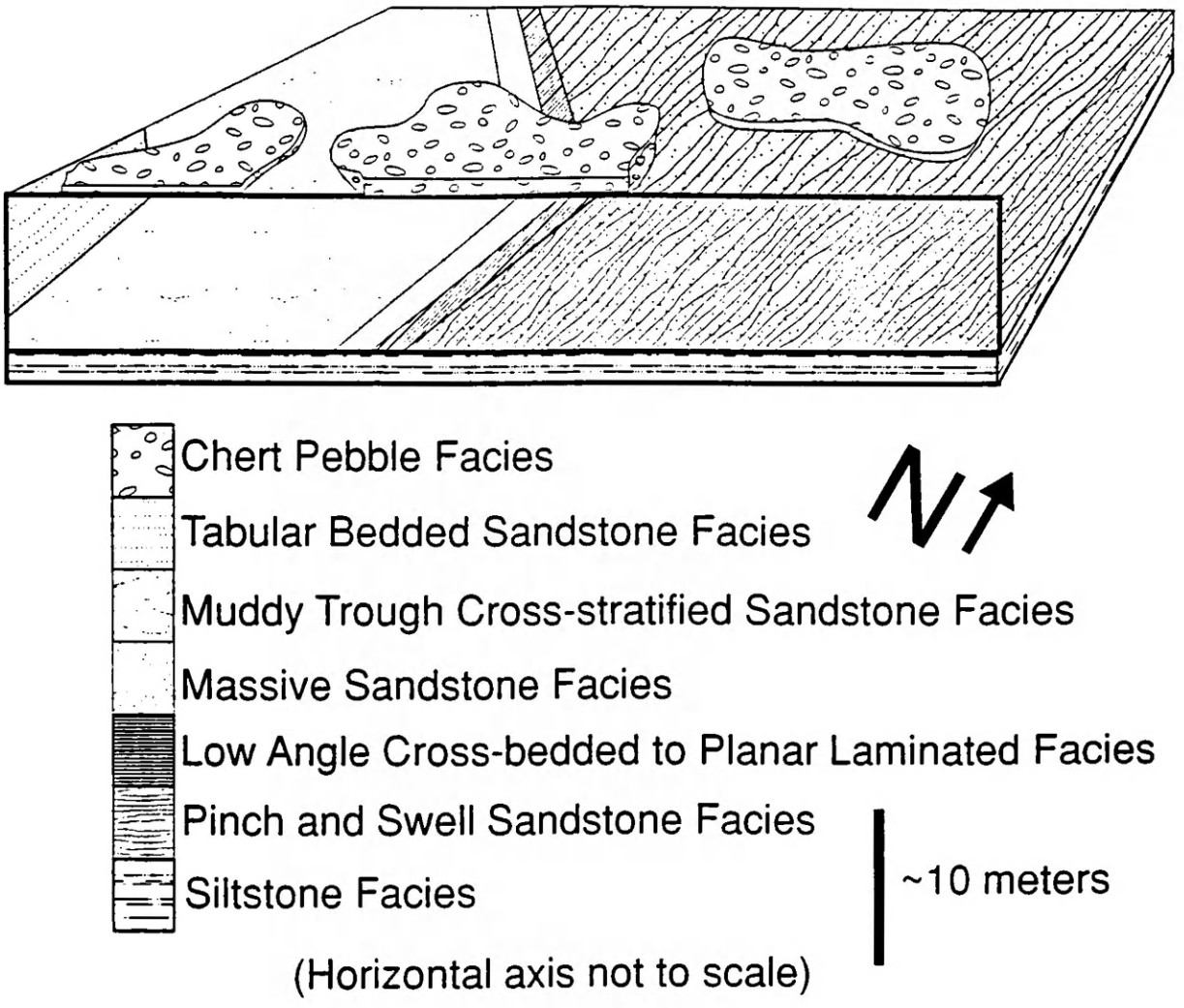

Figure 20: Diagrammatic illustration of the relationship of the facies described in this study. Note the westward dip and westward shingling of the facies between the horizontal Siltstone facies and Chert Pebble facies.

deposited from suspension clouds over a submerged sand bar (Reineck, 1963). This facies corresponds to Lithofacies 5 of Arnott and others (1995).

Chert Pebble facies: This facies is composed of extremely well rounded black chert clasts 0.25-3 cm in diameter set in a coarse sand matrix. It contains shark's teeth up to 1 cm, and bone fragments from 0.1 to 5 cm and exists on the upper surface of the bluff as a discontinuous but persistent layer around 1 centimeter thick. Importantly, it can be found overlying the Low Angle Cross-bedded to Planar Laminated Sandstone, Massive Sandstone, Muddy Trough Cross-stratified Sandstone, and Tabular Bedded Sandstone facies, and is by all appearances horizontal. Thus, it is in angular contact with the underlying facies.

Trace Fossils: None.

Interpretation: This facies is interpreted as a lag that lies in angular unconformity with the underlying facies. It was likely formed during a transgression that eroded an unknown volume of overlying deposits, concentrating the coarse material while removing the finer material. The fact that it has been found on the top of the bluff overlying four different facies and exhibits a concentration of fossils and coarse chert seem to support this interpretation. This facies corresponds with Lithofacies 5 of Arnott and others (1995), which they interpret in a similar fashion.

Figure 21 shows the paleocurrent information gathered in the study area.

2.5 Interpretation of the depositional environment

2.5.1 Possible depositional environments for the uppermost Bootlegger rocks in the study area

The most striking first order observations are that the facies are shingled to the west, and that all sandstone facies are sandwiched between the lower, continuous siltstone facies and the uppermost chert pebble facies. Both the lower and upper contacts of the sandstone appear to be horizontal. The depositional environment of the rocks used for this study has previously been described as shallow marine (Arnott, 1987; Arnott and

Pinch and Swell facies		Transitional Facies		Massive facies		Muddy Trough Cross-Stratified		Tabular	
Unidirectional	Bidirectional	Unidirectional	Bidirectional	Unidirectional	Bidirectional	Unidirectional	Bidirectional	Unidirectional	Bidirectional
108 (A:330)	311/131 (A:100)	192 (F:505)	310/130 (E:540)		296/116 (G:220)	115 (H:295)	0/180 (I:570)	120 (H:390)	295/115 (H:400)
110 (A:490)	302/122 (A:110)	255 (F:520)	315/135 (E:670)		301/121 (E:675)	310 (J:190)	250/70 (I:575)		
105 (A:495)	300/120 (A:480)	305 (F 530)	317/137 (E:665)				318/138 (J:625)		
108 (B:360)	305/125 (B:300)		310/130 (F:540)						
292 (B:685)	299/119 (B:380)		295/115 (F:550)						
286 (C:680)	305/125 (B:685)		306/126 (F:625)						
286 (D:750)	298/118 (B:705)		298/118 (F:630)						
130 (E:280)	300/120 (C:530)		313/133 (F:640)						
92 (E:445)	295/115 (C:605)		305/125 (F:660)						
120 (F:5)	271/91 (C:690-T)		295/115 (F:555)						
306 (F:240)	277/97 (C:690-T)		341/161 (F:670)						
	300/120 (C:685))								
	303/123 (C:670)								
	298/116 (D:180)								
	300/120 (D:575)								
	306/126 (D:745)								
	295/115 (D:160)								
	301/121 (E:250)								
	313/133 (E:295)								
	300/120 (E:335)								
	305/125 (E:460)								

Paleocurrent is an azimuth
Symbols in parenthesis are the letter of the vertical section, followed by the position in cm from the base of the bluff.
T is for trough

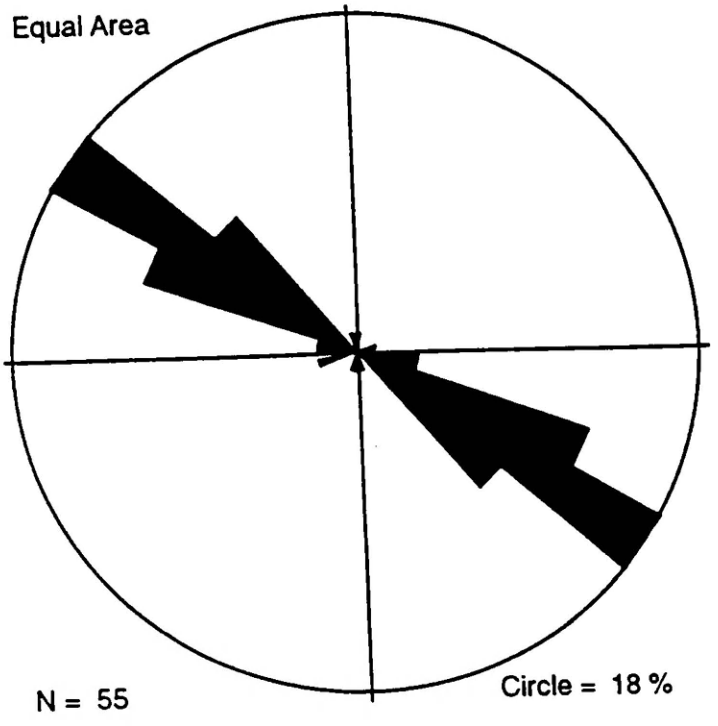

Figure 21: Plot of the 55 paleocurrent measurements made in the study area. Measurements are from all facies, except the Chert Pebble facies. Data from each facies is presented above the plot.

others, 1995). The preserved sedimentary structures in the sandstones, underlying bentonitic siltstones, and abundance of trace fossils support this interpretation. Arnott and others, (1995) suggested that these rocks represent an eastward-prograding nearshore/shoreline sequence. They speculated that the supposed shoreline prograded as a result of decreased accomodation space, possibly caused by vertical uplift of the ancestral Sweetgrass Arch. Internal geometries of facies identified during work with the photo-mosaic (Plate 2) and GPR data (Plate 3) are not consistent with eastward progradation. Rather, these deposits have an internal geometry that is shingled to the west, and record westward migration. This geometry does not seem plausible for an eastward prograding nearshore/shoreline system and suggests that alternate depositional models be considered. The preferred model is a westward-migrating (landward), offshore sand body.

The argument against an eastward prograding nearshore/shoreline deposit is generated from work illustrating the internal geometry of the deposit in the study area. Typical prograding nearshore systems demonstrate a geometry with facies stepping seaward. The surfaces representing the transition between facies are generally seaward dipping, as the deposit progrades offshore (Vail and others, 1977). Although this would not be the case in an upward building progradational event during a transgression (Friedman and others, 1992; Campbell, 1971), seaward dipping surfaces are most common in shoreface settings (Walker, 1984). In addition, the examples illustrated by Friedman and others (1992) and Campbell (1971) occur at large scales that are unreasonable given the 1.6 km length of the exposure in the study area. As seen in Plate 2, internal bounding surfaces in the exposure in the study area are westward dipping, and facies step to the west. This is most clearly demonstrated between Sections F and G, where the Massive Sandstone facies can be seen dropping around 10 meters down and to the west (dipping at around 3 degrees; Plate 2). Westward dip is also seen in two, meter-scale sands (seen between Section C and D; Pinch and Swell Sandstone facies) and the consistently westward dipping reflectors in the radargram (Plate 2). This westward shingling casts doubt on the interpretation of an eastward migrating shoreline.

One might argue that the entire sequence dips gently west due to tectonic tilt, and that the facies were originally deposited vertically on horizontal surfaces. However, the underlying Siltstone facies is in contact with the Pinch and Swell, Transition, Massive, and Muddy Trough facies along the base of the exposure. Tectonic influence would be inferred if the Siltstone facies dipped west as well, but the existence of this facies in contact with other facies in addition to the horizontal attitude of observed Siltstone facies argues strongly against this. Moreover, radar imaging of a flat reflector at the base of the sandstone package (Plate 2) is inferred to be the siltstone/sandstone contact. For clarity, Figure 22 shows two sketches illustrating the internal geometries that one would expect in an eastward prograding nearshore sequence and a westward migrating offshore sand sheet. The eastward prograding model is inconsistent with GPR and stratal architecture data presented herein. Therefore, I propose an alternate interpretation- that of a westward migrating, offshore sand sheet, similar to that of the nearly contemporaneous Shannon Sandstone that outcrops in the Powder River Basin in Wyoming.

2.5.2 Comparison of the deposits in the study area with the Shannon Sandstone

Given the above observations regarding stratal architecture and sedimentology, I propose that the Bootlegger sandstones observed of the study area record deposition in an offshore, westwardly to northwestwardly migrating sand ridge (Nio and Siegenthaler, 1978; Figure 23). This interpretation draws heavily from published descriptions of the Upper Cretaceous Shannon sandstone of Wyoming, also interpreted to be an offshore sand ridge (Spearing, 1976; Tillman and Martinsen, 1984; Gaynor and Swift, 1988). The Shannon has been documented to have been deposited at least 70 miles from shore at middle to inner shelf depths by shore-parallel currents intensified periodically and frequently by storms (Tillman and Martinsen, 1984). The offshore nature of the sand body is illustrated by the fact that it is encased in shelf muds both vertically and laterally. While the Bootlegger succession in the study area can not be similarly demonstrated to be encased in offshore mud by work in this study, the facies described for the Shannon and the internal geometry of the deposit are similar. The Siltstone facies that under- and

Drawing 1: Eastward prograding shoreline

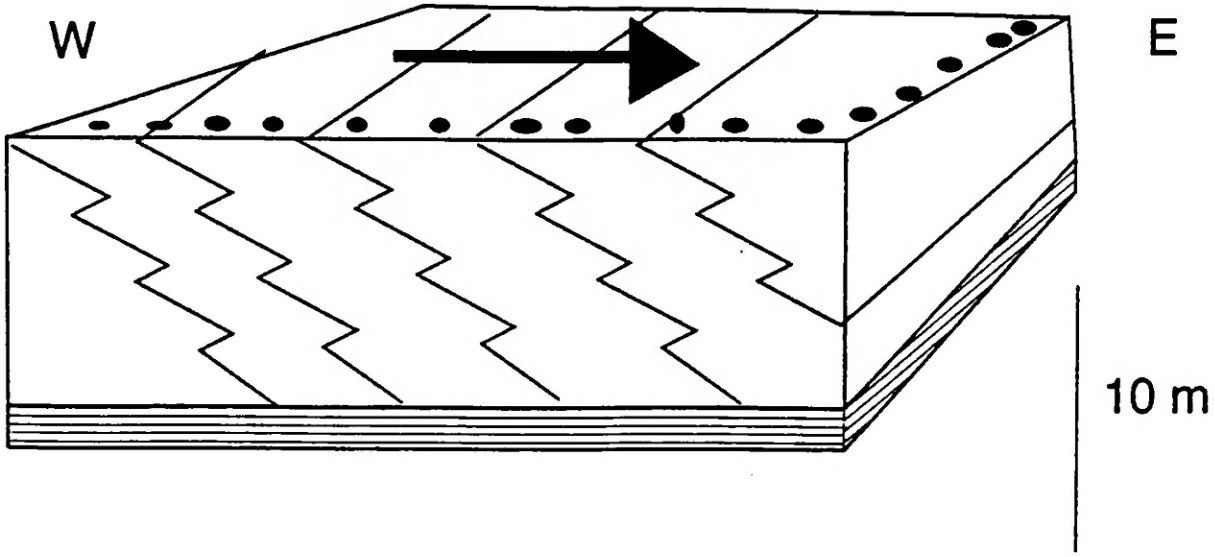

Drawing 2: Westward migrating sand sheet

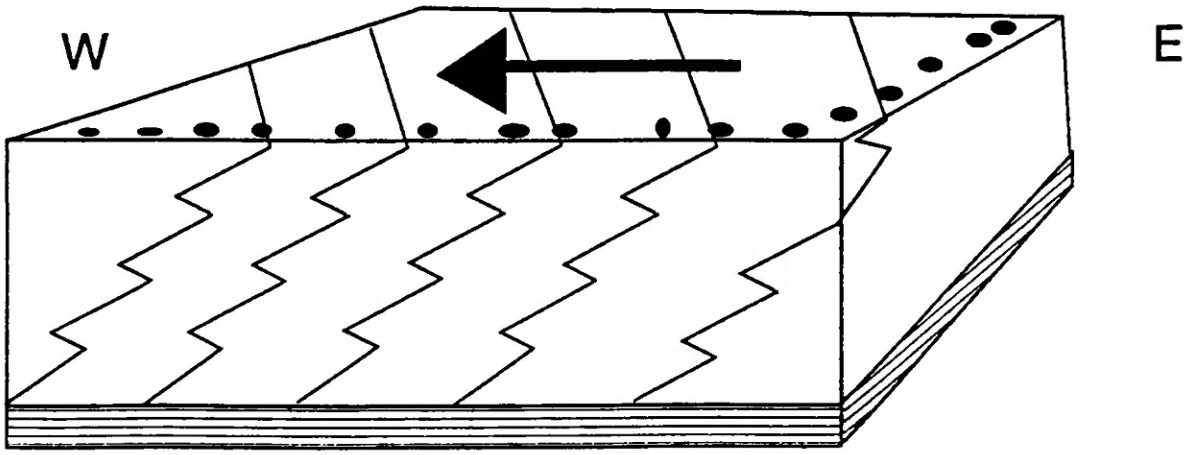

Figure 22: Two contrasting models for the deposition of the rocks in the study area. Drawing 1 is based on Arnott, and others (1995). Drawing 2 is based on information presented in this study.

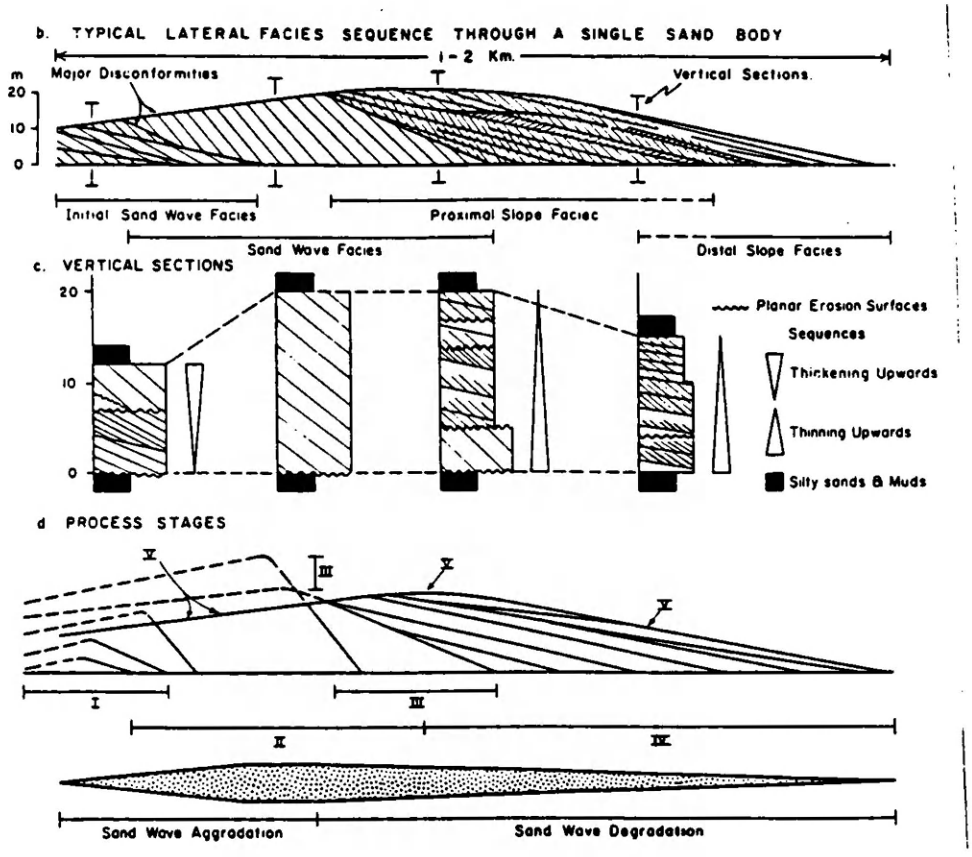

Figure 23: Reproduction of diagram from Nio and Siegenthaler (1978) taken from Walker (1979) illustrating the facies contacts dipping in the direction of migration of a moving offshore sand body.

overlies the sandstones in this study are offshore shelf deposits (Arnott, 1993). The Shannon interval has been shown with isopach maps to range from 20 to 70 feet (6 to 21 meters) in thickness, similar to the average thickness of the sandstone in this study (10 m).

Eleven facies are described (Tillman and Martinsen, 1984) for the Shannon based on physical and biologic sedimentary structures and lithology. The facies are generally stacked in coarsening upward sequences. The most typical vertical sequence encountered was the Bioturbated Shelf Sandstone or Bioturbated Shelf Siltstone facies overlain by the Interbar Sandstone facies, which is commonly overlain by the Central Bar or Bar Margin facies. The Bioturbated Shelf Sandstone and Bioturbated Shelf Siltstone are both dominated by burrowing and occasional ripple stratification and differ only in the average grain size. The Interbar Sandstone facies consists of generally 5-10 cm thick, rippled sandstone beds, with both asymmetrical current ripples and local symmetrical ripples. 5 m wide erosional channels are present as well. The commonly overlying Central Bar facies is composed of high angle cross-beds ranging from planar tabular to planar tangential to trough geometries with increasing energy. This facies is interpreted to be generally of high energy, and the cross-sets commonly exhibit truncated upper surfaces. Burrowing is not abundant, although there are many bedding plane traces. The Bar Margin facies consists of two types (Type 1 and 2), but is composed primarily of high angle cross-bedded sandstones. Type 1 deposits generally differ from Central Bar deposits in that they contain a greater amount of clay clasts and have more burrows. Type 2 deposits are described as transitional between Central Bar and Inter Bar Sandstone deposits. In addition to the high angle cross-beds, type 2 deposits are composed of greater than 25% thin rippled sandstone, with common burrowing.

These deposits are generally quite similar to facies described in this study. Specifically, the similarity of the transition from shelf siltstones into thin, rippled, bioturbated sandstones with small-scale scoured channels, followed by cross-bedded sandstones, some with mud clasts, is compelling. No facies similar to the Tabular Sandstone facies of this study was described for the Shannon, but conditions unique to the Bootlegger environment may be reflected by this discrepancy. Specifically, if the

Massive facies does represent an episodic deposit similar to a washover fan, the event may have locally shallowed the sand body in the study area. Increased current velocity across this shallow zone may have resulted in the deposition of thin bedded, current lineated sands similar to those seen in the Tabular Sandstone facies.

The westward shingling of the Bootlegger facies and the angular relation between Bootlegger sandstones and siltstone facies above and below can also be explained by analogy with the Shannon Sandstone. Spearing (1976) indicated that the Shannon Sandstone grew vertically from a flat surface in a dome shape, with the flanks sloping off from the crest. These slopes would allow vertically stacked facies to lie in angular relationship with the underlying muddy siltstone at the toes of the flanks (Figure 24). By analogy, I interpret the rocks in the study area to represent the western (landward) flank of such a sand body. An eastern flank has not been documented, but should lie to the east of Taft Hill. Arnott (1987) has described Bootlegger deposits east of Great Falls, and has documented a more gradual transition from the underlying siltstone into overlying Bootlegger sands. This more gradational grain size transition may be the result of a more basinward position and associated decrease in grain size.

Finally, the Shannon is interpreted (Tillman and Martinsen, 1984) to have been deposited below daily wave base, but within storm influence, between 60 and 300 feet of water depth. This environment typically preserves fine grained deposits and storm influence (Walker, 1984). Both these are noted in the Bootlegger (silty interbeds and HCS) as well.

In summary, the similarity of the facies descriptions, associations and internal geometries of the Shannon and Bootlegger sandstones suggests that a similar depositional environment is admissible for the rocks in the study area.

Other ancient examples of non-emergent sand complexes on a shallow marine shelf similar to the one described in this study support my interpretations. Studies supporting my facies interpretations and depositional environment include Wright and Walker (1981) and La Fon (1981). Studies that support the internal architecture proposed here include Brenner (1978), Hobday and Reading (1972), Boyles and Scott (1982) and Swift and Rice (1984). Davis and Byers (1989) describe thin (much thinner than the

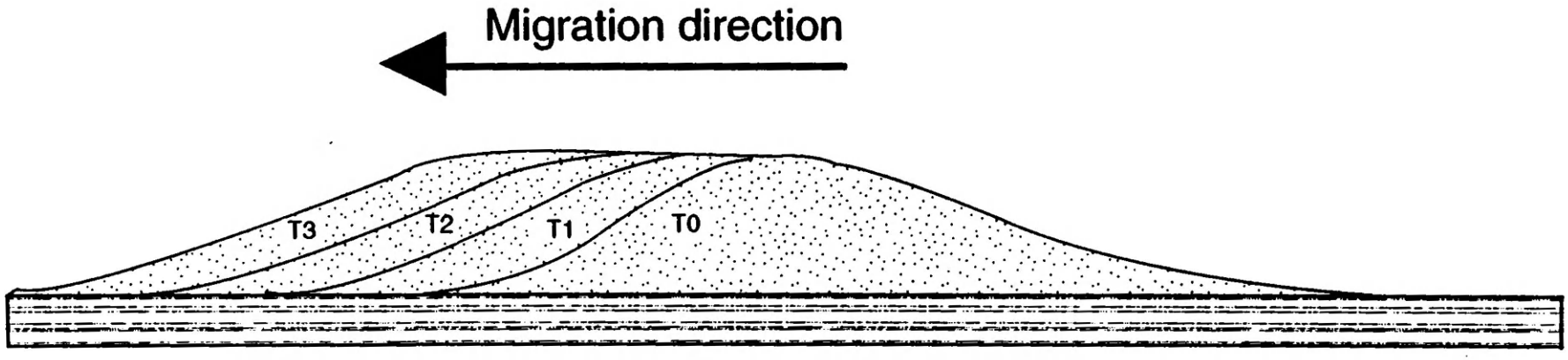

Figure 24: Illustration of Spearing's (1976) concept of the angular relationship produced on the flank of a migrating, offshore sand body. TO is the initial time, and T1, T2, and T3 are progressively later times during migration of the sand body.

Bootlegger), Lower Cretaceous sand bodies in north-central Wyoming and south-central Montana they interpret as offshore sands deposited during sea level falls during the longer term Greenhorn Transgression. Figure 25 highlights two of these examples.

2.5.3 Depositional model for the deposits in the study area

Given the similarity of the deposits in the study area with the deposits described for the Shannon Sandstone and other noted sand bodies, and that the overall geometry of the facies seem to indicate westward progradation, the preferred depositional environment for the rocks in the study area is the shallow offshore. The depth of water that this sand body migrated in must have been within the reach of storm wave base (i.e. 10-15 m; Wright and Walker, 1981). Storm influence of sediments is commonly associated with shallow marine environments (Duke, 1985). Bourgeois (1980) described rippled sands exhibiting HCS that she calculated to have formed in 50 meters of water. The depth of deposition for the Bootlegger at Taft Hill was likely comparable to these estimates based on the similarity of the sedimentary structures. Ancient offshore sand bodies have been documented as occurring from 10 to 100 km from associated shorelines (Brenner, 1978; La Fon, 1981; Boyles and Scott, 1982; Davis and Byers, 1989). Lang and McGugan's (1988) study indicated that during the deposition of the Joli Fou Sandstone (equivalent to the Flood Member of the Blackleaf, Figure 3), the paleoshoreline existed around 111 degrees west longitude at the Montana/Alberta border. The paleocurrent information indicates that dominant currents generally flowed NW/SE. Asymmetric ripples demonstrate that at times currents flowed NW, or generally shoreward. The shingling of the facies suggests the deposit grew with some component westward, but this could record apparent dip. Progradation of the deposit likely paralleled the paleocurrent direction. Storms likely generated combined flow currents with some component directed toward shore (Tillman and Martinsen, 1984). Rossetti (1997) suggested that during storm episodes, sand in an offshore setting can be transported shoreward. In the Bootlegger, such transport could have deposited sand on a shoaling, (north)westward migrating mass, where it was then reworked by the dominant currents.

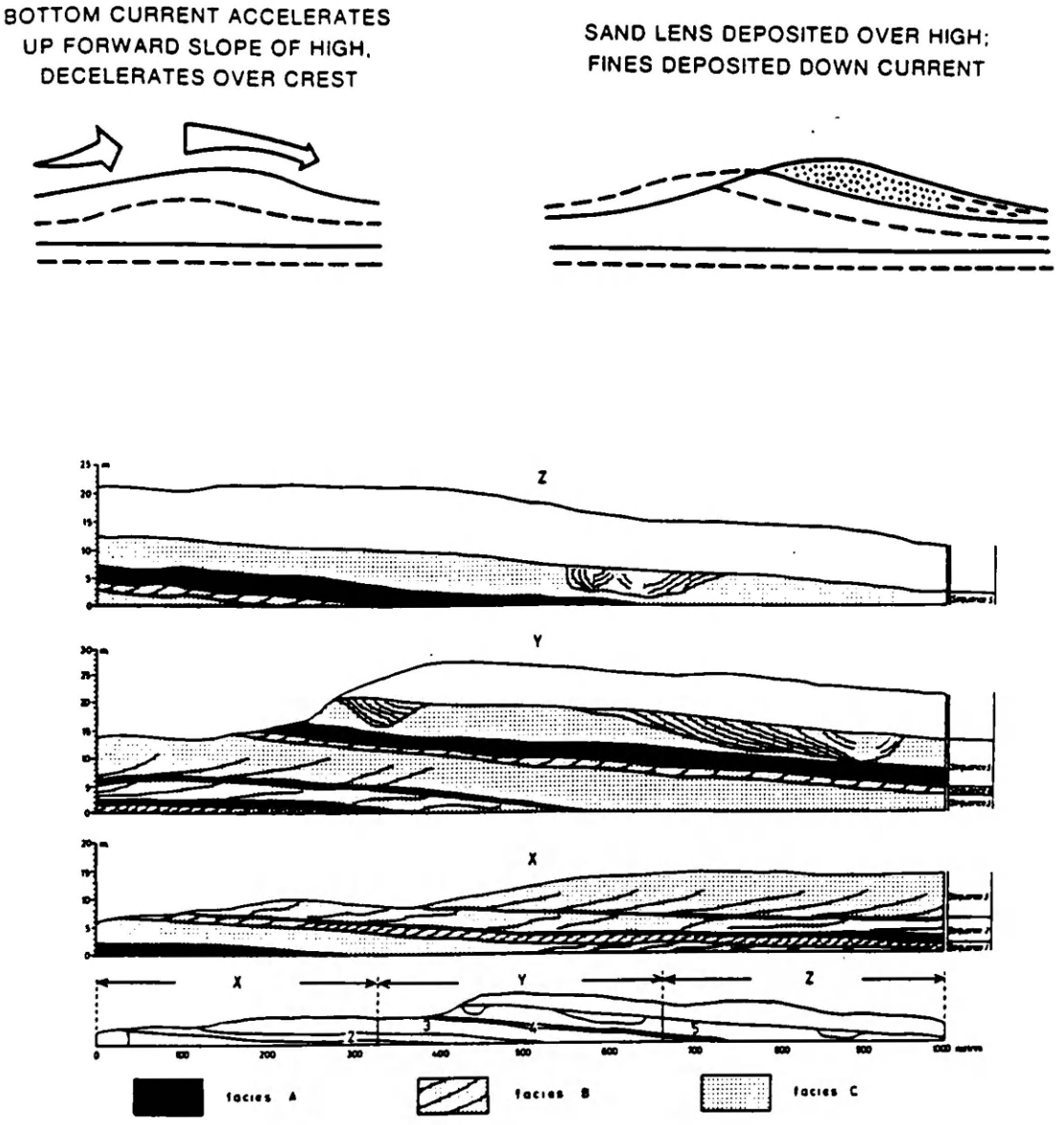

Figure 25: Two examples of the internal architecture of non-emergent sand complexes on a shallow marine shelf. The upper diagram is from Swift and Rice (1984), and the lower diagram is from Hobday and Reading (1972). Note the existence of facies contacts dipping in the direction of migration (to the right).

Different terms have been used to describe sands deposited in the offshore environment (offshore bars, migrating sand sheets, shoreline-attached sheet sandstones, shelf-ridge complexes, shoal retreat massifs, etc.). The different terms are related to inferred genesis and also to the geometry of the sand body. In order to avoid the preconceptions that are attached with these names, the rocks in the study area are described only as a part of an extensive sand body with variable topography up to ten meters that migrated with some component westward (shoreward) in the shallow shelf environment. Arnott (1984) correlated a fish scale horizon in the Great Falls area with a similar horizon in the Sweetgrass Hills of northern Montana, thus implying that the Bootlegger sand body, whatever its genesis, is at least 300 km long. Exposures he described east of Great Falls suggest that the deposit is at least 16 km wide. Such a sand body may have had many smaller regions with local relief (Johnson, 1977). The rocks in the study area may represent one of these smaller regions.

This geometry is comparable to many other Cretaceous offshore sands (Brenner, 1978; Tillman and Martinsen, 1984). Other interpreted offshore sandstones are far less extensive. One reason given by Tillman and Martinsen (1984) for such extensive deposition of the Shannon sandstone was an actively growing paleo-high in the region during deposition. Reynolds (1976) documented similar [to the Shannon] early structural growth and its influence on shelf sedimentation for the Lost Soldier anticline area, Wyoming. Given the proximity and inferred activity of the Sweetgrass Arch (Arnott and others, 1995), similar processes may have been involved in the Bootlegger deposition.

2.6 Possible relation of sea level to the deposits in the study area

Arnott and others (1995) speculated that the progradation of their interpreted shoreline was in response to a decrease in accomodation space caused by vertical uplift of the ancestral Sweetgrass Arch to the east, in a forced regression. The lag at the top of the exposure (Chert Pebble facies) was interpreted by Arnott and others (1995) to be a transgressive lag generated during subsequent sea level rise, with the overlying silty shale deposits record deeper water deposition that followed the transgression. It is assumed

that any subaerial deposits associated with the prograding shoreline were eroded during this transgression, with coarse material being concentrated as the pebble lag. Neither Arnott (1987) nor I argue that any of the deposits in the study area are subaerial. If any were deposited at all, they have since been eroded by a transgression.

If one accepts the model of an offshore, westerly migrating sand complex to be accurate, then this upper surface should represent both a regressive and transgressive surface. It is the argument of this author that the rocks in the study area were deposited 10 to 100 km offshore, and were completely subaqueous. If this is true, than in order to deposit a transgressive lag composed of coarse material likely derived from the coast, relative sea level may first have fallen to expose the deposits in the study area before a transgression could have taken place. During a regression, an unknown thickness of shoreline, terrestrial, and perhaps fluvial deposits would have overlain the Bootlegger deposits. The subsequent transgression eroded these deposits and concentrated the chert pebbles, sharks teeth, and fish bones. This type of event, known as an erosion/transgression (E/T) (Plint and others, 1986) was recognized by Arnott and others (1995), but discounted based on a lack of stratigraphic data basinward.

An interesting aspect of the rocks in the study area is that the contact between the Siltstone facies and the overlying Pinch and Swell Sandstone facies (at the base of section A, and noted westward) is abrupt (erosive) and indicates a rapid shift in depositional environment. The Siltstone facies described in this study was interpreted as a shallow shelf deposit by Arnott (1984), and its bentonitic nature and trace fossils seem to suggest this. Why would sand be rapidly introduced (as the trough cross-beds and mud intraclasts suggest) to this environment? Likely, the sands in this study were introduced into a shelf environment due to initial regression. During a highstand, which is presumably recorded by the bentonitic Siltstone facies underlying the sands in this study, clastic sediment would be retained in the nearshore environment (Ryer, 1977). A regressive (progradational) episode would cause clastic sediment to be brought offshore (Walker and James, 1992), where it could be distributed by longshore drift and influenced by storm events, perhaps forming the offshore deposits recognized in this work. In this way, the sediments in the study area may be related to a progradational shoreline that existed to the

west, but do not themselves record the shoreface. Hence, the only difference between this interpretation and the one proposed by Arnott and others (1995) is that the rocks are not considered shoreface deposits. The rocks still may record an overall regressive period. Arnott and others (1995) account for the sharp based succession in the study area in this way. Others (Walker, 1984) have interpreted sharp based offshore sand bodies as regressional deposits as well.

In support of such an interpretation, Arnott (1984) described related rocks to the east of Great Falls with a more complete record of the transition from the offshore siltstone to the sand interval. Specifically, he reported the gradual introduction of small sandstone beds into the muddy siltstone east of Great Falls, or a gradual increase in the sandstone to mudstone ratio. This gradual transition could be interpreted as reflective of a more basinward response to the progradational event taking place at the time. The Taft Hill site may not have as gradual a transition because it would have been closer to the paleoshoreline, where more erosion of the shelf occurred due to shallower depths. This concept is supported by work described by Walker and Plint (1992) with reference to the sharp-based sandstone packages of the Viking sandstone in Alberta. The thicker and more complete record of Bootlegger deposition to the east may also be attributed to a more offshore depositional environment.

CHAPTER 3

Ground-Penetrating Radar Imaging of the Taft Hill Exposure

3.1 Introduction to GPR

Ground-Penetrating Radar (GPR) has been shown to be of great utility for investigating various problems related to the shallow subsurface. Studies to date have focused on the architecture of unconsolidated and some consolidated deposits (Beres and others, 1995; Smith and Jol, 1992a, 1997; Bridge and others, 1995; Gawthorpe and others, 1993; Stephens, 1991). Some studies focused on the internal structure of various deposits such as lacustrine deltas (Jol and Smith, 1991), peat deposits (Jol and Smith, 1995), and gravel deposits (Huggenberger and others, 1994; Gawthorpe and others, 1993; Huffman, 1992). Still others have successfully interpreted the depositional setting of Quaternary deposits (Bridge and others, 1995), including coastal spits (Smith and Jol, 1992b). More recently, some researchers have become interested in the use of GPR for sedimentological characterization of clastic reservoir analogs (McMechan and others, 1997, Knight and others, 1997). The number of publications concerning GPR in the last decade is evidence of growing interest in the applications of the technique. Articles of particular interest to those unfamiliar with the radar process include Annan and Davis, (1977), Davis and Annan, (1989), and Jol, (1995).

GPR has been compared to shallow seismic methods based on similar fundamental principles and the style of data generated. That is, both methods rely on subsurface heterogeneity to reflect energy that can then be displayed in the wiggle trace format. The fundamental difference is that while seismic processes use acoustic waves and the interaction of these waves with the different acoustic properties of the underlying deposits, GPR uses electromagnetic energy and the interaction of these waves with the different electrical properties of the underlying deposits. GPR generally provides greater resolution than shallow seismic methods, and is preferable in some environments where this is desirable. Both processes record reflected impulses during a specified time interval. These impulses are then plotted as position versus two-way travel time. In place of an acoustic source and numerous, regularly spaced geophones, GPR uses an antenna to

generate electrical energy of a specific frequency which is then received by a singular, similar antenna.

The PulseEKKO IV unit used in this study is manufactured by Sensors and Software© in Mississauga, Ontario. It is composed of a console, powered by a car or wheel chair battery, that is connected to two antennae (of the desired frequency) by fiber optic cables and to a portable computer through the serial port. The antennae are each powered by two 6 V batteries in series. The transmitting antenna generates a short electromagnetic pulse in the FM radio frequency (10 to 1000 MHz) characteristic of the antennae being used. That pulse propagates into the ground and is eventually received by the other antenna. As the pulse propagates it interacts with the electrical properties of the subsurface material. Some of the energy is reflected at interfaces where the local differences in the electrical properties are significant, the rest continues downward. The pulse propagates according to Snell's law (McMechan and others, 1997) and is eventually received at the surface by the second antenna where it is amplified, digitized, and stored as amplitude versus two-way travel time. By moving the antennae in discrete intervals and repeating the process, the single traces of reflected energy versus time for each position can be plotted next to each other according to their position. These traces constitute a profile of the underlying electrical properties of the medium. "Reflectors" on the GPR profile can then be interpreted in terms of their continuity, amplitude, and shape to infer the structure in the underlying material. Note that the resulting profile is only a representation of the variability of the electrical properties of the underlying material. Relating the profile to geology requires control points where subsurface geologic characteristics are known.

3.2 Theory of electromagnetic propagation

The propagation of radar energy is controlled by the high frequency electrical properties of the ground, which affect velocity, attenuation, and the power reflected at boundaries (Davis and Annan, 1989). The electrical properties of most significance are

the magnetic susceptibility, electrical conductivity, and electric permitivity. These are discussed below in more detail.

Olhoeft (1990) and Hoffman (1992) state that above a few megahertz (most radar surveys), magnetic susceptibility of most geologic is quite low. Arnott (1987) performed electrical measurements on some of the rocks in the study area and indeed concluded that the magnetic susceptibility of the deposit is generally quite low. Thus, the electrical conductivity and electric permitivity most affect propagation and attenuation of radar energy (Gawthorpe, and others, 1993 and Meyers, 1994).

Electrical conductivity is the ability of a material to conduct an electric current. Generally materials with low conductivity (less than 10 microseimens per meter) are more suited to GPR methods than those with greater conductivity (Meyers, 1994). Greater conductivity causes the radar energy to dissipate more efficiently, reducing penetration depth and resolution. Jol (1993) states that the most important factors affecting the conductivity of geologic materials are texture, particle shape, moisture content, structure, temperature, porosity, the presence of electrolytes, and the measurement frequency. Moisture content and the total dissolved solids within the moisture are considered the most influential. Sen (1980) reported on the dependence of dielectric constant and conductivity of sedimentary rocks on clay content, salinity, frequency, and grain-texture variables, and investigated further (Sen, 1984) the grain shape effects on dielectric and electric properties of rocks. Knight and Nur (1987) made measurements of the dielectric constant of sandstones from 60 kHz to 4 MHz and concluded that for these frequencies the surface area-to-volume ratio of the pore space determines the amount of surface water in the pore space, which controls the frequency response of the rock, making this ratio the essential material property governing the dielectric response of a sandstone.

Technically, the electrical permitivity is the ratio of the capacitance of an electrical condenser filled with a dielectric (a nonconductor of electricity, a material for which charges of opposite polarity separate in an applied electric field; Huffman, 1992) to the capacitance of the same condenser when evacuated (Moorman, 1990). As stated by Jol (1993), it is a measure of a material's ability to store electrical charge when an electric

field is applied. Materials with high permitivity decrease the strength of the radar pulse as it propagates in a medium because the radar energy is effectively dissipated. The permitivity is generally expressed as a dielectric constant (K), which is composed of both real (K`) and imaginary (K``) components. Davis and Annan (1989) illustrate the mathematics involved in the relationship of these two components to the constant. The dielectric constant is a measure of the degree to which a material can be polarized relative to permitivity of free space ($8.854 * 10^{-12}$ $C^2/(N*m^2)$), and is thus always greater than 1. The permitivity value for water, generally an order of magnitude greater than that for common rock types, illustrates the strong influence water saturation has on the dielectric constant. Figure 26 presents the electrical properties of common geologic materials.

3.3 Velocity considerations

Radar wave velocity is a function of the frequency, dielectric constant, and conductivity. Velocity is related to frequency by the relationship $V = f\lambda$, where f is the frequency and λ is the wavelength. In a vacuum, the velocity is $3*10^8$ m/s, the propagation velocity of electromagnetic waves in free space. For a given λ, an increase in frequency increases velocity. Velocity is inversely proportional to the square root of the dielectric constant given by: $V = c/\sqrt{K'}$, where c is the propagation velocity of electromagnetic waves in free space and K` is the real part of the dielectric constant. Thus the velocity is inversely related to the permitivity. In addition, for a given frequency, an increase in conductivity decreases the velocity. Figure 27 illustrates the relationship between frequency, conductivity, and velocity.

Velocity can be estimated using two different techniques: deduction from field data and calculation using the dielectric constant. If a discrete reflector is known to exist at some depth, the field estimate uses the two way travel time to that reflector to calculate the velocity, a method called the common midpoint technique (CMP). In this technique, antenna separation is gradually increased by a given distance over a fixed location. By increasing the antennae separation, the ray path to a given point on a subsurface horizon is increased, delaying the arrival time of the reflection. A plot of the two-way travel time

Material	K	σ (mS/m)	V (m/ns)	α (dB/m)
Air	1	0	0.30	0
Distilled water	80	0.01	0.033	0.002
Fresh water	80	0.5	0.033	0.1
Sea water	80	30,000	0.01	1000
Dry sand	3 - 5	0.01	0.15	0.01
Saturated sand	20 - 30	0.1 - 1.0	0.06	0.03 - 0.3
Limestone	4 - 8	0.5 - 2	0.12	0.4 - 1
Shales	5 - 15	1 - 100	0.09	1 - 100
Silts	5 - 30	1 - 100	0.07	1 - 100
Clays	5 - 40	2 - 1000	0.06	1 - 3000
Granite	4 - 6	0.01 - 1	0.13	0.01 - 1
Dry salt	5 - 6	0.01 - 1	0.13	0.01 - 1
Ice	3 - 4	0.01	0.16	0.01

K - Dielectric Constant
σ - Electrical Conductivity
V - Velocity
α - Attenuation

Figure 26: The dielectric constant, electrical conductivity, velocity, and attenuation for various geologic materials. The velocity used in this study (0.08 m/ns) is reasonable given these values, as it is in the reported range for many rock types. From Davis and Annan (1989).

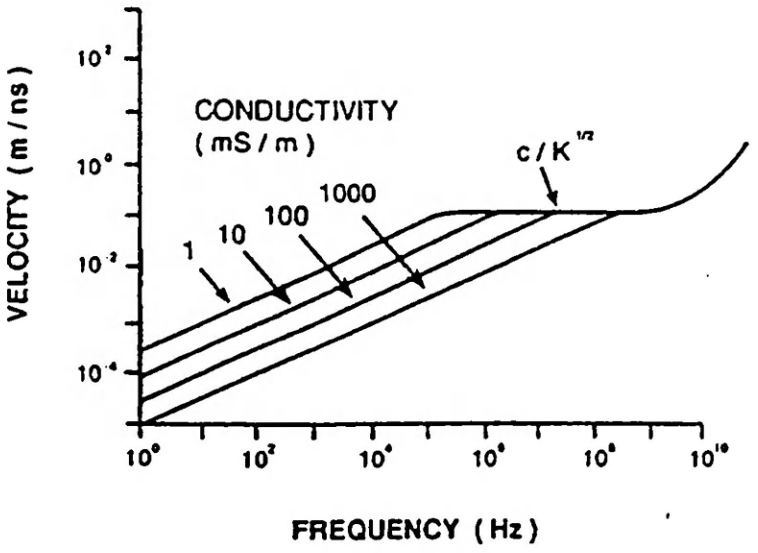

Figure 27: This figure illustrates the relationship between frequency, conductivity, and velocity. Taken from Davis and Annan (1989).

versus the separation distance is then used to estimate velocity (Figure 28). This method is similar to the normal move out analyses done in seismic work. It is important to note that this technique assumes a flat horizon that extends the length of the profile, and that the pulse travels linearly and consistently reflects off the same point on that horizon, a case that is hard to verify but is generally assumed to be true. Often it may be difficult to identify such a reflector, and the second method is used. Estimates of the velocity may be calculated from measurements of the dielectric constant in field samples using the equation above.

3.4 Other considerations

Reflections of the EM wave are the result of a contrast in the dielectric constant across a subsurface boundary. The reflection coefficient, R, for normal incidence is

$$R = \frac{\sqrt{K_1} - \sqrt{K_2}}{\sqrt{K_1} + \sqrt{K_2}}$$

where K_1 is the dielectric constant of the upper medium (1) and K_2 is the dielectric constant of the lower medium (2). Stephens (1991) states that GPR reflections are not always the direct result of any visually derived bounding surfaces. They may be attributed most effectively to changes in the bulk electric properties within or between elements in the stratigraphy. While the exact cause of a reflector can be attributed to many different variables, work to date has not sufficiently isolated any single variable as the cause for a given reflection. Little work by those who have previously correlated GPR data to stratigraphy has addressed this concern adequately. Information presented later in this thesis attempts to initiate an understanding of the importance of this aspect of radar work when data is correlated to stratigraphy.

The amplitude of a reflection is affected by numerous variables, and Baker (1991a, 1991b) states that the relative reflection amplitude is generally insufficient to uniquely determine a specific type of bounding surface. Thus the radar trace does not necessarily reveal distinct lithologic contrasts with a distinct amplitude. As seen above, it is the ratio of the dielectric constants that is significant, not their magnitude. Many

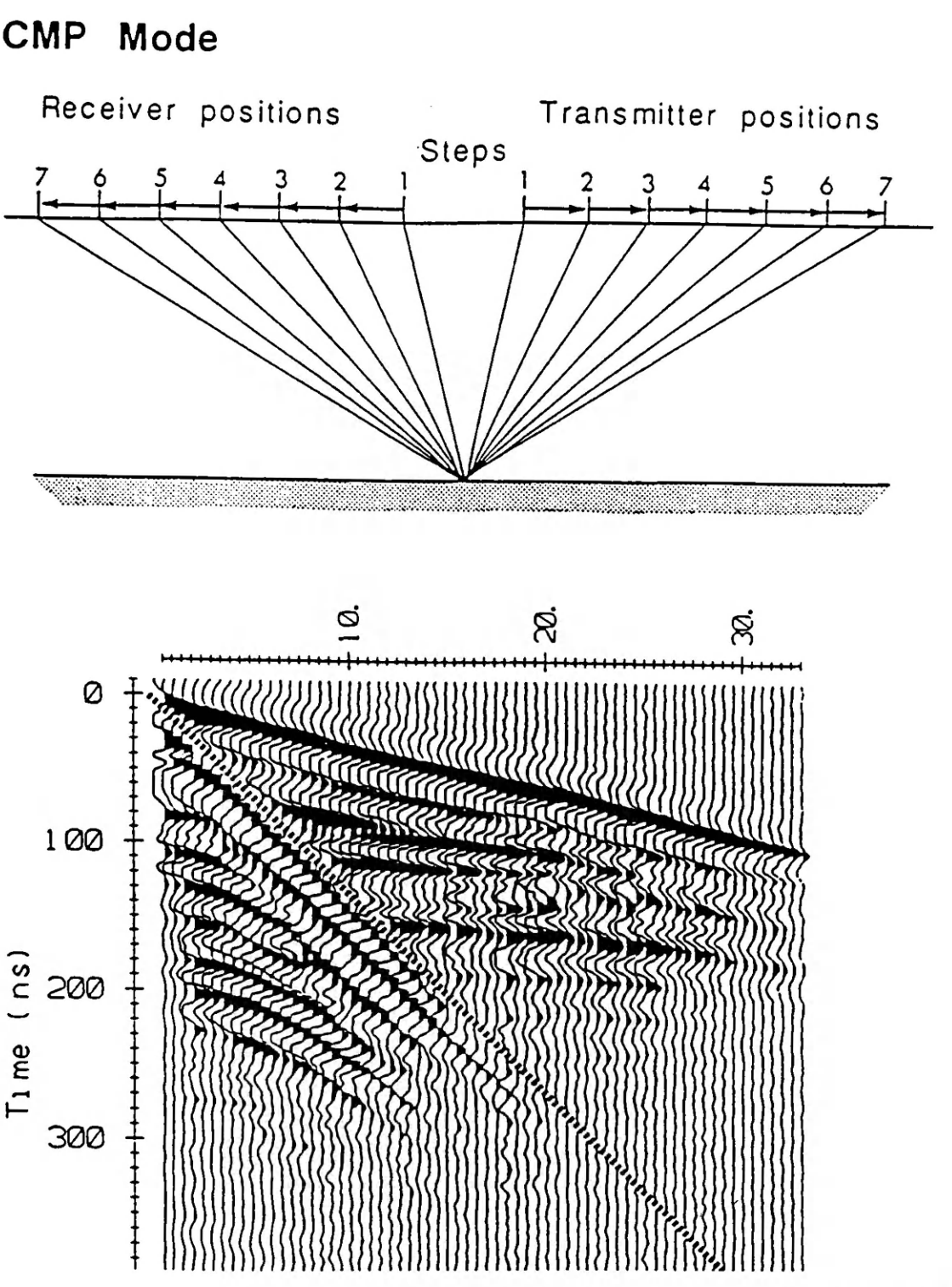

Figure 28: An illustration of the CMP technique and the ideal record. The antennae position is increased from position one to two, etc. for each subsequent trace. In the lower diagram, the horizontal axis is the antennae separation in meters, and the vertical axis is the two way travel time of the radar wave in nanoseconds. The velocity is 1/slope of the ground wave (indicated by the dashed line), and was found to be 0.07 m/ns. Taken from Meyers (1994), p. 23.

different combinations of the characteristics influencing the dielectric constant can yield similar amplitude reflections. For example, a contact between saturated sand and dry gravel may produce a reflection equivalent to a contact between granite and limestone. Finally, reflected energy behaves in an analogous manner to seismic reflections. Similar problems such as secondary reflections, ringing, and long path multiples can be encountered using GPR (Meyers, 1994; Moorman, 1990). Telford and others (1990) present a discussion of these complications.

3.5 The effect of water on GPR

The effect of water on the GPR method is complex, can be quite significant, and is the subject of much current research (Beres and Haeni, 1991; Greaves and others, 1996; Baker, 1991). The influence of water revolves around its high relative permitivity and large effect on attenuation. As noted previously, the dielectric constant of water is generally an order of magnitude higher than dry geologic materials, and thus the varying degree of water saturation within a deposit significantly affects the distribution of dielectric constants and therefore the reflection coefficients. Theoretically, water results in a decrease in the velocity by increasing the dielectric constant. The specific effect of water on electrical properties is related to the dielectric relaxation of the water molecule. As the radar waves passes through a material, it polarizes (rotates) the water molecules, resulting in attenuation of the energy.

3.6 Resolution

The expected resolution for a given frequency is similar to seismic expectations and, at best, is approximately ¼ of dominant wavelength (Sheriff and Geldhart, 1982). Given all the variables associated with the GPR method, a more conservative estimate is ½ of the dominant wavelength (Meyers, 1994). Jol (1995) suggested that the wavelength of the propagating pulse be long compared with the gradation of the boundary of interest in order to resolve that boundary. Resolution may also be controlled by pulse width and

frequency (Gawthorpe and others, 1993). The wavelength is related to the velocity and frequency by the equation $\lambda = V/f$, where λ is the wavelength in meters, V is the velocity in meters/nanosecond and f is the frequency in cycles/nanosecond. The frequency in this study is constrained to 50 MHz. Because velocity is such a critical factor in the resolution, an attempt was made to determine how sensitive resolution would be to different velocities using 50 MHz. Figure 29 is a plot of different velocities versus expected resolution for 50 MHz. From this plot it is clear that for each 0.01 m/ns that the velocity estimate is in error, the resolution changes from 5 to 10 cm depending on whether ¼ or ½ of the wavelength is resolved respectively. For a velocity of 0.05 m/ns, the best resolution that can be expected is 25 cm and the worst is 50 cm. If the velocity was in fact 0.08 m/ns, the resolution best resolution would be 40 and the worst 80 cm. Therefore, the velocity determination is not only important in converting time sections to depth sections, but also important with regard to the resolution expected.

3.7 Processing of GPR data

Similarities between the data sets of GPR and seismic surveys allow processing techniques developed for seismic data to be modified for use on GPR data. Both data sets are commonly displayed in a wiggle trace format. Each trace contains amplitude versus time information, which, when combined with the position information, results in a three variable data set: position, amplitude, and time. Because GPR data are stored digitally, they can be processed by different methods repeatedly without affecting the original data. This allows the effects of different processing techniques to be directly compared.

In this study, processing was performed with software provided with the GPR unit, and generally time and spatial gains, filters, as well as vertical and horizontal trace averaging were applied. Gains are applied to compensate for the various aspects of attenuation that occur during radar surveys. Radar reflection amplitude decreases dramatically with time, so that deeper reflection amplitudes can be orders of magnitude smaller than shallow reflection amplitudes. Gain procedures evaluate the amplitude versus time data for each trace and scale the amplitudes according to a defined time

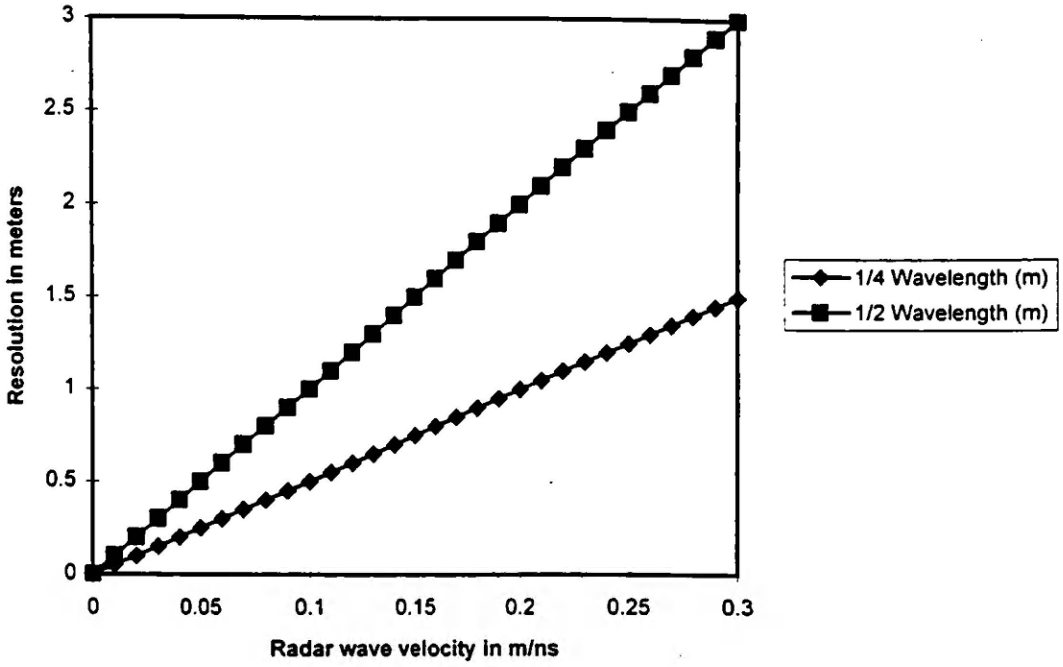

Figure 29: This is a plot constructed to illustrate the variability of resolution with different velocities at 50 MHz. The horizontal axis is the radar wave velocity and the vertical axis is the expected resolution. The two lines represent resolution of ¼ and ½ the wavelength. The wavelength was calculated using $\lambda=V/f$, and then fractions of this value were taken as the expected resolution. For every 0.01 m/ns the velocity determination is in error, the resolution increases from 5 to 10 cm, depending on whether ¼ or ½ of the wavelength is thought to be resolved. For a velocity of 0.08 m/ns, ¼ of the wavelength is 40 cm and ½ of the wavelength is 80 cm. Resolution in this study is thought to be in this range.

function. PulseEKKO IV software allows four different gaining procedures to be used: automatic gain control (AGC), spreading and exponential compensation (SEC), constant gain, and user defined gain.

AGC attempts to equalize all reflections to a given amplitude. The gain applied is essentially inversely related to the signal strength. Large amplitude reflections receive low gain, while small amplitude reflections receive a large gain. This usually improves the continuity of reflectors across a profile. No comparisons of signal amplitude may be made after this gain has been applied. SEC applies a gain that increases exponentially with time. Later signals receive the most gain, regardless of their original amplitude. Some comparison of reflector strength may be possible when this gain is used, as the same gain is applied over the same time interval for adjacent traces. Constant gain simply multiplies each amplitude by a constant number. Amplitudes throughout a profile all receive the same gain. User defined gains allow the user to describe a function that will be used to gain the data. The advantage of this gain is the ability to construct more sophisticated gain functions that may improve specific data sets more than the standard gains.

Filters are used to isolate specific frequencies of the data. A recorded reflection amplitude may be a result of the superposition of different frequencies with different amplitudes. For example, each recorded amplitude may contain some high frequency noise from various sources. In this instance, filters can eliminate the effect of the high frequency component on the reflection amplitude. This would be a low pass (or high cut) filter. Other filters include high pass (low cut), bandpass, and DC Shift. Filters may be applied in both the spatial and time domains (between and within individual traces respectively).

Other processing techniques include averaging traces vertically and horizontally. This serves to "smooth" data and to present a more coherent image of the subsurface. Traces may be added together or subtracted, cropped, merged, inserted or deleted, as described in the PulseEKKOIV RUN User's Guide. The specific processing techniques used in this study are presented in section 3.8.3.

3.8 GPR Methodology

3.8.1 Field Methods

GPR profiles were recorded within 10 meters of the cliff face directly on the upper surface of the exposure. This area close to the cliff generally had little to no ground cover and thus aided the coupling of the radar wave with the deposit. A chord with markings every 0.5 meter was used to position the antennae across the profile. This spacing was used in order to resolve lateral variability in the exposure at this scale. Flags labeled with position information were placed regularly along the profiles, allowing the location of measured stratigraphic sections to be directly located on the radar image. Individual files collected averaged 100 meters in length. The position of the antennae was input at the beginning of each file, and separate profiles were joined according to these positions. Antennae separation was 2 meters and each antenna was moved 0.5 meters before collecting the next trace. In this way a continuous profile was constructed over the 1.6 km of outcrop used in this study. The 1.6 km length of the line is similar to the distance between two production wells at a reservoir scale.

50 MHz antennae were used for the duration of the study after various frequencies (50, 100, and 200 MHz) had been tried and the determination made that the best depth to resolution trade off was achieved using 50 MHz. The impulse voltage used was 1000 V as this increased the depth of penetration. 128 stacks were recorded at each position along the profile, which represented the best compromise between survey time and signal to noise ratio. The time window for recording was 600 ns, which was far greater than necessary for the thickness of the outcrop. The velocity used in this study was 0.08 m/ns (see below), possibly allowing information from depths of 24 meters to be recorded within a 600 ns time window.

3.8.2 Velocity Determination

The velocity determination is a critical aspect of interpreting the radar profiles. Three independent assessments of velocity were made. Initially, many Common

Midpoint Soundings (CMP) were made at different locations along the profile. Figure 30 presents the results of one CMP survey in the study area. From this plot, the velocity is determined by using the inverse of the slope of the ground wave. The plot presented represents the best CMP survey in the study area, and the velocity was determined to be 0.08 m/ns. These data are not ideal, and the lack of a single continuous horizon at a shallow depth was likely the cause for unsatisfactory CMP results. The discontinuous, thin bedding characteristics of the outcrop also likely negatively influenced the CMP. Due to the poor quality of the CMP method, other methods to constrain the velocity were pursued.

Velocity estimates can be constrained by simple geometric considerations. Using a standard spreadsheet, different velocities were multiplied by a 250 ns time window used in order to determine the velocity that seemed to make sense given the thickness of the exposure. No significant reflections were observed after 250 ns (Figure 31), and were not expected to come from deeper than around 10 meters, as it is unlikely that the radar wave penetrated effectively into the underlying muddy siltstone (Meyers, 1994). By determining the time over which strong reflections were received (0-250 ns), the velocity for which its product with this time corresponded to a total distance traveled of around 20 meters (two way travel) is a good first approximation for the velocity. The assumption is made that responses received during the 250 ns window represent the entire thickness of the 10 m outcrop. This seems reasonable, as the time window was left open long enough during acquisition to allow for this. It is assumed that the latest responses are those from the bottom of the exposure (Figure 31). Figure 32 shows calculations of the distance that waves of various velocities will travel in 250 ns. Using this reasoning, velocity can be constrained to be between 0.07 and 0.09 m/ns, which correspond well with the CMP determination.

Finally, velocity estimates can be made using the measurement of the real part of the dielectric constant. Velocity is related to this value by the relationship

$$V = \frac{c}{\sqrt{K'}}$$

where c is the propagation velocity of electromagnetic waves in free space ($3*10^8$ m/s) and K` is the real part of the dielectric constant. Measurements of the real part of the

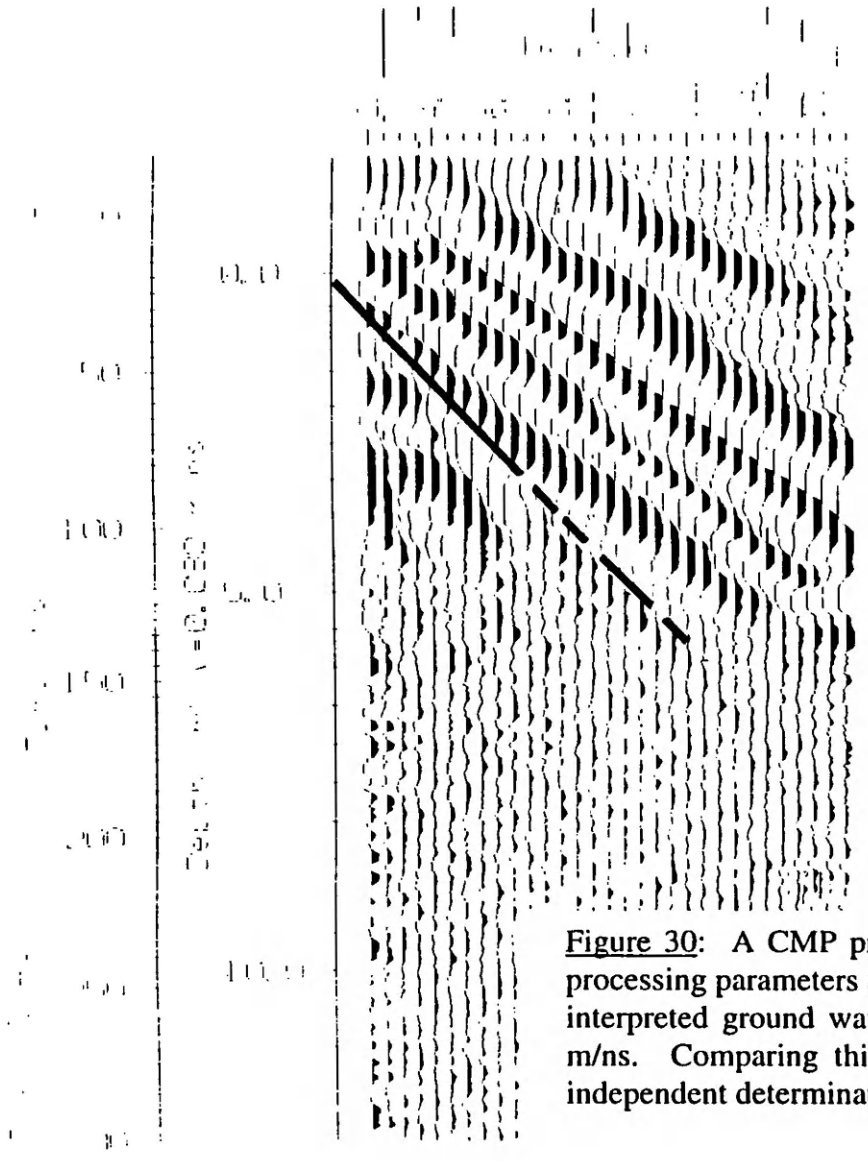

```
PROCESSING SELECTED:
   Trace Stacking     : 8
   Points Stacking    : 4
   Trace Differencing: N
   Correction         : DEWOW
   Gain Type   : AGC
     Window    : 1.000  pulse widths
     Amount    : 1000 Maximum
   Selection   : Time = all
                 Position = all
   Picture Id  : 06/25/98-15:42:30
```

Figure 30: A CMP profile recorded in the eastern part of the study area. The processing parameters are found in the data sheet included. The dashed line is the interpreted ground wave. For this plot, the velocity was determined to be 0.8 m/ns. Comparing this figure to Figure 28, the data are not ideal, and other independent determinations of velocity were made.

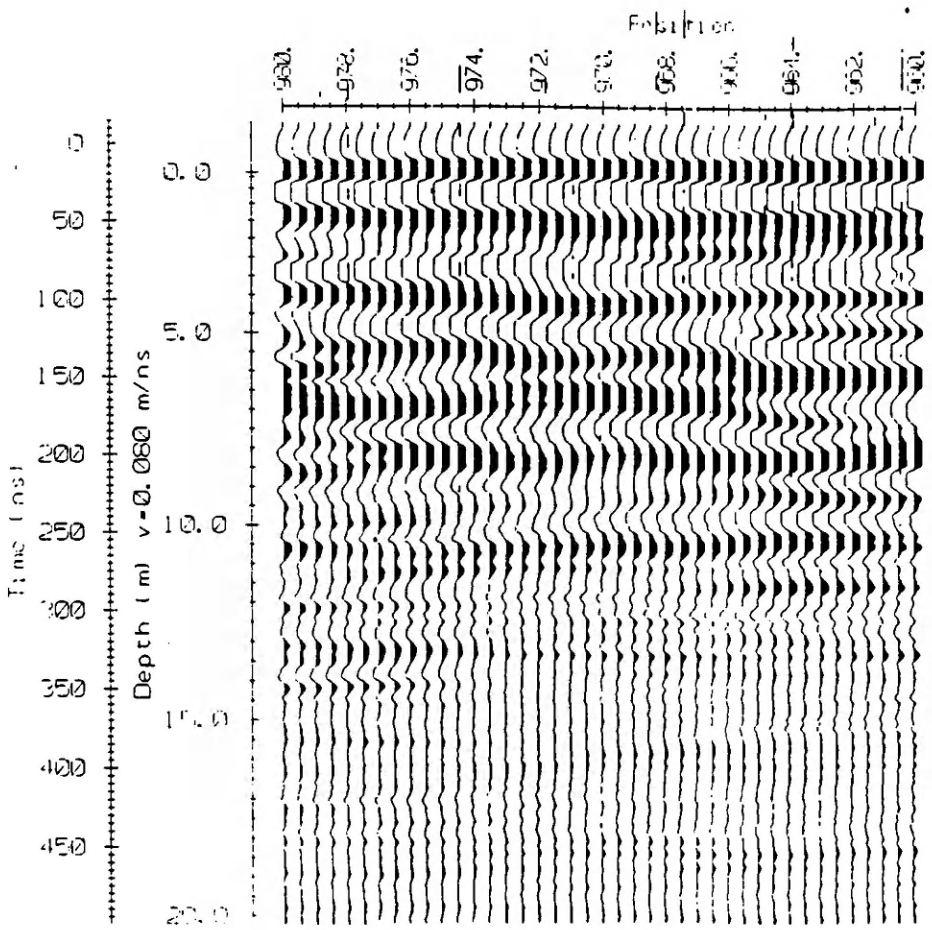

Figure 31: A portion of the radar data illustrating the lack of strong reflectors below around 250 nanoseconds.

Velocity (m/ns)	Time 1 (ns)	Distance Traveled
0.03	250	7.5
0.04	250	10
0.05	250	12.5
0.06	250	15
0.07	250	17.5
0.08	**250**	**20**
0.09	250	22.5
0.1	250	25
0.11	250	27.5
0.12	250	30
0.13	250	32.5
0.14	250	35
0.15	250	37.5
0.16	250	40
0.17	250	42.5
0.18	250	45
0.19	250	47.5
0.2	250	50
0.21	250	52.5
0.22	250	55
0.23	250	57.5
0.24	250	60

Figure 32: This table shows the estimates of the velocity considering geometrical field constraints. The bold data are of most significance. No radar reflections were recorded after 250 ns in the field (see Figure 31). A velocity of 0.08 m/ns allows the signal to travel 10 meters down and return in the 250 ns window.

dielectric constant were made on 15 samples from Section G (Appendix II). Velocity calculations using these values are presented in Table 33. Note that the measurements were made on samples with 0% and 100% saturation, providing bounds for the possible velocity values in the outcrop. The actual saturation of the layers in the outcrop was not determined due to the difficult nature of this procedure. It is unlikely that the outcrop was saturated to either of these values (0 and 100 %), but these measurements allow the greatest and least possible velocities to be determined. The percent saturation attained for each sample before saturated measurements were made is presented in Table 34. From Table 33 it can be seen that the velocity of the radar wave in the outcrop from these calculations likely lies between 0.09 and 0.18 m/ns. The first value corresponds to the velocity if the outcrop were entirely saturated and the second value corresponds to no saturation. Using standard statistical methods (Table 33), the 95% confidence interval for saturated samples is 0.09 $\pm$0.02 m/ns. The 95% confidence interval for unsaturated samples is 0.17 $\pm$0.01 m/ns. Velocities determined by other methods fall within the range for the saturated calculations. The unsaturated velocities seem unreasonable given the results from the other methods. It is likely that the actual value probably lies closer to 0.09 m/ns by this method, although complete saturation is unlikely. It is important to note that velocity is clearly not constant, based on the range of values indicated in the table. These analyses are an attempt to assign an average value to velocity. Measurements would need to be made on more specimens at closer spacing throughout the outcrop in order to adequately model velocity heterogeneity within the outcrop, and were not made due to budget considerations.

Given these three different methods of constraining the velocity, a velocity of 0.08 m/ns was used in the processing of the profiles. This value seems reasonable considering all the information collected and analyses done. For comparative purposes, Figure 26 reports typical values of the dielectric constant, electric conductivity, velocity, and attenuation for a variety of geologic materials. Theoretically, using a velocity of 0.08 m/ns allows features at the 40 cm scale to be resolved if ¼ the wavelength is expected, and at the 80 cm if ½ the wavelength is expected (see Figure 29). Error analyses for velocity (see Table 33) indicate that the velocity can be constrained to be within 0.02

Specimen		Dry Specimens K'	K''	Conductivity	Velocity (m/ns)	Saturated Specimens K'	K''	Conductivity	Velocity (m/ns)
813A		2.92254	0.198956	0.000563		4.334209	0.498213	0.001409	
		2.533121	0.113438	0.000281		3.912177	0.101314	0.000273	
	Average	2.7278305	0.156197	0.000422	0.181640448	4.123193	0.2997635	0.000841	0.147742153
G1		3.225553	0.330792	0.000848		18.38231	3.832256	0.010839	
		2.78048	0.220303	0.000565		17.16617	3.441359	0.009734	
	Average	3.0030165	0.2755475	0.0007065	0.173118068	17.77424	3.6368075	0.0102865	0.071158328
G2		3.728528	0.096558	0.000273		17.17562	4.350352	0.012305	
		3.337389	0.6643	0.001703		16.45736	3.246619	0.009183	
	Average	3.5329585	0.380429	0.000988	0.159607019	16.81649	3.7984855	0.010744	0.073156611
G3		3.22575	0.442021	0.001133		14.72842	1.849969	0.005233	
		2.892052	0.442582	0.001134		14.93382	2.251706	0.006369	
	Average	3.058901	0.4423015	0.0011335	0.17152939	14.83112	2.0508375	0.005801	0.07789943
G4		3.336575	0.21937	0.000562		14.66425	5.991932	0.016948	
		4.546581	0.099765	0.000269		14.35911	5.792351	0.016384	
	Average	3.941578	0.1595675	0.0004155	0.15110756	14.51168	5.8921415	0.016666	0.078752148
G5		2.669261	0.22047	0.000565		22.2881	8.842345	0.02501	
		2.506695	0.237112	0.000566		22.48106	8.130661	0.022997	
	Average	2.587978	0.228791	0.0005655	0.186483737	22.38458	8.486503	0.0240035	0.063408398
G6		2.669098	0.109254	0.00028		20.60795	4.10905	0.011622	
		2.648586	0.343577	0.000851		21.51178	3.693474	0.010447	
	Average	2.658842	0.2264155	0.0005655	0.183981853	21.059865	3.901262	0.0110345	0.065372255
G7		3.448214	0.441614	0.001132		15.13839	2.552595	0.00722	
		3.222892	0.236062	0.000564		13.51709	1.759447	0.004977	
	Average	3.335553	0.338838	0.000848	0.164262085	14.32774	2.156021	0.0060985	0.079256047
G8		2.303259	0.45919	0.001137		5.140255	0.395107	0.001118	
		2.446674	0.109566	0.000281		4.716949	0.281712	0.000834	
	Average	2.3749665	0.284378	0.000709	0.194667078	4.928602	0.3384095	0.000976	0.135132366
G9		2.335461	0.109712	0.000281		13.33408	4.082729	0.011548	
		2.506695	0.237112	0.000566		12.32169	3.787561	0.010713	
	Average	2.421078	0.173412	0.0004235	0.192804366	12.827885	3.935145	0.0111305	0.083761361
G10		2.891699	0.22013	0.000564		12.8063	1.159963	0.003281	
		2.78048	0.220303	0.000565		12.2013	1.164544	0.003294	
	Average	2.8360895	0.2202165	0.0005645	0.178139935	12.5038	1.1622535	0.0032875	0.084839919
G11		1.334631	0.221936	0.000569		3.595413	0.313482	0.000845	
		2.187829	0.229015	0.000567		3.172425	0.314309	0.000847	
	Average	1.76123	0.2254755	0.000568	0.226054532	3.383919	0.3138955	0.000846	0.16308397
G12		3.447793	0.219163	0.000562		11.40437	2.582595	0.007305	
		3.799678	0.111312	0.000276		12.82353	3.379792	0.00956	
	Average	3.6237355	0.1652375	0.000419	0.157595209	12.11395	2.9811935	0.0084325	0.086194264
G13		3.670455	0.32995	0.000846		11.40577	2.784449	0.007876	
		3.915536	0.456532	0.00113		10.39135	1.983837	0.005611	
	Average	3.7929955	0.393241	0.000988	0.154038787	10.89856	2.384143	0.0067435	0.090873383
G14		4.132619	0.49873	0.001411		16.71746	9.00933	0.025483	
		3.829532	0.197101	0.000557		14.99055	8.519346	0.024097	
	Average	3.9810755	0.3479155	0.000984	0.150356098	15.854005	8.764338	0.02479	0.075344535
				Average=	0.175025744			Average=	0.091731678

Unsaturated Specimens	
Mean	0.175025744
Standard Error	0.005284818
Median	0.173118068
Mode	#N/A
Standard Deviation	0.020468011
Sample Variance	0.000418939
Kurtosis	1.307940126
Skewness	0.965152679
Range	0.075698433
Minimum	0.150356098
Maximum	0.226054532
Sum	2.625386166
Count	15
Confidence Level(95.0%)	0.011334817

Saturated Specimens	
Mean	0.091731678
Standard Error	0.007959321
Median	0.079256047
Mode	#N/A
Standard Deviation	0.030826319
Sample Variance	0.000950262
Kurtosis	1.208420887
Skewness	1.554198722
Range	0.099675572
Minimum	0.063408398
Maximum	0.16308397
Sum	1.375975168
Count	15
Confidence Level(95.0%)	0.017071061

Table 33: Electrical measurements (at 50 MHz) and calculated velocities for the 15 samples from Section G. Values for the two trials are averaged, and the average velocity using these 15 values is presented in the boxes below the table. See text for an explanation of the symbols and the formulae used.

Specimen	Gravimetric Moisture Content (%)
G1	7.0
G2	6.4
G3	6.3
G4	6.3
G5	6.8
G6	7.0
G7	6.8
G8	6.7
G9	6.3
G10	5.9
G11	7.9
G12	6.6
G13	6.7
G14	6.9
813A	6.9

Table 34: Values of the gravimetric moisture content for the specimens from Section G. These are the values that were observed after soaking the specimens in de-ionized water for 48 hours and before electrical measurements were made on the saturated specimens.

m/ns of the value used. This corresponds to an error in resolution of 10 to 20 cm (Figure 29).

3.8.3 Processing Parameters

Many different processing techniques were used to determine the optimal combination of reflector amplitude and continuity without emphasizing significant noise. Initially, all profiles were corrected to a horizontal datum corresponding to the upper surface of the bluff. The first breaks (air wave) on the radar traces were identified and shifted to a horizontal line. Various gain and filter combinations were performed to bring out the strength continuity of reflections. The final combination used for presentation here included an AGC of 1000, vertical averaging of 4 and horizontal averaging of 8. The processing parameters used for the GPR data presented in this study can be found in Figure 35. This gain brought the consistent, horizontal reflector thought to be the contact between the sands of interest and the underlying siltstone into view while enhancing the magnitude of reflectors in the zone of interest. The vertical and horizontal averaging produced the best strength and continuity of the reflectors within the zone of interest. Figure 36 shows the same portion of the radar data near Section G before and after processing. Note the enhanced continuity of internal reflectors and the basal reflector in the processed section of the profile.

3.8.4 Electrical measurement methodology

Samples collected at 50 cm intervals from Section G were analyzed for their electrical properties. Section G was chosen in order to compare the electrical data with the petrographic data for this measured section. Measurements of complex permitivity (K` and K``) as well as effective conductivity were performed by Carlos Santamaria at Georgia Tech (Appendix II). The device used was an HP 8752A with a coaxial termination probe. Measurements were made between the frequencies of 20 and 1000 MHz on specimens after they had been dried in an oven for 48 hours and again after they had been immersed in de-ionized water for 48 hours. The gravimetric moisture content

```
PulseEKKO  Data Sheet

DATA FILE #1 PARAMETERS:
   Data File  = C:\TIP\THESIS~1\FTOGPR~1\4-26.hd
   0808-E
   Pishkun Field study area
   08/02/97: 50 MHz traverse, east to west from 0.0M
   02/08/97
   NUMBER OF TRACES    = 601
   NUMBER OF PTS/TRC   = 331
   TIMEZERO AT POINT   = 19
   TOTAL TIME WINDOW   = 265
   STARTING POSITION   = 1000.000000
   FINAL POSITION      = 700.000000
   STEP SIZE USED      = -0.500000
   POSITION UNITS      = metres
   NOMINAL FREQUENCY   = 50.000000
   ANTENNA SEPARATION  = 2.000000
   PULSER VOLTAGE (V)  = 1000
   NUMBER OF STACKS    = 128
   SURVEY MODE         = Reflection
   THIS FILE A MERGING OF \20 AND C:\TIP\GPR\ULM\081597\
   FIRST BREAK POINT CORRECTED. THRESHOLD = 10000
   FIRST BREAK SHIFT APPLIED.
   SOURCE DATA FILE    = C:\TIP\GPR\ULM\COMBINE
   THIS PROFILE CLIPPED FROM ORIGINAL PROFILE.
   SOURCE DATA FILE    = C:\TIP\GPR\ULM\WORKING
   SOURCE DATA FILE    = C:\TIP\GPR\ULM\WORK819
   PROFILING DIRECTION HAS BEEN REVERSED
   SOURCE DATA FILE    = C:\TIP\GPR\ULM\TOTALL~1\REVERSE
   THIS PROFILE CLIPPED FROM ORIGINAL PROFILE.

PROCESSING SELECTED:
   Trace Stacking     : 8
   Points Stacking    : 4
   Trace Differencing: N
   Correction         : DEWOW
   Gain Type   : AGC
     Window    : 1.000  pulse widths
     Amount    : 1000 Maximum
   Selection   : Time = all
                 Position = all
   Picture Id  : 06/25/98-14:33:05

PLOT LAYOUT PARAMETERS:
   Trace Spacing      : 0.080"
   Trace Width        : 0.080"
   Trace Position     : 1.000" to 6.000"
   Left/Right Margin  : 0.500" / 0.500"
   Border Size        : 0.500"
   Page Length/Width  : 11.000" / 8.500"
   Printer Name       : HP LaserJet IV 600dpi
```

Figure 35: Data sheet indicating parameters, including processing techniques, that were used for the GPR profile presented in Plate 3. An AGC gain of 1000 with a trace stacking of 8 and a point stacking of 4 was found to be the most useful for looking at the data.

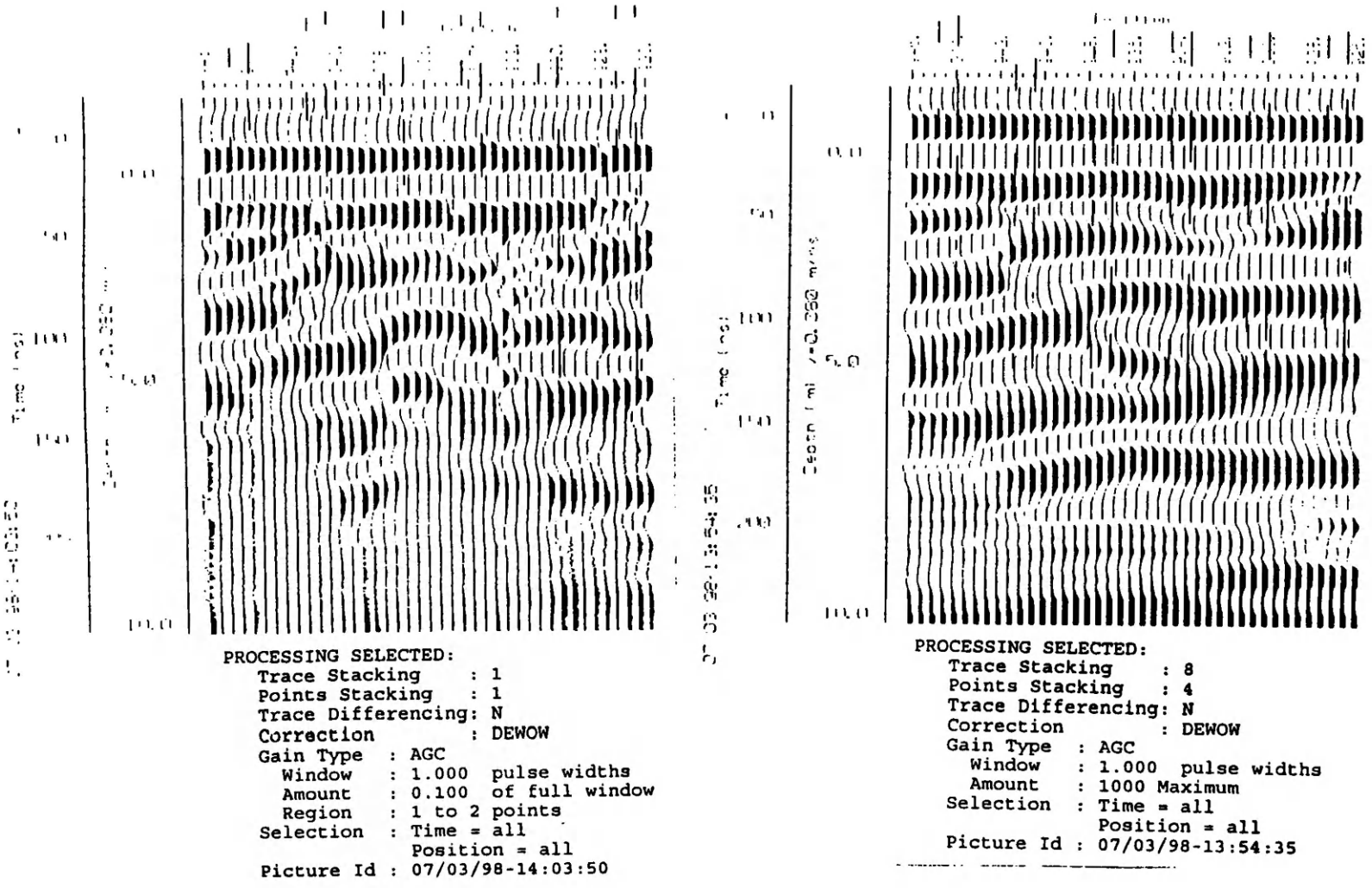

Figure 36: Radar data near Section G (936 m) showing the data before and after processing. Processing parameters can be found in Figure 35.

attained for each specimen after soaking is presented in Table 34. Both saturated and unsaturated measurements were made to bracket the possible moisture content in the outcrop. Table 33 presents the measurements of the dielectric constant and conductivity at 50 MHz (the radar survey frequency) for the 15 samples from Section G for both the saturated and unsaturated conditions. The goal of this work was to quantify the electrical properties in the samples that might consistently influence the radar signal.

Measurements of the real part of the permitivity (K`) from Section G were used to construct a synthetic radargram and to make some estimates of an average velocity of the radar wave in the deposit. The synthetic process is similar to synthetic seismograms, but uses the ratio of values of real permitivity (K`) from adjacent samples to determine a reflection coefficient between the samples. The equation used for these calculations is shown in section 3.4. Conductivity measurements were made to verify that conductive losses in the medium are low. The conductivity measurements on the dry specimens were below the limit of resolution of the device (Carlos Santamaria, 1998, personal communication). Conductivity measurements on the saturated specimens were low enough that they are unimportant when considering radar wave propagation at the site. This work was done to investigate the relationship of dielectric properties in Section G with petrographic data and reflections observed in the radar profile near Section G.

Figure 37 presents the data used to calculate the reflection coefficients for the saturated and unsaturated specimens. Figure 38 presents the reflection coefficients in a vertical profile. The results indicate that variability in the bulk electrical properties of the samples could generate reflection coefficients. Figure 38 also compares the saturated and unsaturated reflection coefficients with the radar traces and stratigraphy near measured section G. The correlation between the three data sets is encouraging. The magnitude and the polarity of the calculated responses can not be directly compared to the radar data for a couple of reasons. Firstly, the magnitude of the radar traces has been put through a gaining function. Secondly, the polarity of the synthetic traces is dependent on the degree of saturation (compare the unsaturated and saturated plots). As the exact saturation of the outcrop is unknown, direct correlation of polarity is not possible. The utility of the synthetic data is to illustrate that differences in the electrical properties of adjacent beds

Specimen	Location in cm from the top of the exposure	K` (unsaturated)	K` (saturated)	Reflection Coefficient (unsaturated)	Reflection Coefficient (saturated)
G14	10	3.98	15.85		
G13	60	3.79	10.90	0.012	0.093
G12	110	3.62	12.11	0.011	-0.026
G11	160	1.76	3.38	0.178	0.308
G10	215	2.84	12.50	-0.119	-0.316
G9	250	2.42	12.83	0.040	-0.006
G8	310	2.37	4.93	0.005	0.235
G7	360	3.34	14.33	-0.085	-0.261
G6	420	2.66	21.06	0.057	-0.096
813A	655	2.73	4.12	-0.006	0.387
G5	705	2.59	22.38	0.013	-0.399
G4	755	3.94	14.51	-0.105	0.108
G3	810	3.06	14.83	0.063	-0.005
G2	855	3.53	16.82	-0.036	-0.031
G1	905	3.00	17.77	0.041	-0.014

Figure 37: Data used to calculate the shown reflection coefficients. Formula used shown in Chapter 3. For location of specimens in Section G see Figure 7. To construct the radargram, these coefficients were plotted at the most prominent bedding contact between the location of the two samples.

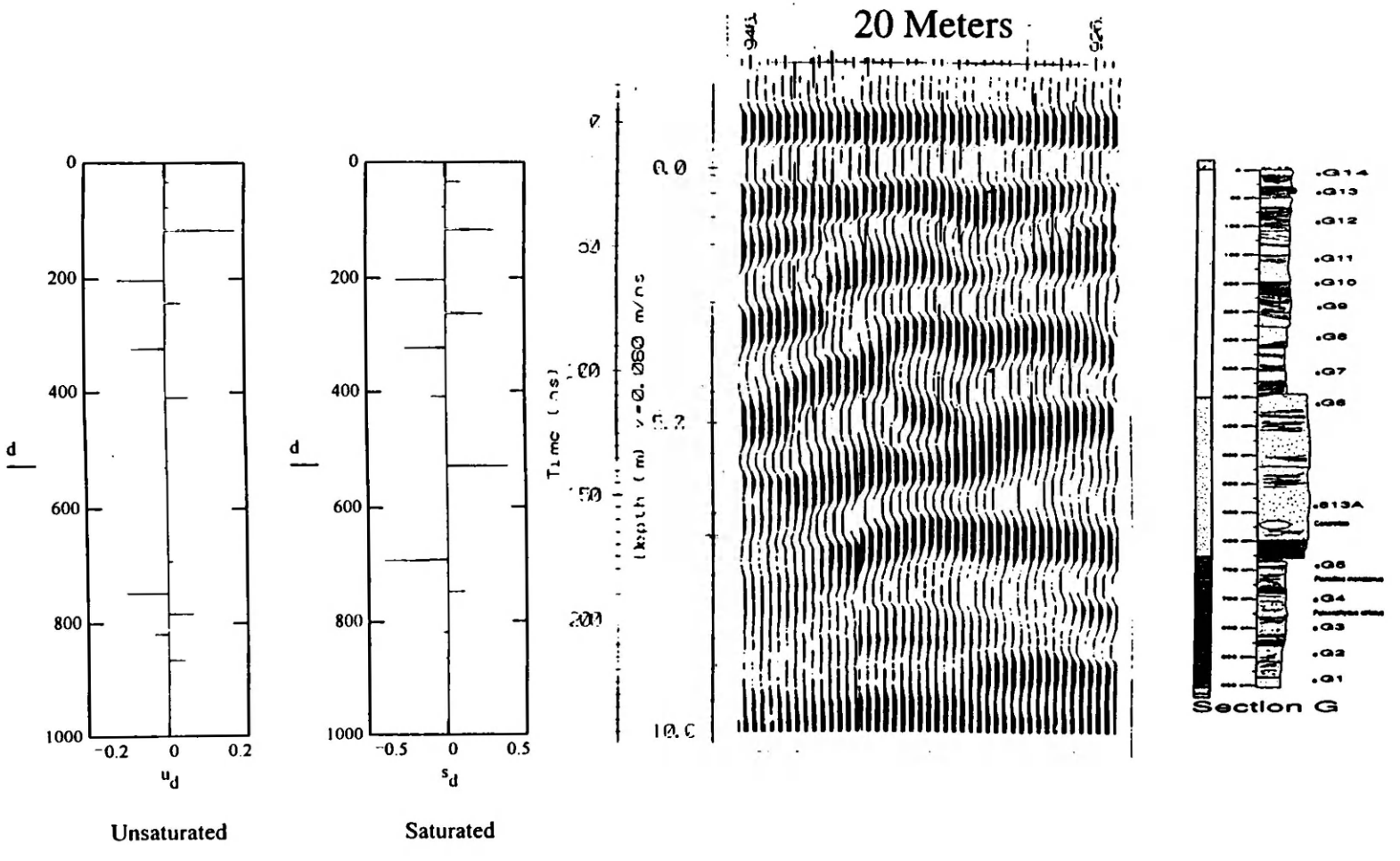

Figure 38: Comparison of the radargrams generated for the saturated and unsaturated specimens compared to the radar traces and measured Section G.

can cause reflections. The position of these reflections correlates well with radar reflections. Thus, physical properties of samples can be related to calculated reflection coefficients and further related to radar reflections. The reflection coefficients are used as a proxy for the radar traces when relating the traces to changes in physical properties of the samples. Keep in mind that neither saturation is probably representative of the outcrop, and the most realistic synthetic is probably a combination of the two traces.

3.9 Presentation and Interpretation of GPR Data

The entire radar data set can be found in Appendix III on 31/2 inch disk. This disk can be read by PulseEKKO IV software not included on the disk for copyright reasons. The file is titled 'Whole Line', and it contains data for 1590 meters. For the purposes of discussion, only the data between Section F and G will be presented in a hard copy. Plate 3 presents the radar data between Section F and G. Note the pair of laterally consistent reflectors of opposite polarity that begin in the upper part of the profile at the right and dip downward to the left (west), apparently terminating into the continuous, basal reflector. The upper reflector is labeled 'A' and the lower is 'B'.

For the simplicity of this paper, only the radar data between Sections F and G will be commented on directly. Tracings of a photo-mosaic and GPR data for this area are presented in the included plates. This part of the outcrop was the focus of GPR interpretation because it contains the most striking geometry in the study area. Specifically, the Massive Sandstone facies exists at the top of the exposure in the vicinity of F, and works down the exposure to the west (left), where it exists at the bottom of the exposure at G. The radar data shows an analogous surface dipping down to the west (Plate 3).

After careful work converting the two way travel time section into a depth section, the westward dipping reflector could be correlated directly to the measured sections and tracing of the photo-mosaic. The striking, continuous reflector (labeled B) is interpreted to be the contact between the Low Angle Cross-bedded Sandstone and Massive Sandstone facies in both measured sections F and G.

The overall correlation of smaller-scale bedding surfaces with radar reflections in other parts of the profile is not quite as convincing, and it appears likely that the resolution of the 50 MHz radar in this environment was only capable of detecting major bounding surfaces. This phenomenon has prompted others to interpret radar data with a more general 'radar facies' concept (Baker, 1991a). These facies are "groups of radar reflections whose descriptors (configuration, amplitude, continuity, frequency, interval velocity, attenuation, and dispersion) differ from adjacent groups" (Baker, 1991a). Considering only the first three of these, the radar data between Sections F and G can be broken into three radar facies.

Beginning at the base of the radar profile (Plate 3) and working upward, radar facies 1 (R1) can be described as discontinuous, medium- to small-scale, subhorizontal to westward-dipping events. The second radar facies (R2) consists of a pair of almost completely continuous reflectors of opposite polarity approximately 2 m apart and sub-parallel, also dipping to the west. The third (R3) is similar to the first, but exists above the second, separated from the first completely. The upper reflectors truncate against the ground surface where the survey was performed and Chert Pebble facies crops out. All the radar facies are apparently in angular relationship with the underlying, basal reflector and upper, horizontal surface. The downward bulge (X in Plate 3) in the traces around 876 meters was probably caused by a slight topographic high on the top of the cliff in this area. An increase in distance to the dipping reflector would cause delay in the arrival time and downward offset of the reflectors. Correction for small topographic features like this was not conducted in this study.

The R1 facies is correlated with the Pinch and Swell Sandstone and Low Angle Cross-bedded to Planar Laminated Sandstone lithofacies. Distinction between these two facies is not seen because of the overall similarity of the scale and continuity of the beds between the two facies. The R2 facies is correlated with the Massive facies based on its continuity and constant amplitude. The R3 facies is correlated with the Muddy Trough Cross-Bedded facies. The continuous nature of R2 is distinct from the more discontinuous reflections of R1 and R3 because the Massive facies has a consistent thickness, sharp contact with the adjacent facies, and is continuous within the outcrop.

The small scale of bedding and lateral discontinuity likely caused radar reflections in facies R1 and R3 to be discontinuous. If these radar facies indeed can be correlated with the lithofacies, then the angular relationship of the radar facies with the basal reflector suggests that the lithofacies downlap onto the Siltstone facies and dip west, as seen in the field.

There are many reflections within the data that could not be correlated directly with bedding surfaces. This observation prompted a major line of inquiry while looking at the radar data: what physical attributes in the outcrop influence dielectric properties and cause radar reflections? This subject is addressed below.

3.10 Relation of Physical Rock Properties to GPR Reflections

Many of the calculated reflection coefficients correspond to bounding surfaces in the outcrop (Figure 38). This may be an artifact of the method used. Differences in measured electrical properties were used to calculate a reflection coefficient, which was plotted at the most prominent bedding contact between the measurements because this was thought to be the most reasonable location for a change in electrical impedance (Meyers, 1994). This led to the question of what characteristics of the rocks were actually influencing the electrical properties.

Meyers (1994) states that it is presently unknown whether GPR reflection patterns indicate variation in lithology, porosity, permeability, pore fluid content or some other material property (Knoll and others, 1992). Data from the point counts of the 15 thin sections from Section G are presented in Figure 39. The point count method used was that of Gazzi (1966) and Dickinson (1970). Figure 40 shows two photo-micrographs as representations of the thin sections from Section G. Figure 41 shows the modal percent composition of each sample at the location of the sample in the vertical section G. Monocrystalline quartz is the dominant constituent, followed by chert and potassium feldspar. Appendix I presents plots relating 100 times the reflection coefficient (for viewing purposes) for both the saturated and unsaturated specimens to the changes in composition between the samples that were used to generate the coefficient in these plots.

RAW DATA

Sample#	Qm	Cht.	K	P	Lv	Lsed	bt	ms	heav.	Cmt	Matr.	cmt+ma	Unid T	Porosity
G-14	241	120	57	2	6	11	1	0	1	45	16	61	0	14.4
G-13	234	131	54	4	9	6	4	0	1	34	23	57	0	11.7
G-12	239	125	37	5	11	2	4	0	2	50	24	74	1	13.6
G-11	233	132	54	4	2	11	1	0	2	52	9	61	0	20.5
G-10	226	118	81	3	3	8	1	0	0	57	3	60	0	15.4
G-9	216	144	61	2	5	9	4	0	2	55	2	57	0	14.2
G-8	226	126	56	3	6	6	6	1	2	52	16	68	0	13.2
G-7	213	170	45	1	9	2	2	0	1	50	7	57	0	16.5
G-6	215	163	68	3	1	3	9	0	3	27	8	35	0	11.5
813A	274	119	43	3	1	3	6	0	1	39	11	50	0	12.4
G-5	248	156	44	2	4	4	1	0	1	31	9	40	0	12.3
G-4	258	129	50	6	6	13	2	0	0	33	3	36	0	13.6
G-3	266	100	58	12	6	7	1	0	0	50	0	50	0	18.4
G-2	256	121	57	8	17	5	3	0	2	30	1	31	0	20.6
G-1	238	147	43	10	5	1	6	0	5	29	14	43	2	13.6
STDEV:	18.65	19.03	11.15	3.18	4.18	3.71	2.47	0.26	1.30	10.71	7.61	12.71	0.56	2.96

TERNARY DATA

Sample#	QM	F	LT	QT	F	L	QP	LV	LSM	QM	P	K
G-14	55.1	13.5	31.4	82.6	13.5	3.9	87.6	4.4	8.0	80.3	0.7	19.0
G-13	53.4	13.2	33.3	83.3	13.2	3.4	89.7	6.2	4.1	80.1	1.4	18.5
G-12	57.0	10.0	32.9	86.9	10.0	3.1	90.6	8.0	1.4	85.1	1.8	13.2
G-11	53.4	13.3	33.3	83.7	13.3	3.0	91.0	1.4	7.6	80.1	1.4	18.6
G-10	51.5	19.1	29.4	78.4	19.1	2.5	91.5	2.3	6.2	72.9	1.0	26.1
G-9	49.4	14.4	36.2	82.4	14.4	3.2	91.1	3.2	5.7	77.4	0.7	21.9
G-8	53.4	13.9	32.6	83.2	13.9	2.8	91.3	4.3	4.3	79.3	1.1	19.6
G-7	48.4	10.5	41.1	87.0	10.5	2.5	93.9	5.0	1.1	82.2	0.4	17.4
G-6	47.5	15.7	36.9	83.4	15.7	0.9	97.6	0.6	1.8	75.2	1.0	23.8
813A	61.9	10.4	27.8	88.7	10.4	0.9	96.7	0.8	2.4	85.6	0.9	13.4
G-5	54.1	10.0	35.8	88.2	10.0	1.7	95.1	2.4	2.4	84.4	0.7	15.0
G-4	55.8	12.1	32.0	83.8	12.1	4.1	87.2	4.1	8.8	82.2	1.9	15.9
G-3	59.2	15.6	25.2	81.5	15.6	2.9	88.5	5.3	6.2	79.2	3.6	17.3
G-2	55.2	14.0	30.8	81.3	14.0	4.7	84.6	11.9	3.5	79.8	2.5	17.8
G-1	53.6	11.9	34.5	86.7	11.9	1.4	96.1	3.3	0.7	81.8	3.4	14.8
STDEV:	3.84	2.51	3.89	2.88	2.51	1.13	3.78	2.93	2.67	3.47	0.98	3.66

Figure 39: Point count data from 15 thin sections from Section G. Qm=monocrystalline quartz, Cht.=chert, K=potassium feldspar, P=plagioclase feldspar, Lv=lithic volcanic, Lsed=lithic sedimentary, bt=biotite, ms=muscovite, heav.=heavy mineral, cmt=cement, Matr.=matrix, Unid T=total grains unidentified. For Ternary data: QM=monocrystalline quartz, F=feldspar, LT=lithic total, QT=quartz total, L=lithic, Qp=polycrystalline quartz, LV=lithic volcanic, LSM=lithic sedimentary, P=plagioclase feldspar, K=potassium fedspar.

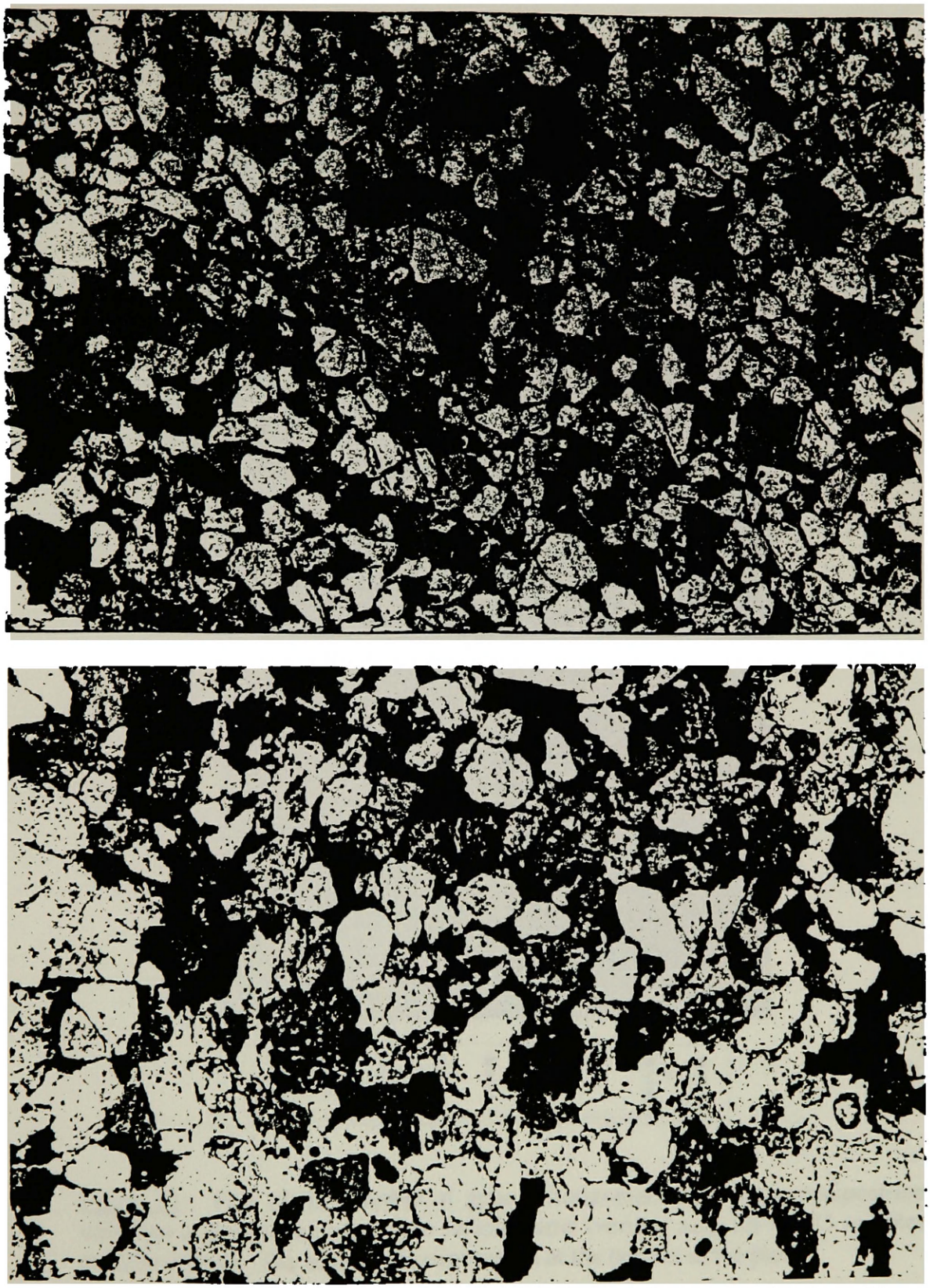

Figure 40: Two photo-micrographs of thin sections from the study area. Upper photograph is from sample 11-3 (see Plate 1), under plain light, on the stained portion of the slide. Lower photograph from sample G-11 in plain light, on the stained portion of the slide. Horizontal distance is approximately 1.5 cm.

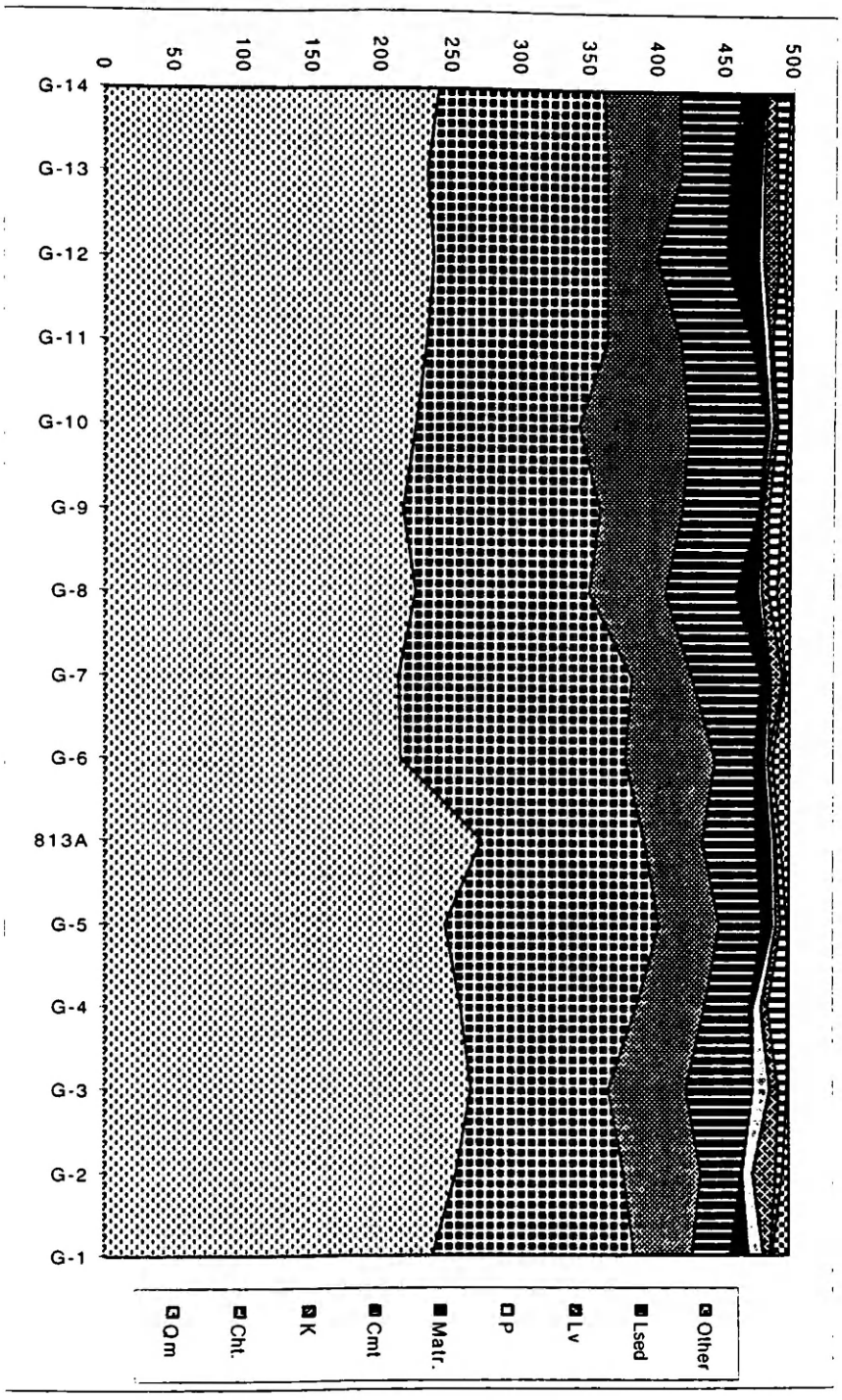

Figure 41: Plot of the number of grains (horizontal axis) of the composition indicated at the bottom versus the sample name (vertical axis) for the 15 samples from Section G. The base of the exposure is at the bottom of the plot.

Only the plots for the attributes of the slides that changed most significantly are included. Of all the major framework constituents, the abundance of monocrystalline quartz seems to correlate most notably with the magnitude of the reflection coefficient calculated from saturated specimens (Figure 42).

The grain size of the samples from Section G did not vary at a scale that was considered significant enough to warrant quantification. All the specimens are composed of lower medium to upper fine sand that is sub-angular to well-rounded and well-sorted.

The cement characteristics of the slides was also quite similar. The amount of cementation (dominantly silica with minor calcite exclusively) in each thin section was estimated visually using the point count method (Gazzi, 1966; Dickinson, 1970; Ingersoll, 1964). Within the suite of thin sections, the volume of cement varied from 5% to 12%. Yet, the variability of cement volume between samples did not appreciably affect the reflection coefficients calculated from the electrical measurements (Figure 43). Since the calculated reflection coefficients are the best approximation for the reflections in the radar profile (see section 3.8.4), the variability in the volume of cement did not likely influence the reflections seen in the radar profile.

Percent porosity values were recorded during thin section analysis and do not correlate significantly with the synthetic reflection coefficients calculated (Figure 44). Baker (1991a) indicated that minor changes in porosity (affecting the degree of saturation) give relatively small reflection coefficients that still may be detectable. For the samples from Section G, changes in the calculated reflection coefficients can sometimes be related to changes in porosity but not in a systematic way that provided any predictability.

Stephens (1991) concluded from his study in consolidated sandstone that the reflections he obtained were caused by changes in water content. Yet, direct evidence for this is not presented in his paper. With regard to the effect the variation in saturation has on radar response, Davis and Annan (1989) indicated that volumetric water content may give rise to radar reflections. In order to investigate whether water content may relate to synthetic reflections generated in this study in a systematic way, the changes in the moisture content from sample to sample for each of the saturated specimens were

100X Saturated Refl. Coeff	Delta Qm
-39.94	-26
-1.38	-18
-26.06	-14
-0.64	-10
-3.14	-10
9.34	-7
-31.56	-7
30.84	-6
-9.54	2
-2.64	5
-0.54	8
10.79	10
23.47	11
38.60	59

100X Unsaturated Refl. Coeff	Delta Qm
1.32	-26
4.06	-18
-8.47	-14
3.95	-10
-3.60	-10
1.21	-7
-11.85	-7
17.84	-6
5.66	2
1.14	5
6.33	8
-10.48	10
0.48	11
-0.64	59

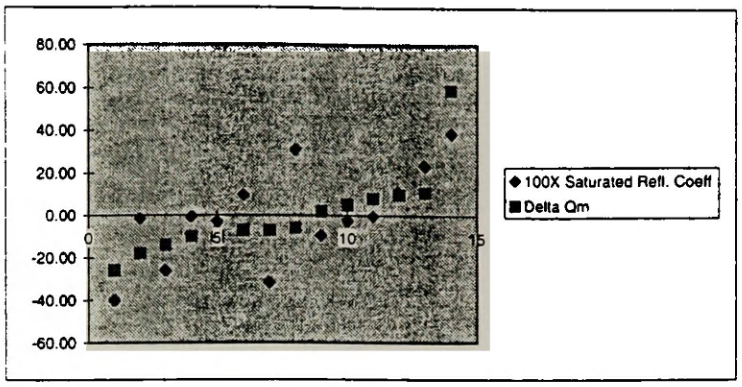

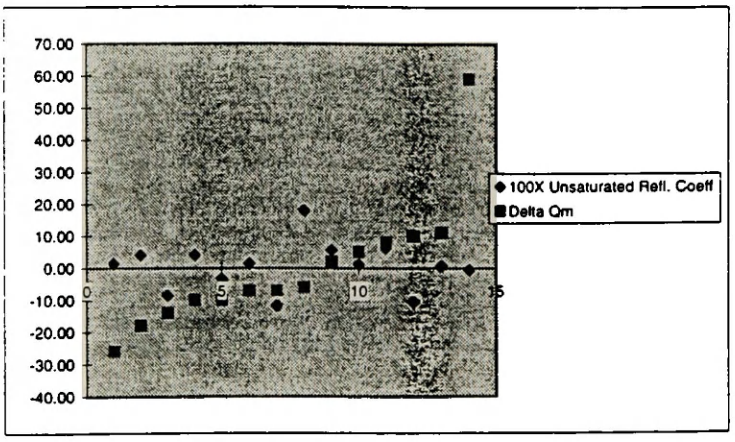

Figure 42: Plot relating the change in number of monocrystalline quartz grains from sample to sample with the associated reflection coefficient (both from saturated and unsaturated specimens) calculated between adjacent samples for Section G. The horizontal scale is the number of each reflection coefficient, and the vertical scale indicates the values for the characteristics shown at the right. Delta Qm is the change in the number of monocrystalline quartz grains from adjacent samples moving down the vertical section. Each reflection coefficient can be identified and related to the measured section using Appendix III and Figure 7.

100X Saturated Refl. Coeff	Delta Cement
-9.54	-23
-3.14	-20
9.34	-11
-39.94	-8
23.47	-3
-0.64	-2
-26.06	-2
-1.38	-1
30.84	2
10.79	2
-31.56	5
38.60	12
-2.64	16
-0.54	17

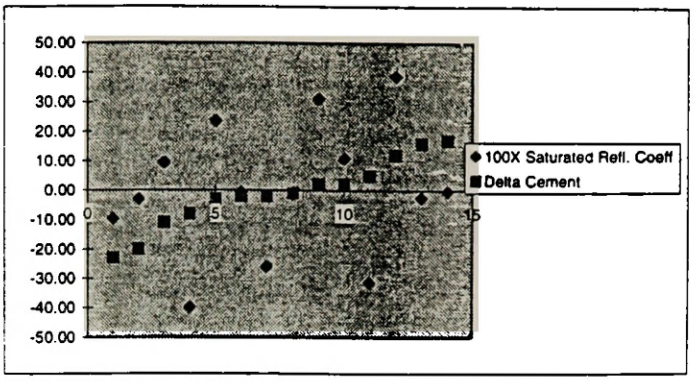

100X Unsaturated Refl. Coeff	Delta Cement
5.66	-23
-3.60	-20
1.21	-11
1.32	-8
0.48	-3
3.95	-2
-8.47	-2
4.06	-1
17.84	2
-10.48	2
-11.85	5
-0.64	12
1.14	16
6.33	17

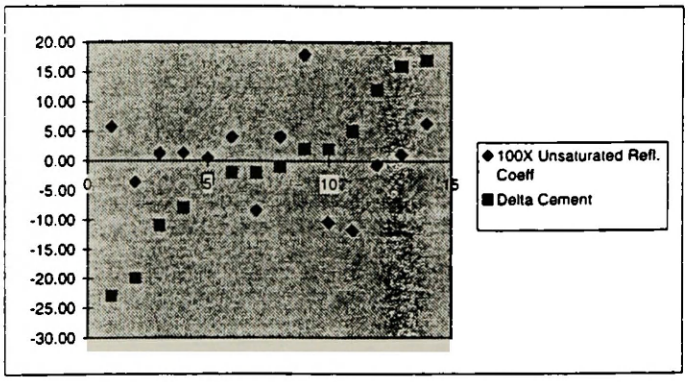

Figure 43: Plot relating the change in amount of cement from sample to sample with the associated reflection coefficient (both from saturated and unsaturated specimens) calculated between adjacent samples for Section G. The horizontal scale is the number of each reflection coefficient, and the vertical scale indicates the values for the characteristics shown at the right. Delta cement is the change in the amount of cement from adjacent samples moving down the vertical section. Each reflection coefficient can be identified and related to the measured section using Appendix III and Figure 7.

100X Saturated Refl. Coeff	Delta Porosity (%)
-1.38	-6.99
-31.56	-5.11
-9.54	-5.03
9.34	-2.72
-0.64	-1.16
23.47	-1.05
-39.94	-0.15
38.60	0.93
10.79	1.36
-2.64	1.98
-3.14	2.2
-26.06	3.34
-0.54	4.79
30.84	6.87

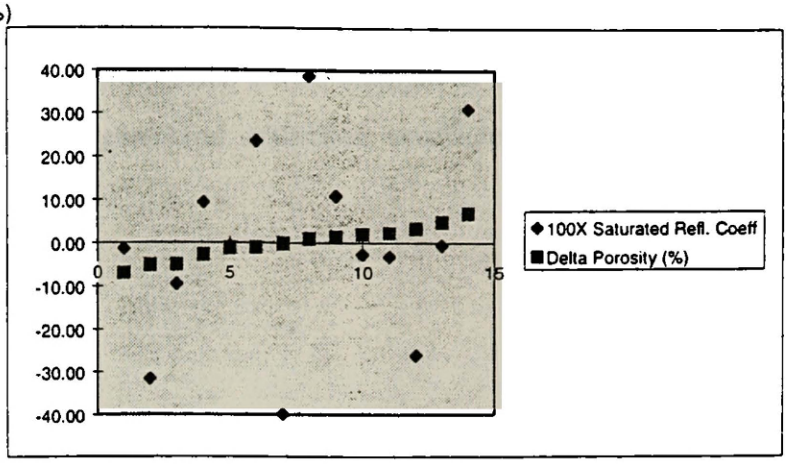

100X Unsaturated Refl. Coe	Delta Porosity(%)
4.06	-6.99
-11.85	-5.11
5.66	-5.03
1.21	-2.72
3.95	-1.16
0.48	-1.05
1.32	-0.15
-0.64	0.93
-10.48	1.36
1.14	1.98
-3.60	2.2
-8.47	3.34
6.33	4.79
17.84	6.87

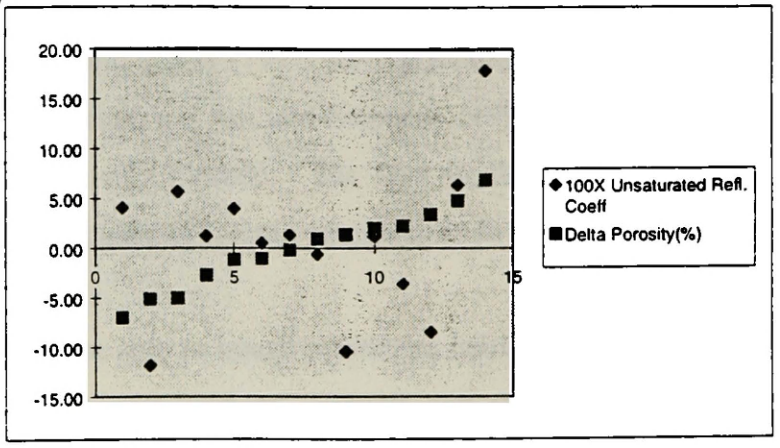

Figure 44: Plot relating the change in percent porosity from sample to sample with the associated reflection coefficient (both from saturated and unsaturated specimens) calculated between adjacent samples for Section G. The horizontal scale is the number of each reflection coefficient, and the vertical scale indicates the values for the characteristics shown at the right. Delta porosity is the change in the percent of porosity from adjacent samples moving down the vertical section. Each reflection coefficient can be identified and related to the measured section using Appendix III and Figure 7.

compared to the reflection coefficients generated between those specimens (Figure 45). The plot indicates that there does not seem to be a predictable response for the value of the reflection coefficient for a given magnitude of the moisture content. In addition, an increase or decrease in the moisture content does not seem to systematically affect changes in the reflection coefficient. The conclusion is that changes in the water content were not the overriding cause for the generated reflection coefficients in saturated specimens.

3.11 Discussion of GPR Data

In general, the quality of the radar data are quite good for a consolidated sandstone outcrop. Little work using radar in consolidated sandstone environments has been conducted to this point, but McMechan and others (1997) have presented data from the fluvial to proximal marine Ferron Sandstone in Utah and Stephens (1991) conducted a similar study in the Kayenta Formation of Colorado. The data in this study are of comparable quality to those studies, and illustrate internal architecture in as convincing a manner.

McMechan and others (1997) were able to image prominent lenticular features, a variety of lithologies, and structural elements such as channels and shale drapes that match well with those seen at the same stratigraphic levels in cliff faces adjacent to the survey. They correlated reflections with visible sedimentary structures and sequence boundaries. They concluded that low-permeability drapes of siltstone and shale over the sandstone dominated bedforms enabled GPR to image both individual bedding structures and larger depositional units (McMechan and others, 1997).

Stephens (1991) also claimed to delineate some of the major bounding surfaces in the Kayenta outcrop with GPR. He concluded that not all reflections are the direct result of the visually derived bounding surfaces, but many were related to variability in water content. He identified dominant features such as the bases of paleochannels. Because he conducted a three dimensional survey, the radar data was helpful in three-dimensional reconstruction of an ancient fluvial system.

100 X saturated reflection coeff	Change in % moisture
-31.56	-2
10.79	-0.5
9.34	-0.2
-2.64	-0.1
-39.94	-0.1
38.60	-0.1
-0.54	0
-26.06	0.1
-3.14	0.1
-9.54	0.2
-0.64	0.4
23.47	0.4
-1.38	0.6
30.84	1.3

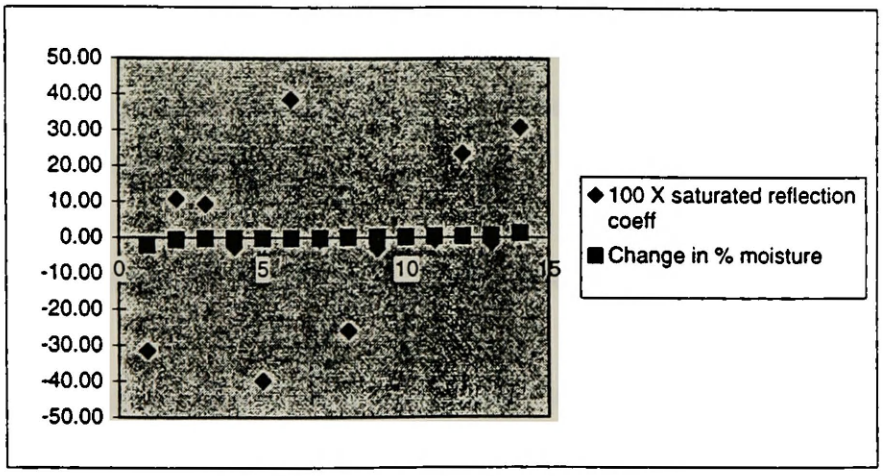

Figure 45: Plot showing the relationship of each calculated reflection coefficient with the associated change in moisture content between the saturated samples used to calculate the coefficient. The horizontal scale is the number of each reflection coefficient, and the vertical scale indicates the values for the characteristics shown at the right. Each reflection coefficient can be identified and related to the measured section using Appendix III and Figure 7.

Although many aspects of radar research in consolidated environments remain untested, the radar results from this study are encouraging, and demonstrate the degree of success that can be expected in consolidated sandstone environments. As such, this work is an advance in the understanding of the ability of radar to delineate subsurface architecture in consolidated sandstone environments. Combined with the growing number of recent studies of GPR in sandstone environments, these studies should direct the future development of GPR in these environments. One interesting outcome of this work is that with some knowledge of the causes for radar response in sandstone, future design of the technology may be able to build on this type of research in the hopes of developing a more effective tool. For example, radar being used in down-hole techniques will benefit from studies such as these. Similarly, the future of radar work in sandstone deposits will likely include more reservoir analog studies similar to McMechan and others (1997), Stephens (1991), and this one.

3.12 Future research of consolidated sedimentary deposits using GPR

There are many aspects of this study that could be focused on in detail in future studies. Previously mentioned studies have documented the response of GPR in unconsolidated environments, and results have demonstrated the ability of GPR to delineate subsurface stratigraphy. In consolidated deposits, attempts in this thesis to demonstrate the cause of GPR reflections could be further developed. Specifically, more work needs to be done to support or refute the claim in this document that bulk composition is the main factor influencing radar reflections. In addition, a similar type of project could be undertaken in a carbonate environment. The thinly bedded parts of the Mississippian Madison Formation might be a good target, or the transition from limestone to the dolomitic cap at the top of the Devonian Jefferson Formation. Diagenetic variability and its influence on GPR might be another fruitful area of research. Future work in the field with GPR should always be accompanied by other electromagnetic geophysical methods, to ensure that the site is suitable for GPR. Finally, there is some potential to integrate GPR data with models of fluid flow in heterogeneous

materials (see Knight, 1997). Attempts to use GPR data as input for engineering models may vastly improve recovery in the subsurface. Eventually, down-hole applications of GPR are likely, and may provide useful additional information for the petroleum industry.

CHAPTER 4

Conclusions

This thesis was a pilot study to explore the application of GPR to imaging of a consolidated sandstone deposit. It presents information that integrates GPR profiling with traditional sedimentary analysis methods. Specifically, it provides detailed information on the relation of radar reflections with stratigraphy and sandstone petrophysical and petrographic characteristics. Although GPR has been used to infer shallow subsurface stratigraphy in unconsolidated deposits, this work extends understanding of radar performance in consolidated sandstone deposits. Conclusions from this work relate to the sedimentology of the deposit as well as to the performance of radar in the imaging of consolidated sandstone exposures.

The following conclusions can be made regarding the sedimentologic investigation:

1) Seven distinct lithofacies that were described and indicate that the deposit shoaled upward. Energy during deposition generally increased as the deposit grew vertically.

2) Lateral profiling of the exposure with a photo-mosaic indicates that the sandy facies identified have a component of dip to the west. These facies have an angular relationship with the underlying muddy siltstone as well as the overlying coarse lag deposit, which are horizontal. The dip of the beds is not due to tectonics, but is related to topography that existed at the time of deposition. Topography of at least ten meters, with some component of dip to the west, existed in the study area at the time of deposition.

3) The internal architecture does not conform with models of nearshore/shoreface progradation proposed by Arnott and others (1995). This observation has led to an alternative hypothesis for the depositional environment of the rocks in the study area. I conclude that the rocks in the study area do not record nearshore/shoreface progradation to the east, but rather record (north)westward (shoreward) migration of an offshore sand body similar to the Cretaceous age Shannon Sandstone in Wyoming.

In addition, the following conclusions can be made based on the work done with GPR:

1) GPR was able to resolve the contact between offshore mudstones and the overlying sandstones at a depth of approximately 10 meters throughout the profile.

2) Interpretation of the GPR profile suggests that some major internal bounding surfaces can be recognized and correlated to architectural features within the sandstone outcrop. Specifically, the contact between two distinct facies was imaged and has characteristics consistent with those seen in the outcrop. Stratigraphy has significant impact on radar response.

3) Electrical measurements made on samples from one measured section were successfully used to generate synthetic traces that correspond well with reflections seen in the GPR profile, indicating that the variability of the electrical properties in the outcrop can generate radar reflections. Responses in the synthetic traces could be reasonably correlated with bedding characteristics in the outcrop.

4) For specimens from Section G that were saturated in de-ionized water for 48 hours, the changes in the degree of saturation from sample to sample could not be correlated with changes in the calculated reflection coefficients generated from electrical measurements of the same samples. This suggests that the variability of water content (when the rocks are completely saturated) can not solely explain radar reflections.

5) Changes in the amount of cement from sample to sample in Section G, as estimated from thin section, could not be correlated with changes in the calculated reflection coefficients. It is therefore unlikely that cementation characteristics contributed significantly to radar response in this study.

6) Changes in porosity between the specimens used to generate the synthetic responses were not correlated convincingly with the calculated reflection coefficients. Thus, porosity variability at the resolution recorded in this study does not likely influence radar reflections.

7) Petrographic data indicate that composition is the most consistent characteristic associated with responses in synthetic traces generated from measurements of the electrical properties of samples from one measured section, though the data do not support this conclusion overwhelmingly. Monocrystalline quartz is the most abundant

framework grain, and its abundance seems to correlate with calculated reflections coefficients for saturated specimens most convincingly.

8) Radar reflections in this study are likely caused by a combination of vertical variability of framework composition and the stratigraphy of the outcrop.

REFERENCES

Annan, A. P., and others, 1984. Radar mapping of buried pipes and cables. Sensors and Software, Inc., Mississauga, Ontario, Technical Note 1.

Annan, A. P., and Davis, J. L., 1976. Impulse radar sounding in permafrost. Radio Science, V. 11, No. 4, p. 383-394.

Annan, A. P., and Davis, J. L., 1977. Radar range analysis for geological materials. Report of Activities, Part B; Geological Survey of Canada, Paper 77-1B, p. 117-124.

Arcone, S. A., 1996. High resolution of glacial ice stratigraphy: a ground-penetrating radar study of Pegasus runway, McMurdo Station, Antarctica. Geophysics, V. 61, No. 6, p. 1653-1663.

Arnott, R.W.C., 1987. Sedimentology of an ancient clastic nearshore sequence, lower Cretaceous Bootlegger Member, north-central Montana. Doctoral Thesis, The University of Alberta. 267 p.

Arnott, R.W.C., 1992. Ripple cross-stratification in swaly cross-stratified sandstones of the Chungo Member, Mount Yamnuska, Alberta. Canadian Journal of Earth Sciences, V. 29, p. 1802-1805.

Arnott, R.W.C., 1993. Quasi-planar-laminated sandstone beds of the lower Cretaceous Bootlegger Member, North-Central Montana: evidence of combined flow sedimentation. Journal of Sedimentary Petrology, V. 63, No. 3, p. 488-494.

Arnott, R.W.C., and others, 1995. Influence of the ancestral Sweetgrass Arch on sedimentation of the lower Cretaceous Bootlegger Member, North-Central Montana. Journal of Sedimentary Petrology, V. B65, No. 2, p. 222-234.

Baker, P. L., 1991a. Response of ground-penetrating radar to bounding surfaces and lithofacies variations in sand barrier sequences. Exploration Geophysics, V. 22, p. 19-22.

Baker, P. L., 1991b. Fluid, lithology, geometry, and permeability information from ground-penetrating radar for some petroleum industry applications. Society of Petroleum Engineers of AIME, Special Paper No. 22976, 11 p.

Beres, M., and Haeni, F. P., 1991. Application of ground-penetrating-radar methods in hydrogeologic studies. Ground Water, V. 29, No. 3, p. 375-386.

Beres, M., and others, 1995. Mapping the architecture of glaciofluvial sediments with three-dimensional georadar. Geology, V. 23, No. 12, p. 1087-1090.

Bourgeois, J., 1980. A transgressive shelf sequence exhibiting hummocky stratification" the Cape Sebastian sandstone (Upper Cretaceous), southwestern Oregon. Journal of Sedimentary Petrology, V. 50, No. 3, p. 681-702.

Boyles, J.M., and Scott, A.J., 1982. A model for migrating shelf-bar sandstones in upper Mancos Shale (Campanian), Northwestern Colorado. AAPG Bulletin, V. 66, No. 5, p. 491-508.

Brenner, R.L., 1978. Sussex Sandstone of Wyoming-example of Cretaceous offshore sedimentation. AAPG Bulletin, V. 62, No. 2, p. 181-200.

Bridge, J.S., and others, 1995. Ground-penetrating radar and coring used to study the large-scale structure of point bar deposits in three dimensions. Sedimentology, V. 42, p. 839-852.

Campbell, C. V., 1971. Depositional model- upper Cretaceous Gallup Beach Shoreline, Ship Rock Area, Northwestern New Mexico. Journal of Sedimentary Petrology, V. 41, No. 2, p. 395-405.

Cobban, W. A., and others, 1959. Revision of Colorado Group on Sweetgrass Arch, Montana. AAPG Bulletin, V. 43, No. 12, p. 2786-2796.

Cobban, W. A., and others, 1976. Type Sections and Stratigraphy of the Members of the Blackleaf and Marias River Formations (Cretaceous) of the Sweetgrass Arch, Montana. USGS Professional Paper, 66 p.

Cosgrave, T. M., and others, 1987. Shallow stratigraphic reflections from ground-penetrating radar. First National Outdoor Action conference on Aquifer Restoration, Ground Water Monitoring, and Geophysical Methods, Las Vegas, Nevada, p. 555-569.

Davis, J. L., and Annan, A. P., 1989. Ground penetrating radar for high-resolution mapping of soil and rock stratigraphy. Geophysical Prospecting, V. 37, p. 531-551.

Davis, H. R., and Byers, C. W., 1989. Shelf sandstones in the Mowry Shale: evidence for deposition during Cretaceous sea level falls. Journal of Sedimentary Petrology, V. 59, No. 4, p. 548-560.

Dickinson, W. R., 1970. Interpreting Detrital Modes of Greywacke and Arkose. Journal of Sedimentary Petrology, V. 40, p. 695-707.

Dominic, D. F., and others, 1995. Delineation of shallow stratigraphy using ground penetrating radar. Journal of Applied Geophysics, V. 33, p. 167-175.

Duke, W.L., 1985. Hummocky cross-stratification, tropical hurricanes, and intense winter storms. Sedimentology, V. 32, p. 167-194.

Ericksen, M. C., and Slingerland, R., 1990. Numerical simulations of tidal and wind-driven circulation in the Cretaceous Interior Seaway of North America. Geological Society of America Bulletin, V. 102, p. 1499-1516.

Folinsbee, R.E., and others, 1963. Dating volcanic ash beds (bentonites) by the K-Ar method. National Academy of Science, National Research Council, Washington, D.C., Nuclear Sciences Series, Report No. 38, p. 70-82.

Friedman, G. M., and others, 1992. Principles of sedimentary deposits, stratigraphy and sedimentology. Macmillan Publishing Company, New York, New York, 717 p.

Gawthorpe, R.L., and others, 1993. Ground penetrating radar: application to sandbody geometry and heterogeneity studies. In: North, C.P., and Prosser, D.J., (eds), *Characterization of fluvial and eolian reservoirs*, Geological Society Special Publication No. 73, p. 421-432.

Gaynor, G.C., and Swift, D.J.P., 1988. Shannon sandstone depositional model: sand ridge dynamics on the Campanian western interior shelf. Journal of Sedimentary Petrology, V. 58, No. 5, p. 868-880.

Gazzi, P., 1966. Le Arenarie del Flysch Sopracretaceo dell'Appennino modenese; Correlazioni con il Flysch di Monghidoro. Mineralog. Et Petrog. Acta, V. 16, p. 69-97.

Grasmueck, M., 1996. 3-D Ground penetrating radar applied to fracture imaging in gneiss. Geophysics, V. 61, No. 4, p. 1050-1064.

Greaves, R. J., and others, 1996. Velocity variations and water content estimated from multi-offset, ground-penetrating radar. Geophysics, V. 61, No. 3, p. 683-695.

Hanninen, P., and Autio, S., eds., 1992. Fourth international conference on ground penetrating radar June 8-13, 1992. Rovaniemi, Finland. Geological Society of Finland, Special Paper 16, 365 p.

Haq, B.U., and others, 1987. Chronology of fluctuating sea levels since the Triassic. Science, V. 235, p. 1156-1166.

Hobday, D. K., and Reading, H. G., 1972. Fair weather versus storm processes in shallow marine sand bar sequences in the Late Precambrian of Finnmark, North Norway. Journal of Sedimentary Petrology, V. 42, No. 2, p. 318-324.

Huffman III, A. C., 1992. Characterization of three-dimensional geologic heterogeneities using ground penetrating radar. MS Thesis, Department of Geophysics, Colorado School of Mines, Golden, 189 p.

Hubbard, S. S., and others, 1997. Estimation of permeable pathways and water content using tomographic radar data. The Leading Edge, The Society of Exploration Geophysicists, V. 16, No. 11, p. 1623-1628.

Huggenberger, P., and others, 1994. Ground-probing radar as a tool for heterogeneity estimation in gravel deposits: advances in data-processing and facies analysis. Journal of Applied Geophysics, V. 31, p. 171-184.

Ingersoll, R. V., 1984. The Effect of Grain Size on Detrital Modes: a Test of the Gazzi-Dickinson Point Counting Method. Journal of Sedimentary Petrology, V. 54, p. 103-116.

Jewell, P. W., 1996. Circulation, salinity, and dissolved oxygen in the Cretaceous North American seaway. American Journal of Science, V. 296, p. 1093-1125.

Johnson, H. D., 1977. Shalow marine sand bar sequences: an example from the Late Precambrian of North Norway. Sedimentology, V. 24, p. 245-270.

Jol, H. M., 1993. Ground penetrating radar (GPR): a new geophysical methodology used to investigate the internal structure of sedimentary deposits (field experiments on lacustrine deltas). Ph.D. Dissertation, University of Calgary, Calgary, Alberta, Canada.

Jol, H. M., 1995. Ground enetrating radar antennae frequencies and transmitter powers compared for penetration depth, resolution and reflection continuity. Geophysical Prospecting, V. 43, p. 693-709.

Jol, H. M., and Smith, D. G., 1991. Ground penetrating radar of northern lacustrine deltas. Canadian Journal of Earth Sciences, V. 28, p. 1939-1947.

Jol, H. M., and Smith, D. G., 1995. Ground penetrating radar surveys of peatlands for oilfield pipelines in Canada. Applied Geophysics, V. 34, p. 109-123.

Jol, H. M., and others, 1996. Digital ground penetrating radar (GPR): a new geophysical tool for coastal barrier research (examples from the Atlantic, Gulf and Pacific Coasts, U.S.A.). Journal of Coastal Research, V. 12, No. 4, p. 960-968.

Knight, R. J., and Nur, A., 1987. The dielectric constant of sandstones, 60 kHz to 4 MHz. Geophysics, V. 52, No. 5, p. 644-654.

Knight, R., and others, 1997. The role of ground penetrating radar and geostatistics in reservoir description. The Leading Edge, The Society of Exploration Geophysicists, V. 16, No. 11, p. 1576-1582.

Knoll, M., and others, 1992. 3-D imaging of a sand and gravel aquifer using ground penetrating radar. Proceedings, CSEG National Convention: Visions of the Future, Calgary, Alberta, May 5-8, 1992. Pp. 13-14.

Lang, H. R., and McGugan, A., 1988. Cretaceous (Albian to Turonian) Foraminiferal Biostratigraphy and Paleogeography of Northern Montana and Southern Alberta. Canadian Journal of Earth Sciences, V. 25, p. 316-342.

Liner, C. L., and Liner, J. L., 1997. Application of GPR to a site investigation involving shallow faults. The Leading Edge, The Society of Exploration Geophysicists, V. 16, No. 11, p. 1649-1651.

Lynch, D.A., 1994. High-frequency sea-level changes and benthic oxygen levels in the Cretaceous Greenhorn Sea; a sedimentological and ichnological approach. GSA Abstracts with Programs, V. 26 (7), p. 494.

McMannis, W. J., 1965. Reume of depositional and structural history of western Montana. Bulletin of the American Association of Petroleum Geologists, V. 49, No. 11, p. 1801-1823.

McMechan, G.A., and others, 1997. Use of ground-penetrating radar for 3-D sedimentological characterization of clastic reservoir analogs. Geophysics, V. 62, No. 3, p. 786-796.

Meyers, R. A., 1994. The Willapa Barrier Spit of S.W. Washington State: depositional processes inferred from ground penetrating radar. M.Sc. Thesis, The Universtity of Calgary, Calgary, Alberta, Canada. 101 p.

Meyers, R. A., and others, 1996. Evidence for eight great earthquake-subsidence events detected with ground-penetrating radar, Willapa Barrier, Washington. Geology, V. 24, No. 2, p. 99-102.

Miall, A. D., and Tyler, N., eds., 1991. The three-dimensioanl facies architecture of terrigenous clastic sediments and its implications for hydrocarbon discovery and recovery. Concepts in Sedimentology and Paleontology, Volume 3, Society for Sedimentary Geology (SEPM).

Moorman, B. J., 1990. Assessing the ability of ground penetrating radar to delineate subsurface fluvial lithofacies. MS Thesis, University of Calgary, Calgary, Alberta, Canada. 124 p.

Nio, S. D., and Siegenthaler, J. C., 1978. A lower Eocene estuarine-shelf complex in the Isabena Valley. State University Utrecht, Sedimentology Group, Report No. 18, p. 1-44. Diagram referenced in: Walker, R. G., ed., 1984. Facies models, Second Edition. Geological Association of Canada, Toronto, Ontario.

Olhoeft, G. R., 1984. Applications and limitations of ground penetrating radar. 54th annual international meeting and exposition of the Society of Exploration Geophysicists, December 2-6, Atlanta, GA, Expanded Abstracts with Bibliographies, p. 147-148.

Olhoeft, G. R., 1990. Tutorial: high frequency electrical properties. In: Lucius, J. E., *et al.*, eds., *Third international conference on ground penetrating radar*, USGS Open File Report, U. S. Geological Survey, Reston, VA, United States, p. 48.

Plint, A. G., and others, 1986. Cardium Formation 6: stratigraphic framework of the Cardium subsurface. Bulletin of Canadian Petroleum Geology, V. 34, p. 213-225.

Pozzobon, J. G., and Walker, R. G., 1990. Viking Formation (Albian) at Eureka, Saskatchewan: a transgressed and degraded shelf sand ridge. The American Association of Petroleum Geologists Bulletin, V. 74, No. 8, p. 1212-1227.

Rea, J., and Knight, R., 1998. Geostatistical analysis of ground penetrating radar data: a means of describing spatial variation in the subsurface. Water Resources Research, V. 34, No. 3, p. 329-339.

Reineck, H. E., 1963. Sedimentgefuge im Bereich der sudlichen Nordsee. Abhandl. Seneckengerg. Naturforsch. Ges., 505: 1-138.

Reineck, H. E., and Singh, I. B., 1972. Genesis of laminated sand and graded rhythmites in storm sand layers of shelf mud. Sedimentology, V. 18, p. 123-128.

Reinson, G. E., 1984. Barrier-island and associated strand-plain systems. In: Walker, R. G., ed. Facies models, Second Edition. Geological Association of Canada, Toronto, Ontario.

Reitz, J. R., and others, 1993. Foundations of electromagnetic theory. Addison-Wesley Publishing Company, Reading, MA, 630 p.

Reynolds, M. W., 1976. Influence of recurrent Laramide structural growth on sedimentation and petroleum accumulation, Lost Soldier area, Wyoming. American Association of Petroleum Geologists Bulletin, V. 60, p. 12-33.

Rossetti, D. de F., 1997. Internal architecture of mixed tide- and storm-influenced deposits: an example from the Alcantara Formation, northern Brazil. Sedimentary Geology, V. 114, p. 163-188.

Ryer, T. A., 1977. Patterns of Cretaceous shallow marine sedimentation, Coalville and Rockport areas, Utah. Geological Society of America Bulletin, V. 88, p. 177-188.

Sen, P. N., 1980. The dielectric and conductivity response of sedimentary rocks. Society of Petroleum Engineers of AIME, Special Paper No. 9379, 11 p.

Sen, P. N., 1984. Grain shape effects on dielectric and electrical properties of rocks. Geophysics, V. 49, No. 5, p. 586-587.

Sheriff, R. E., and Geldhart, L. P., 1982. Exploration seismology Volume 1: history, theory and data acquisition. Cambridge University Press, New York, New York, 253 p.

Smith, D.G., and Jol, H.M., 1992(a). Ground penetrating radar investigation of a Lake Bonneville delta, Provo level, Bringham City, Utah. Geology, V. 20, p. 1083-1086.

Smith, D.G., and Jol, H.M., 1992(b). GPR results used to infer depositional processes of coastal spits in large lakes. In: Fourth international conference on ground penetrating radar, June 8-13, 1992, Rovaniemi, Finland. Geological Survey of Finland, Special Paper 16, Hanninen, P., and Autio, S., eds., p. 169-177.

Smith, D.G., and Jol, H.M., 1993. Ground penetrating radar: antennae frequencies and maximum probable depths of penetration in Quaternary sediments. Journal of Applied Geophysics, V. 33, p. 93-100.

Smith, D.G., and Jol, H.M., 1995. Wasatch Fault (Utah), detected and displacement characterized by ground penetrating radar. Environmental and Engineering Geoscience, V. I, No. 4, p. 489-496.

Smith, D.G., and Jol, H.M., 1997. Radar structure of a Gilbert-type delta, Peyto Lake, Banff National Park, Canada. Sedimentary Geology, V. 113, p. 195-209.

Spearing, D. R., 1976. Upper Cretaceous Shannon Sandstone: an offshore, shallow-marine sand body. Wyoming Geological Association 28th Annual Field Conference, 1976 Guidebook, p. 65-72.

Stephens, M., 1991. Architectural element analysis within the Kayenta Formation (Lower Jurassic) using ground-probing radar and sedimentological profiling, southwestern Colorado. MS Thesis, University of Toronto. _p.

Swift, D. J. P., and Rice, D. D., 1984. Sand bodies on muddy shelves: a model for sedimentation in the Western Interior Seaway, North America. In: Tillman, R. W., and Siemers, C. T., eds., Siliciclastic shelf sediments. Society of Economic paleontologists and Mineralogists, Special Publication No. 34, p. 43-62.

Telford, W. M., and others, 1990. Applied geophysics: second edition. Cambridge University Press, New York, New York, 770 p.

Tillman, R. W., and Martinsen, R. S., 1984. The Shannon shelf-ridge sandstone complex, Salt Creek Anticline area, Powder River Basin, Wyoming. In: Siliciclastic shelf sediments, Society of Economic Paleontologists and Mineralogists, Special Publication No. 34, p. 85-142.

Topp, G. C., and others, 1980. Electromagnetic determination of soil water content: measurements in coaxial transmission lines. Water Resources Research, V. 16, No. 3, p. 574-582.

Ulriksen, P. F., 1982. Application of impulse radar to civil engineering. Ph.D. Dissertation, Lund University of Technology, Lund, Sweden, 179 p.

Vail, P. R., and others, 1977. Seismic stratigraphy and global changes of sea level, part 3: Relative changes in sea level from coastal onlap. In: Payton, C. E., ed., Seismic stratigraphy- applications to hydrocarbon exploration. American Association of Petroleum Geologists, Memoir 26, p. 63-81.

Walker, R. G., ed., 1979. Facies models. Geological Association of Canada, Toronto, Ontario. 211 p.

Walker, R. G., ed., 1984. Facies models, second edition. Geological Association of Canada, Toronto, Ontario. 317 p.

Walker, R. G., and James, N. P., eds., 1992. Facies models: response to sea level change. Geological Association of Canada, Toronto, Ontario. 409 p.

Walker, R. G., and Plint, A. G., 1992. Wave- and storm-dominated shallow marine systems. In: Walker, R. G., and James, N. P., eds., 1992. Facies models, response to sea level change. Geological Association of Canada, Toronto, Ontario.

Wright, M. E., and Walker, R. G., 1981. Cardium Formation (U. Cretaceous) at Seebe, Alberta- storm-transported sandstones and conglomerates in shallow marine depositional environments below fair-weather wave base. Canadian Journal of Earth Science, V. 18, p. 795-809.

Wyatt, D. E., and Temples, T. J., 1996. Ground-penetrating radar detection of small-scale channels, joints and faults in the unconsolidated sediments of the Atlantic coastal plane. Environmental Geology, V. 27, p. 219-225.

APPENDIX I

Plots of the changes in the compositional attributes as determined by point counting with the associated calculated synthetic reflection coefficients

- Delta values represent the change in the number of grains counted between the specimens used to generate the synthetic reflection coefficients
- In each plot, the horizontal axis is the number of each of the 14 reflection coefficients
- In each plot, the vertical axis is the value (unitless) for both the variables described at the right

100X Saturated Refl. Coeff	Delta Qm
-39.94	-26
-1.38	-18
-26.06	-14
-0.64	-10
-3.14	-10
9.34	-7
-31.56	-7
30.84	-6
-9.54	2
-2.64	5
-0.54	8
10.79	10
23.47	11
38.60	59

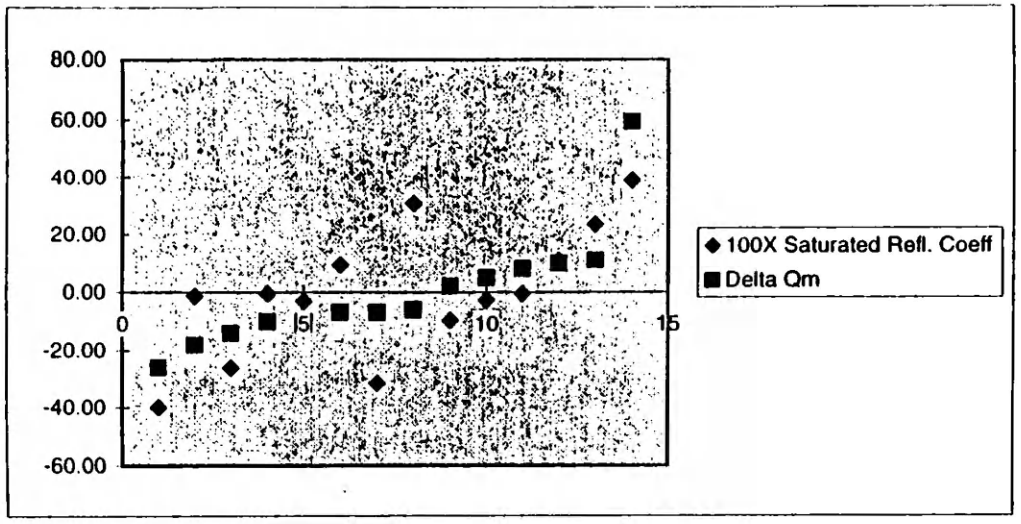

100X Unsaturated Refl. Coeff	Delta Qm
1.32	-26
4.06	-18
-8.47	-14
3.95	-10
-3.60	-10
1.21	-7
-11.85	-7
17.84	-6
5.66	2
1.14	5
6.33	8
-10.48	10
0.48	11
-0.64	59

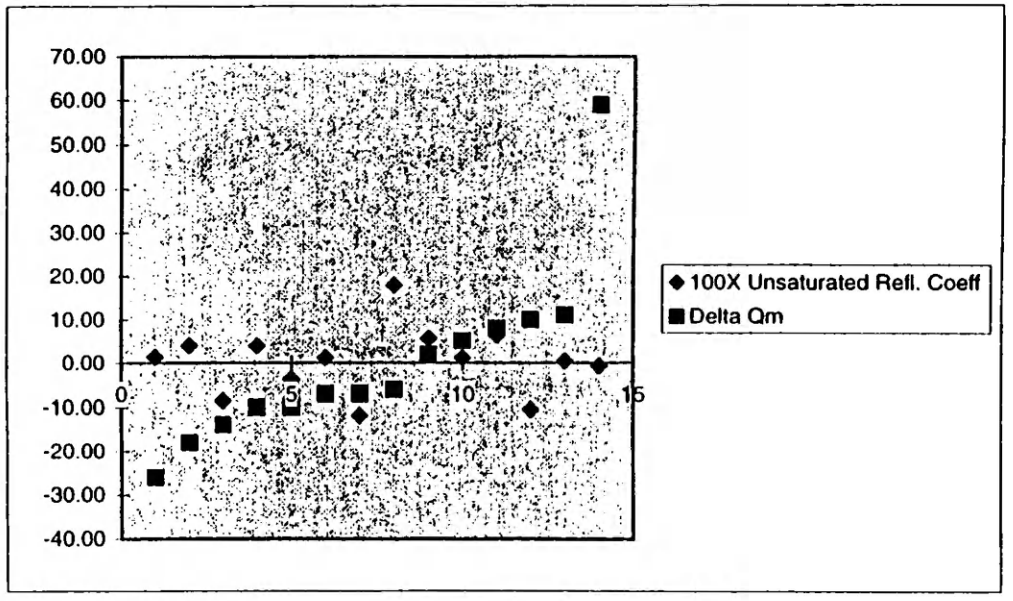

100X Saturated Refl. Coeff	Delta Cht.
38.60	-44
-0.54	-29
10.79	-27
23.47	-18
-31.56	-14
-9.54	-7
-2.64	-6
30.84	7
9.34	11
-3.14	21
-0.64	26
-1.38	26
-39.94	37
-26.06	44

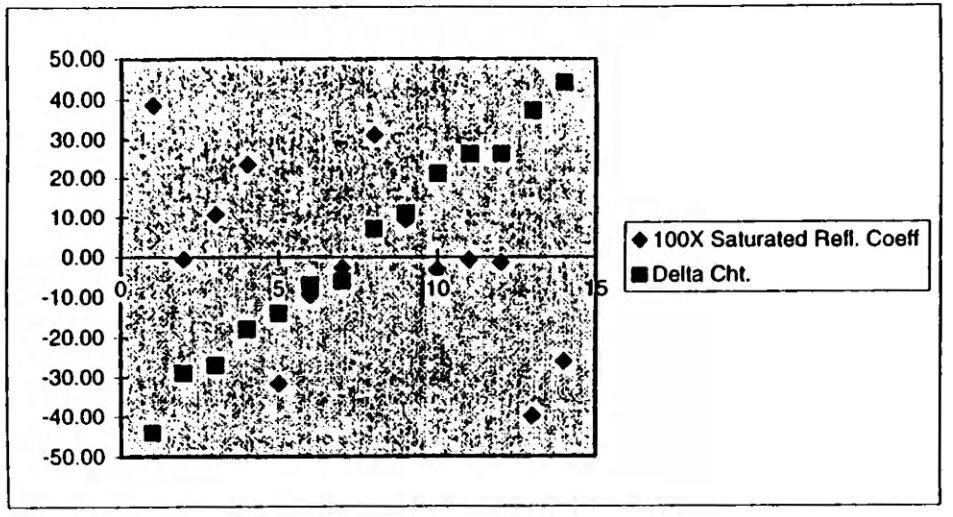

100X Unsaturated Refl. Coeff	Delta Cht.
-0.64	-44
6.33	-29
-10.48	-27
0.48	-18
-11.85	-14
5.66	-7
1.14	-6
17.84	7
1.21	11
-3.60	21
3.95	26
4.06	26
1.32	37
-8.47	44

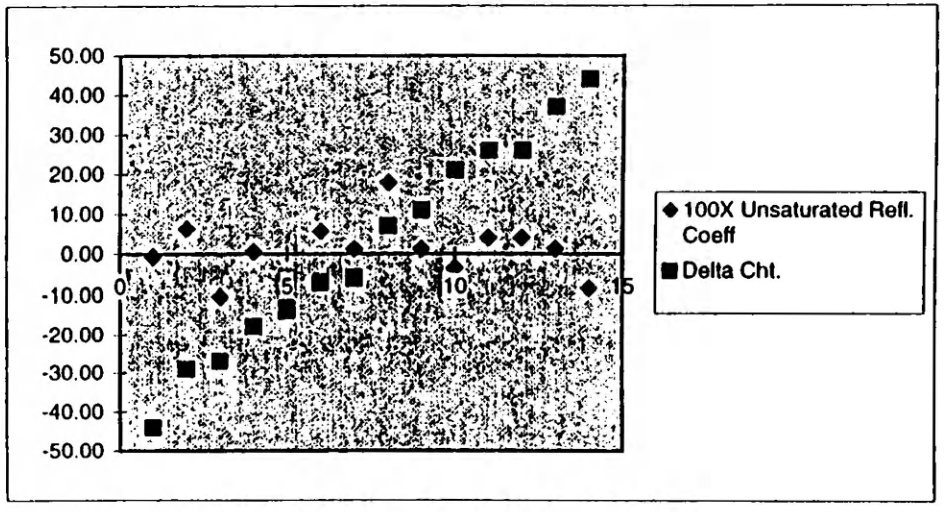

100X Saturated Refl. Coeff	Delta Porosity (%)
-1.38	-6.99
-31.56	-5.11
-9.54	-5.03
9.34	-2.72
-0.64	-1.16
23.47	-1.05
-39.94	-0.15
38.60	0.93
10.79	1.36
-2.64	1.98
-3.14	2.2
-26.06	3.34
-0.54	4.79
30.84	6.87

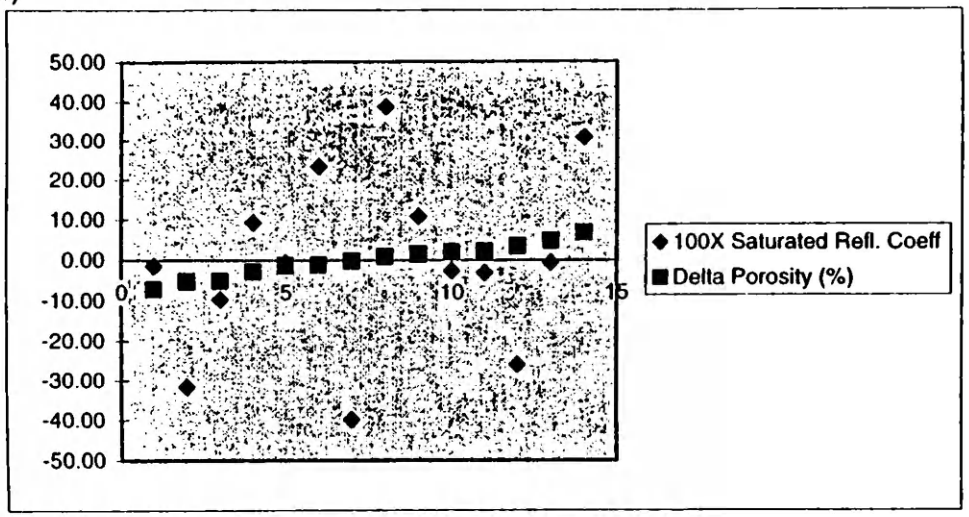

100X Unsaturated Refl. Coe	Delta Porosity(%)
4.06	-6.99
-11.85	-5.11
5.66	-5.03
1.21	-2.72
3.95	-1.16
0.48	-1.05
1.32	-0.15
-0.64	0.93
-10.48	1.36
1.14	1.98
-3.60	2.2
-8.47	3.34
6.33	4.79
17.84	6.87

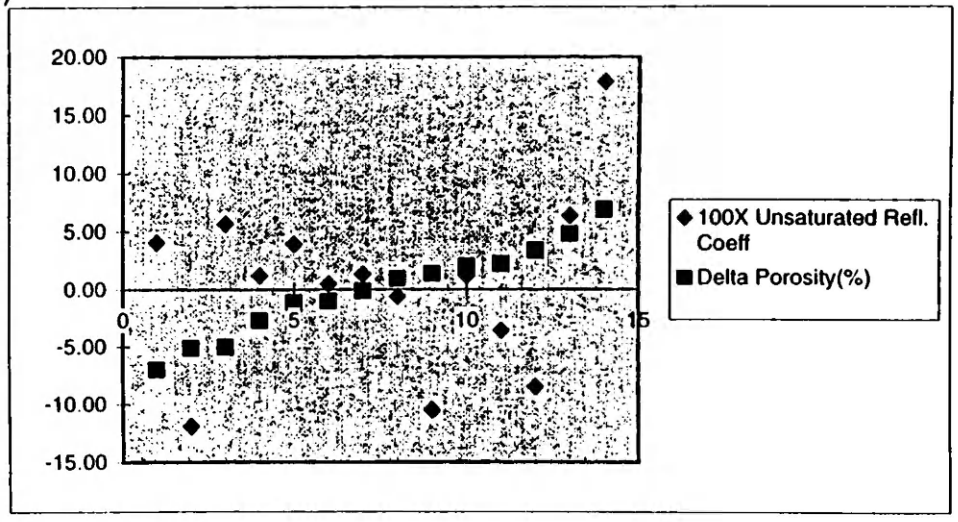

100X Saturated Refl. Coeff	Delta K
38.60	-25
-0.64	-20
-2.64	-17
-1.38	-14
-26.06	-11
23.47	-5
9.34	-3
-3.14	-1
-39.94	1
10.79	6
-0.54	8
30.84	17
-9.54	23
-31.56	27

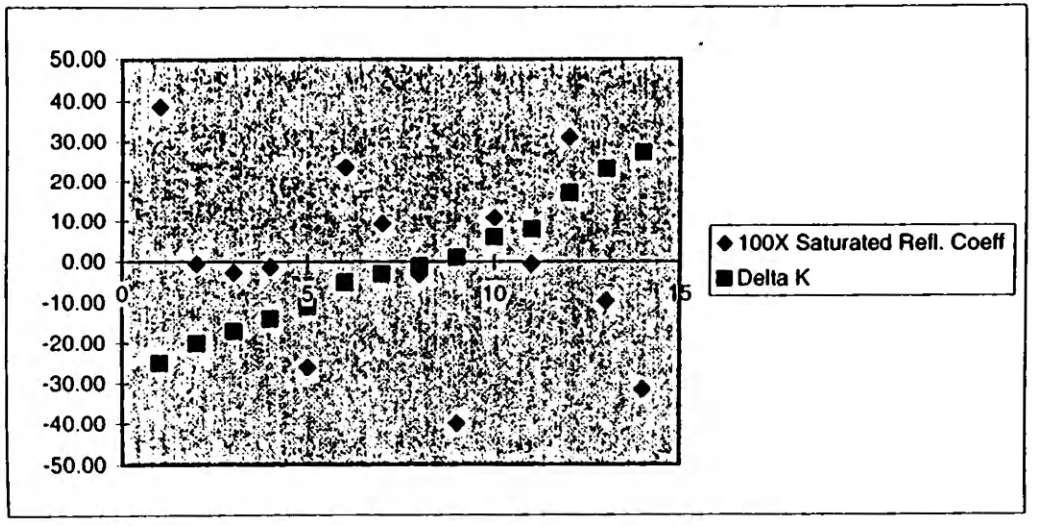

100X Unsaturated Refl. Co	Delta K
-0.64	-25
3.95	-20
1.14	-17
4.06	-14
-8.47	-11
0.48	-5
1.21	-3
-3.60	-1
1.32	1
-10.48	6
6.33	8
17.84	17
5.66	23
-11.85	27

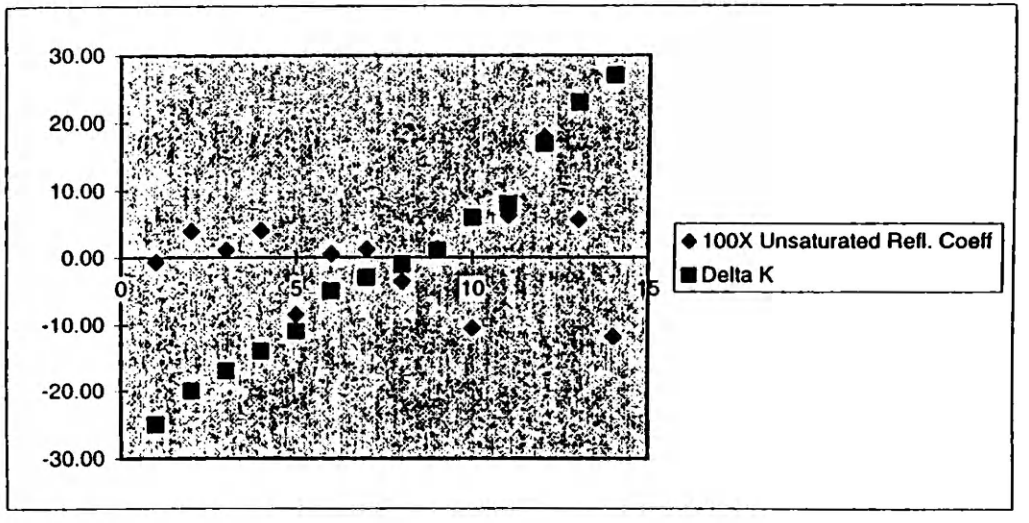

100X Saturated Refl. Coeff	Delta P
-3.14	-4
-26.06	-2
30.84	-1
-31.56	-1
-0.64	-1
-39.94	-1
38.60	0
-2.64	1
23.47	1
9.34	2
-9.54	2
-1.38	2
10.79	4
-0.54	6

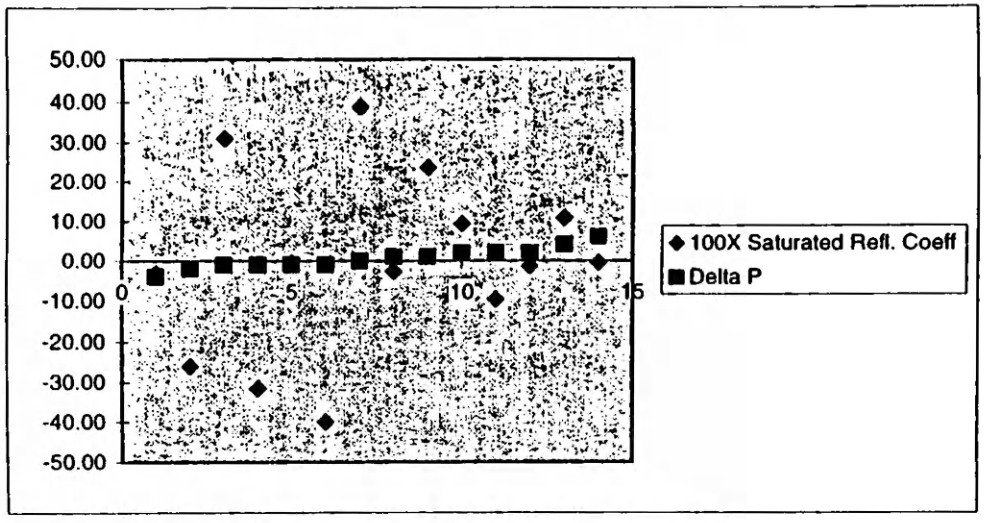

100X Unsaturated Refl. Coeff	Delta P
-3.60	-4
-8.47	-2
17.84	-1
-11.85	-1
3.95	-1
1.32	-1
-0.64	0
1.14	1
0.48	1
1.21	2
5.66	2
4.06	2
-10.48	4
6.33	6

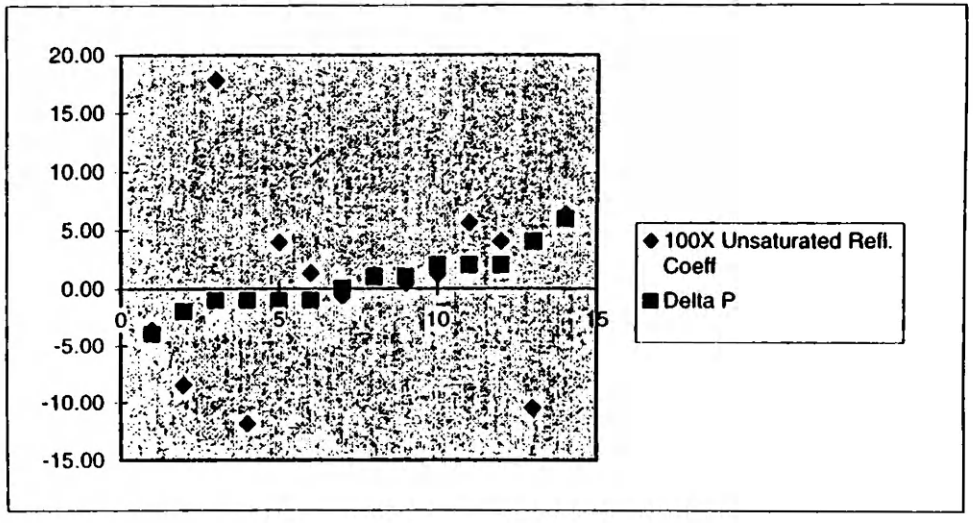

100X Saturated Refl. Coeff	Delta Lv
-1.38	-12
30.84	-9
-9.54	-8
38.60	0
-0.54	0
-31.56	1
23.47	1
-2.64	2
-0.64	2
10.79	2
9.34	3
-26.06	3
-39.94	3
-3.14	11

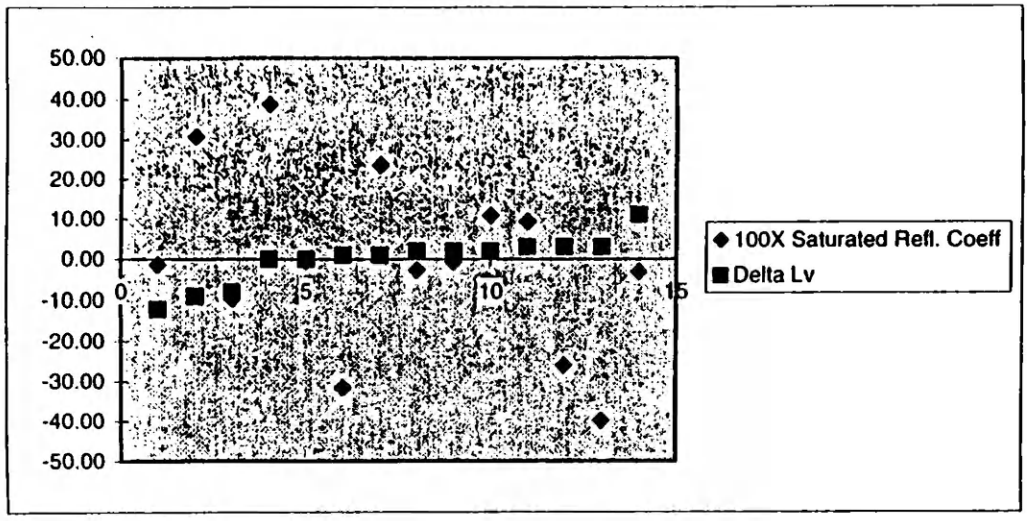

100X Unsaturated Refl. Coef	Delta Lv
4.06	-12
17.84	-9
5.66	-8
-0.64	0
6.33	0
-11.85	1
0.48	1
1.14	2
3.95	2
-10.48	2
1.21	3
-8.47	3
1.32	3
-3.60	11

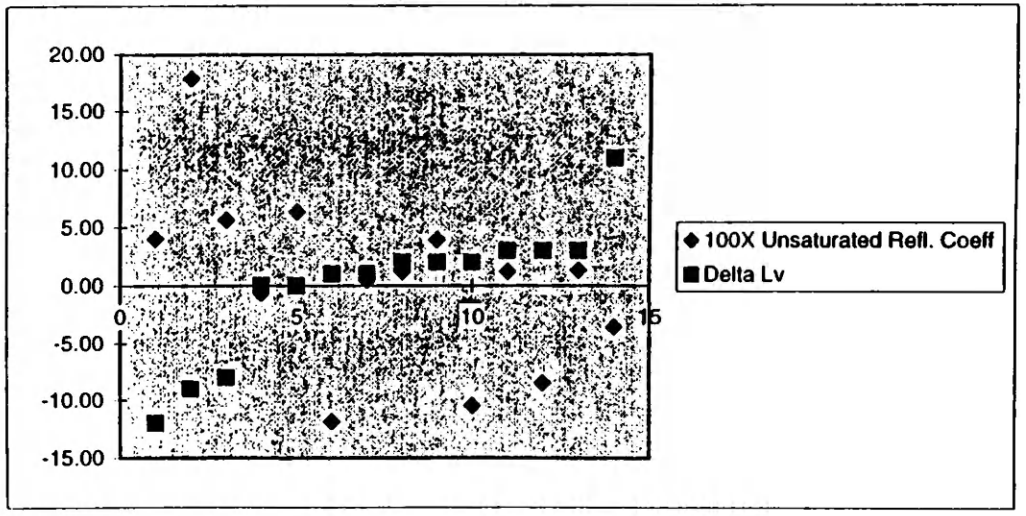

100X Saturated Refl. Coeff	Delta Cement
-9.54	-23
-3.14	-20
9.34	-11
-39.94	-8
23.47	-3
-0.64	-2
-26.06	-2
-1.38	-1
30.84	2
10.79	2
-31.56	5
38.60	12
-2.64	16
-0.54	17

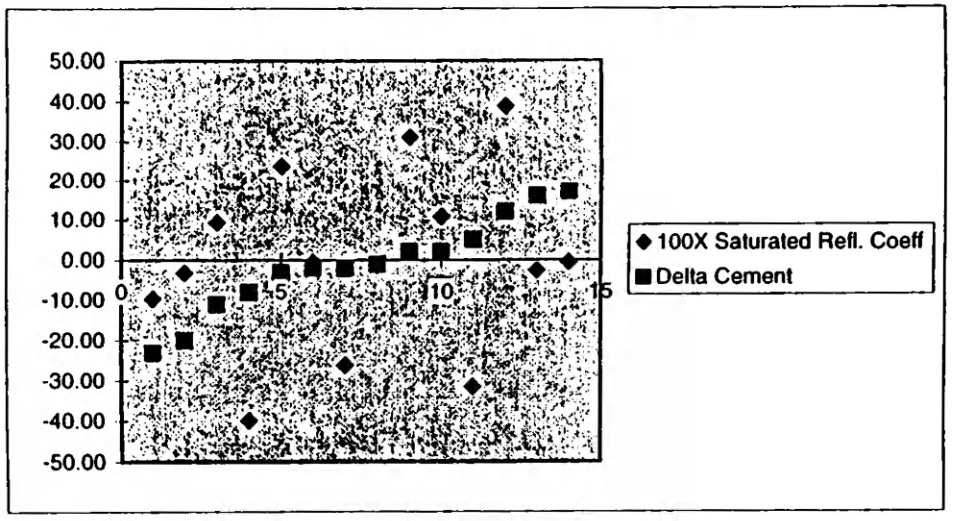

100X Unsaturated Refl. Coeff	Delta Cement
5.66	-23
-3.60	-20
1.21	-11
1.32	-8
0.48	-3
3.95	-2
-8.47	-2
4.06	-1
17.84	2
-10.48	2
-11.85	5
-0.64	12
1.14	16
6.33	17

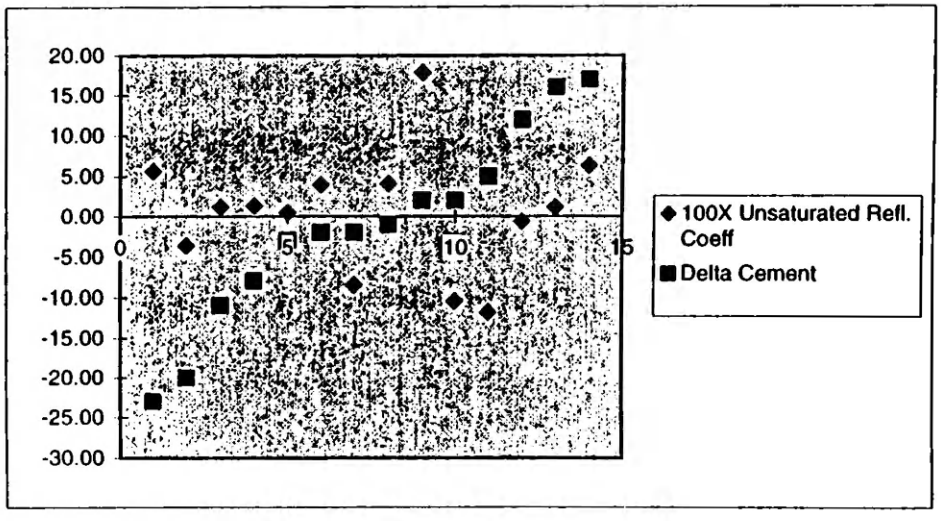

100X Saturated Refl. Coeff	Delta Cmt+mat
-9.54	-22
-3.14	-19
30.84	-13
-26.06	-11
-39.94	-10
9.34	-4
10.79	-4
-0.64	-3
-31.56	-1
23.47	11
-1.38	12
-0.54	14
38.60	15
-2.64	17

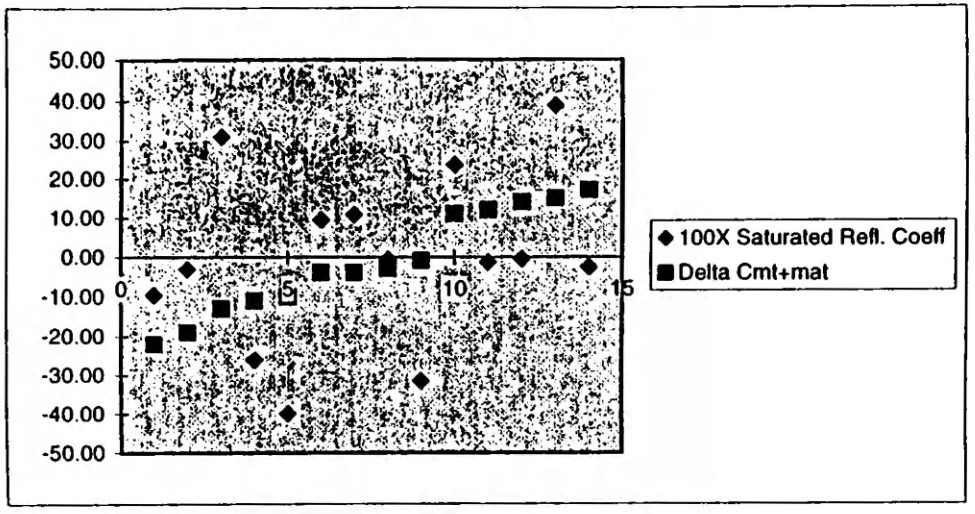

100X Unsaturated Refl. Coe	Delta Cmt+mat
5.66	-22
-3.60	-19
17.84	-13
-8.47	-11
1.32	-10
1.21	-4
-10.48	-4
3.95	-3
-11.85	-1
0.48	11
4.06	12
6.33	14
-0.64	15
1.14	17

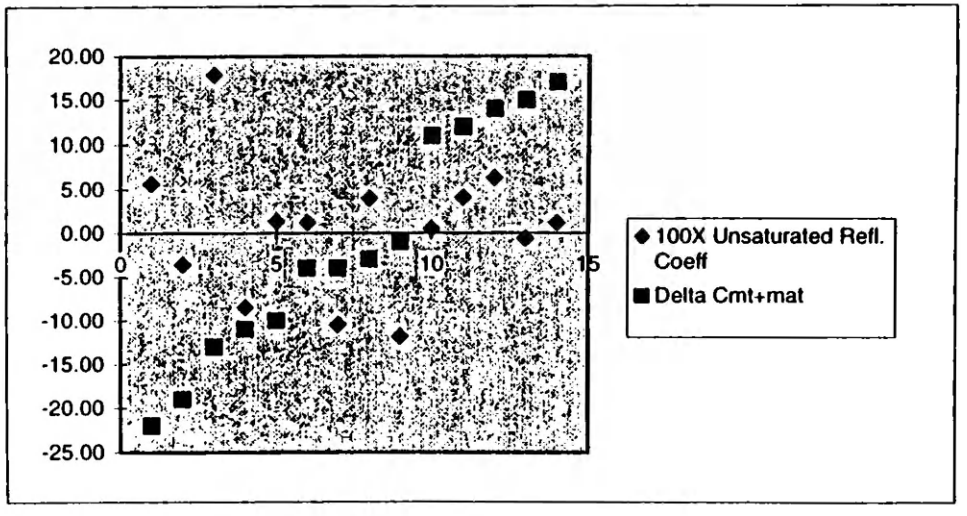

100X Saturated Refl. Coeff	Delta Cmt+matrix+porosity
-9.54	-27.03
-3.14	-16.80
-39.94	-10.15
-26.06	-7.66
9.34	-6.72
30.84	-6.13
-31.56	-6.11
-0.64	-4.16
10.79	-2.64
-1.38	5.01
23.47	9.95
38.60	15.93
-0.54	18.79
-2.64	18.98

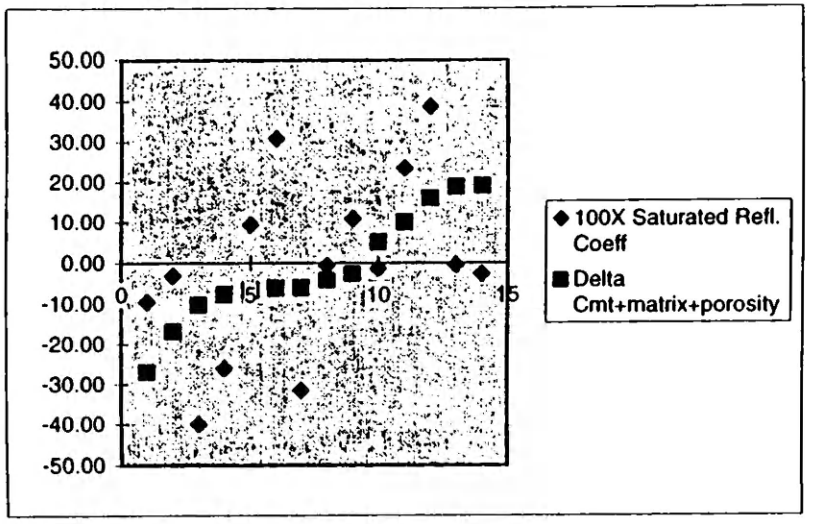

100X Unsaturated Refl. Coeff	Delta Cmt+matrix+porosity
5.66	-27.03
-3.60	-16.80
1.32	-10.15
-8.47	-7.66
1.21	-6.72
17.84	-6.13
-11.85	-6.11
3.95	-4.16
-10.48	-2.64
4.06	5.01
0.48	9.95
-0.64	15.93
6.33	18.79
1.14	18.98

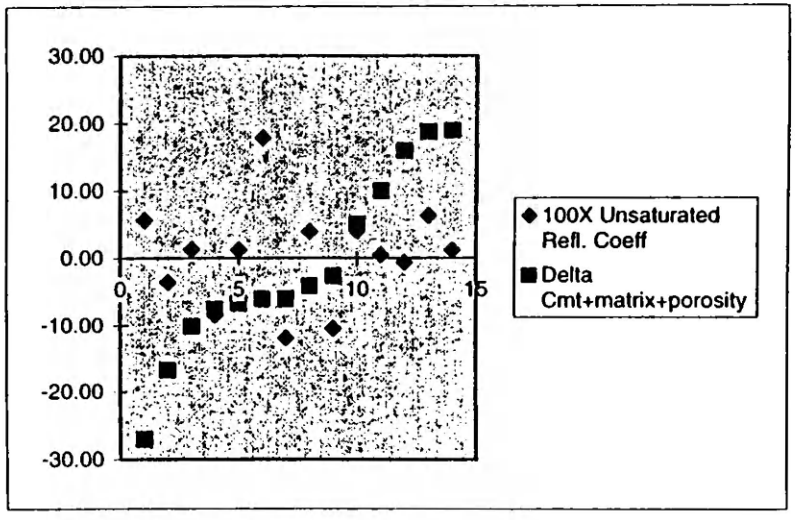

APPENDIX II

Plots of the electrical measurements between 20 and 1000 MHz for the 15 samples from Section G

- Crosses and squares correspond to the two measurements on the unsaturated specimens
- Hour-glass and asterisk correspond to the two measurements on the saturated specimens
- Raw data for 50 MHz (survey frequency) presented in Table 33

G1

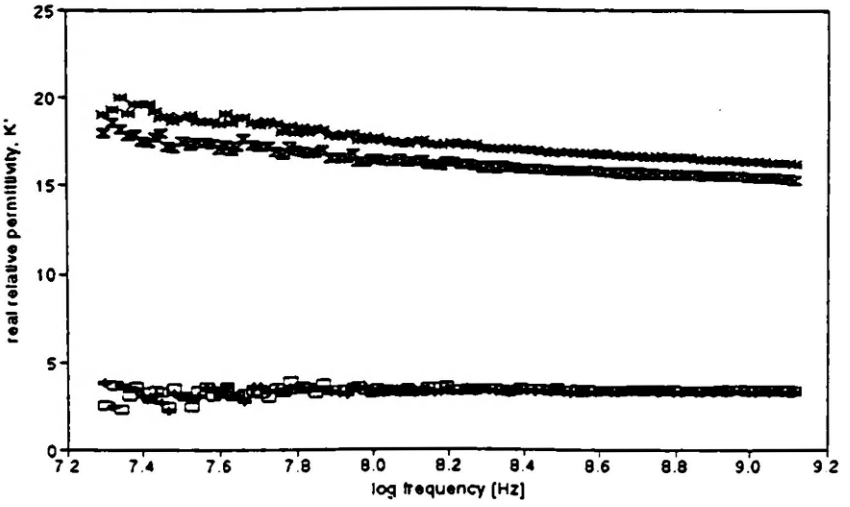
real relative permittivity, K'
25
20
15
10
5
0
7.2
7.4
7.6
7.8
8.0
8.2
8.4
8.6
8.8
9.0
9.2
log frequency [Hz]

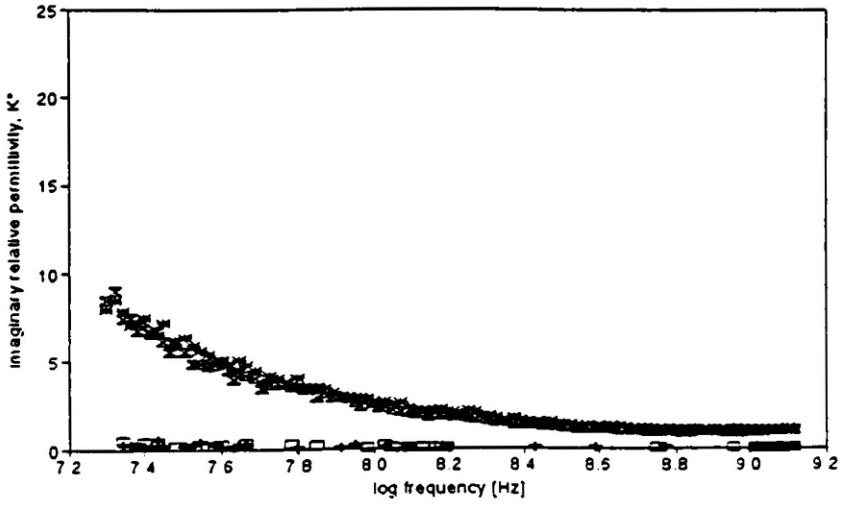
imaginary relative permittivity, K"
25
20
15
10
5
0
7.2
7.4
7.6
7.8
8.0
8.2
8.4
8.5
8.8
9.0
9.2
log frequency [Hz]

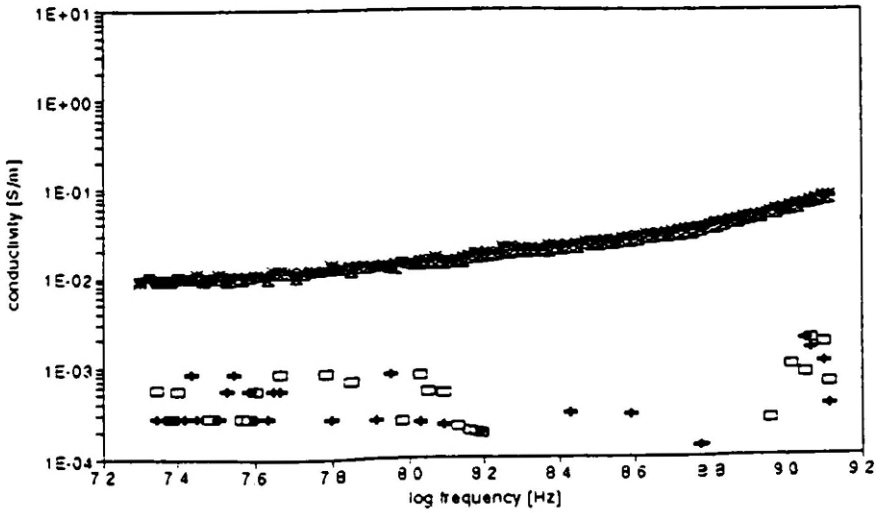
conductivity [S/m]
1E+01
1E+00
1E-01
1E-02
1E-03
1E-04
7.2
7.4
7.6
7.8
8.0
8.2
8.4
8.6
8.8
9.0
9.2
log frequency [Hz]

G2

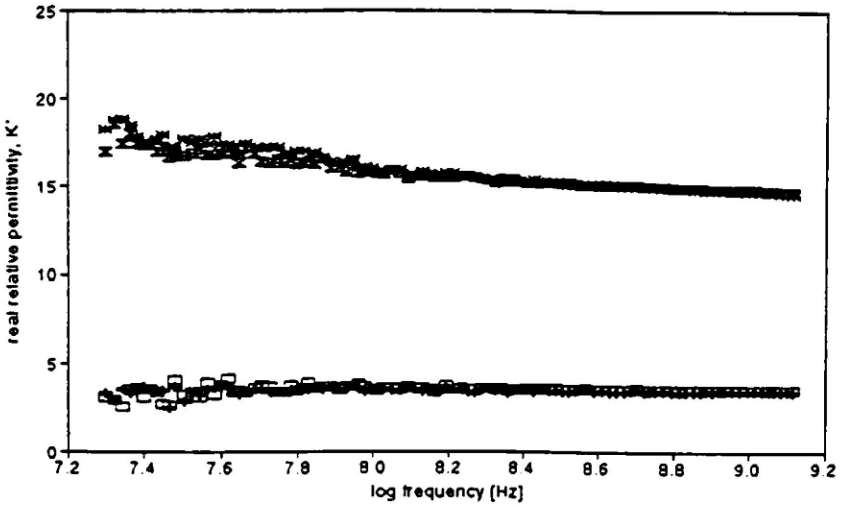
real relative permittivity, K'
25
20
15
10
5
0
7.2
7.4
7.6
7.8
8.0
8.2
8.4
8.6
8.8
9.0
9.2
log frequency [Hz]

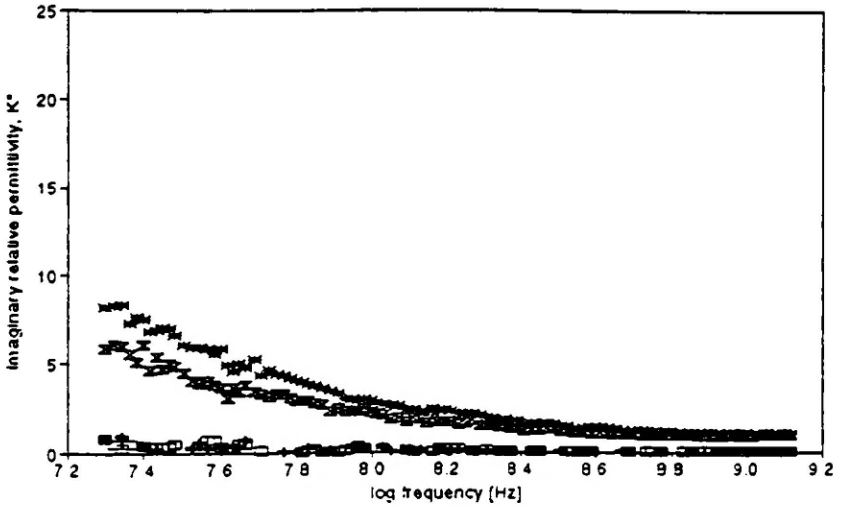
imaginary relative permittivity, K"
25
20
15
10
5
0
7.2
7.4
7.6
7.8
8.0
8.2
8.4
8.6
8.8
9.0
9.2
log frequency [Hz]

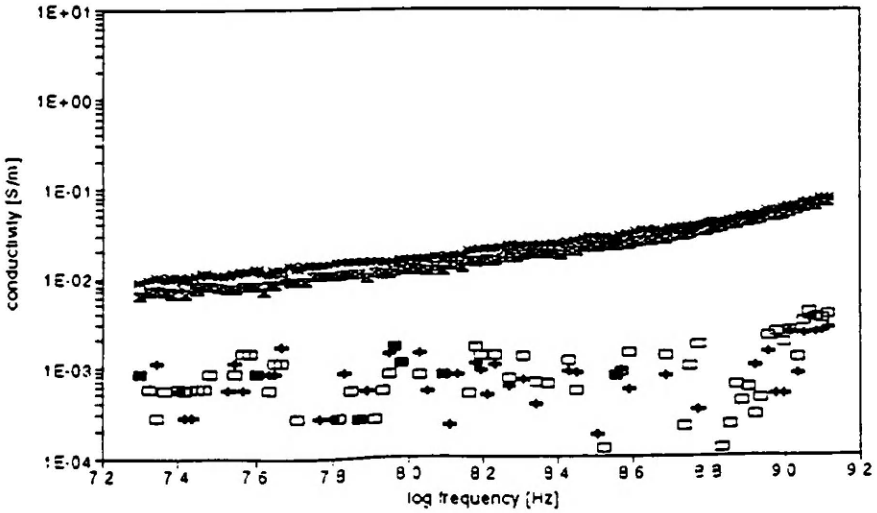
conductivity [S/m]
1E+01
1E+00
1E-01
1E-02
1E-03
1E-04
7.2
7.4
7.6
7.8
8.0
8.2
8.4
8.6
8.8
9.0
9.2
log frequency [Hz]

G3

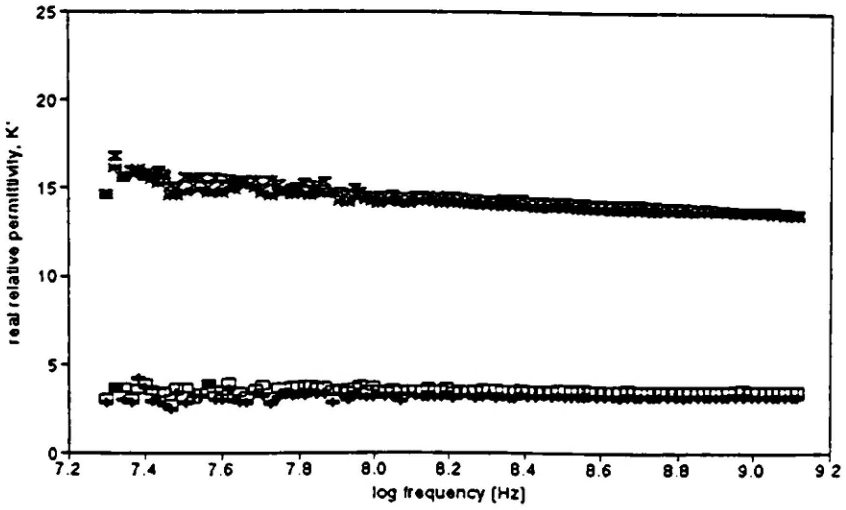
real relative permittivity, K'
25
20
15
10
5
0
7.2
7.4
7.6
7.8
8.0
8.2
8.4
8.6
8.8
9.0
9.2
log frequency [Hz]

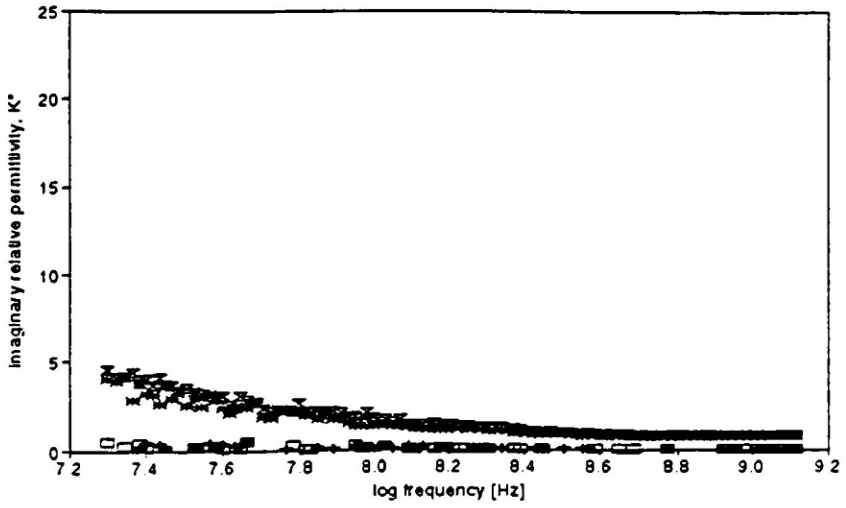
imaginary relative permittivity, K"
25
20
15
10
5
0
7.2
7.4
7.6
7.8
8.0
8.2
8.4
8.6
8.8
9.0
9.2
log frequency [Hz]

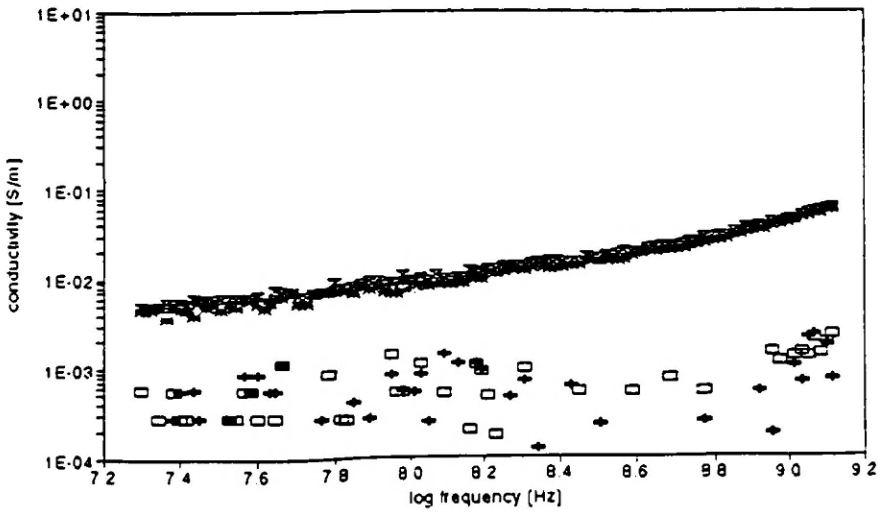
conductivity [S/m]
1E+01
1E+00
1E-01
1E-02
1E-03
1E-04
7.2
7.4
7.6
7.8
8.0
8.2
8.4
8.6
8.8
9.0
9.2
log frequency [Hz]

G4

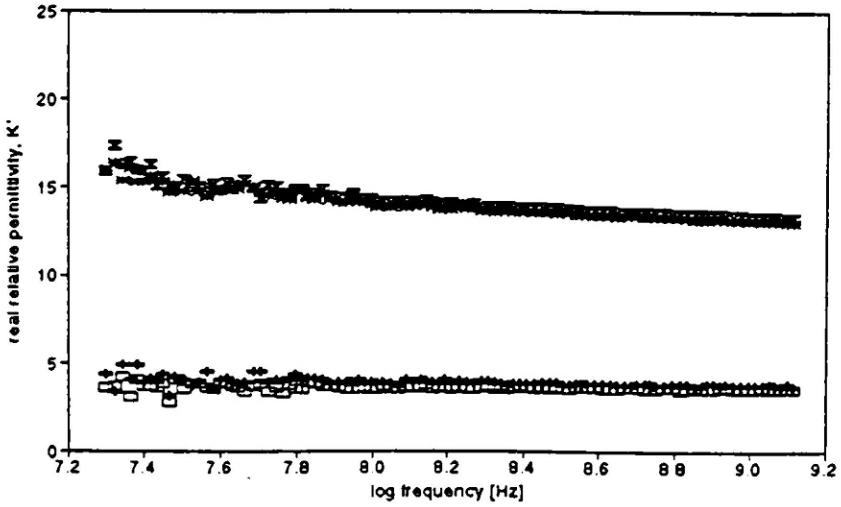
real relative permittivity, K'
25
20
15
10
5
0
7.2
7.4
7.6
7.8
8.0
8.2
8.4
8.6
8.8
9.0
9.2
log frequency [Hz]

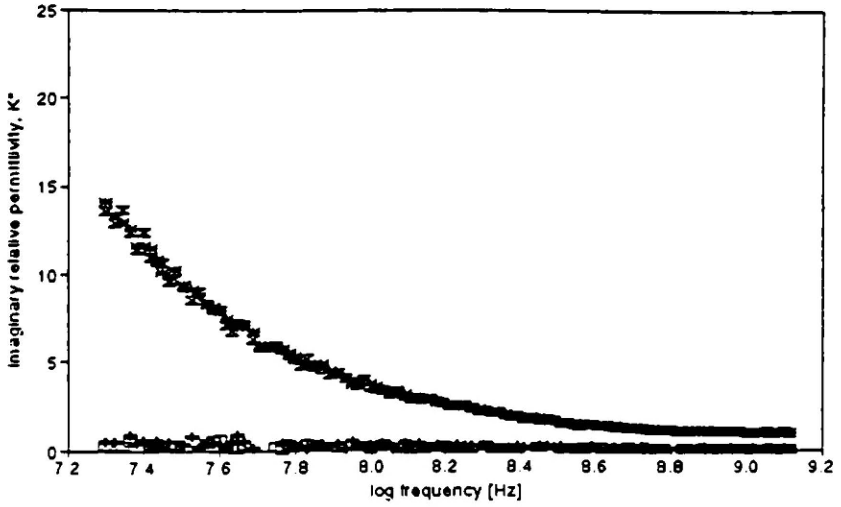
imaginary relative permittivity, K"
25
20
15
10
5
0
7.2
7.4
7.6
7.8
8.0
8.2
8.4
8.6
8.8
9.0
9.2
log frequency [Hz]

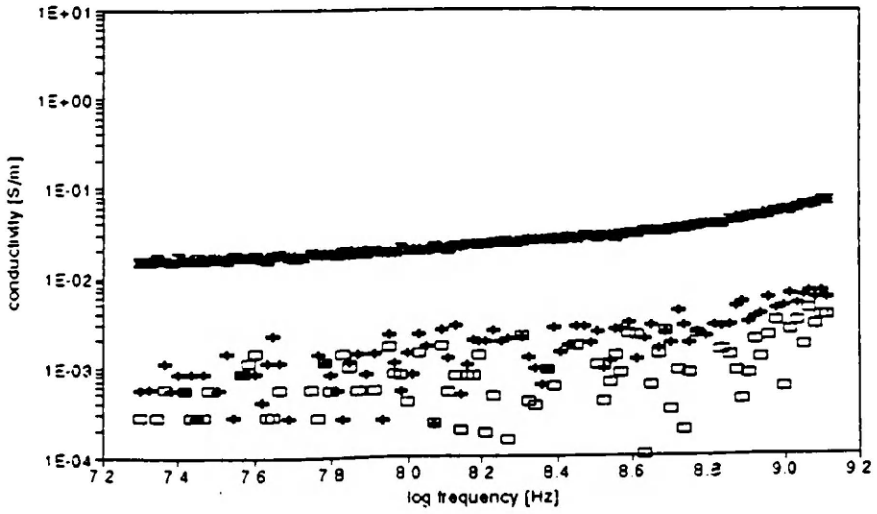
conductivity [S/m]
1E+01
1E+00
1E-01
1E-02
1E-03
1E-04
7.2
7.4
7.6
7.8
8.0
8.2
8.4
8.6
8.8
9.0
9.2
log frequency [Hz]

G5

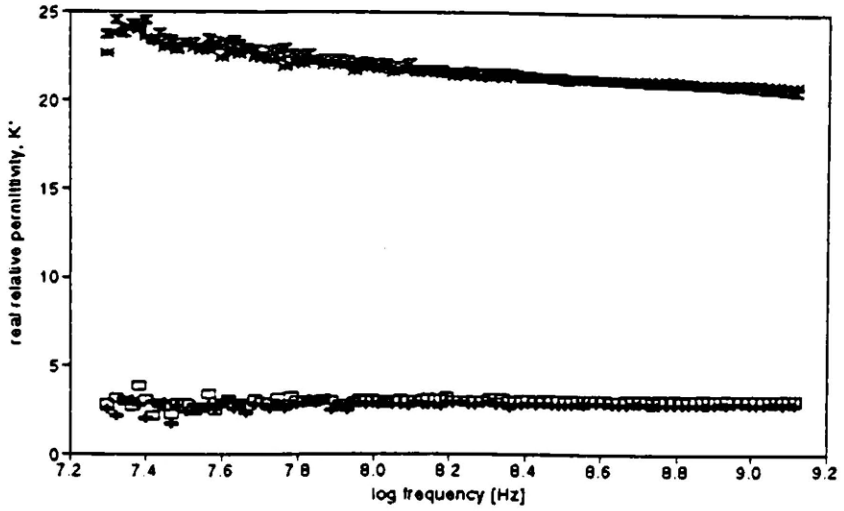
real relative permittivity, K'
25
20
15
10
5
0
7.2
7.4
7.6
7.8
8.0
8.2
8.4
8.6
8.8
9.0
9.2
log frequency [Hz]

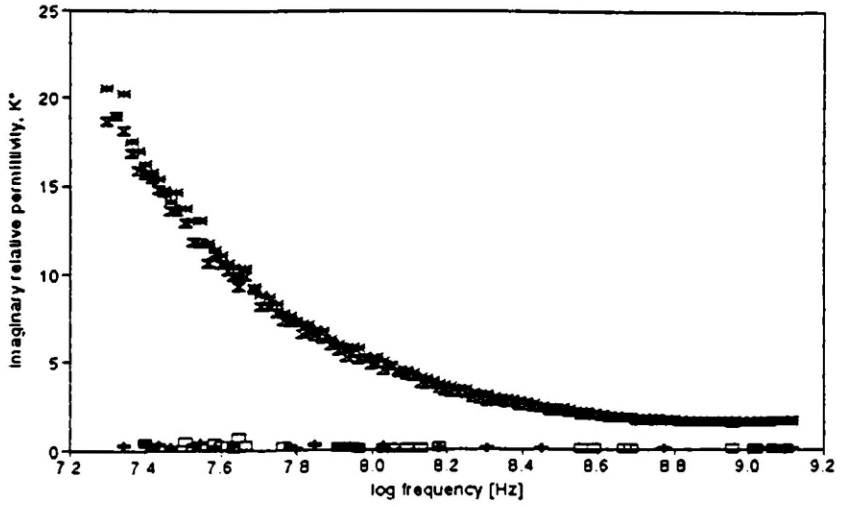
imaginary relative permittivity, K"
25
20
15
10
5
0
7.2
7.4
7.6
7.8
8.0
8.2
8.4
8.6
8.8
9.0
9.2
log frequency [Hz]

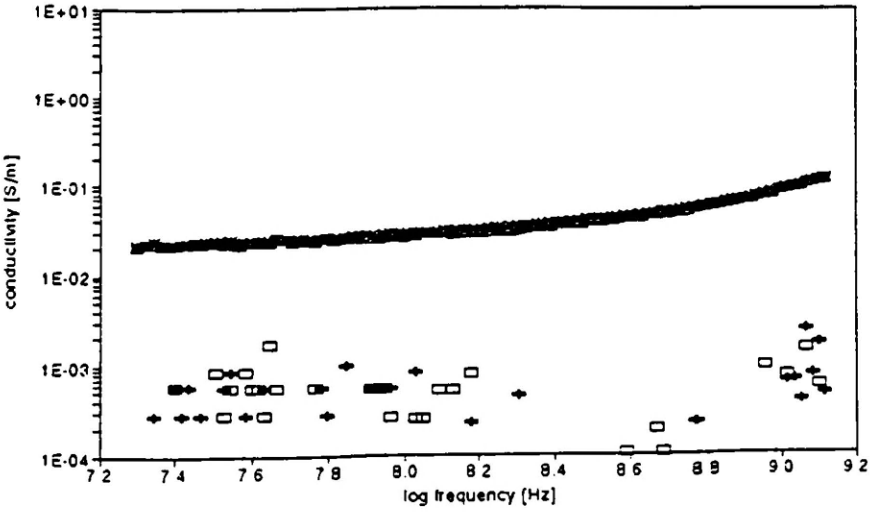
conductivity [S/m]
1E+01
1E+00
1E-01
1E-02
1E-03
1E-04
7.2
7.4
7.6
7.8
8.0
8.2
8.4
8.6
8.8
9.0
9.2
log frequency [Hz]

813A

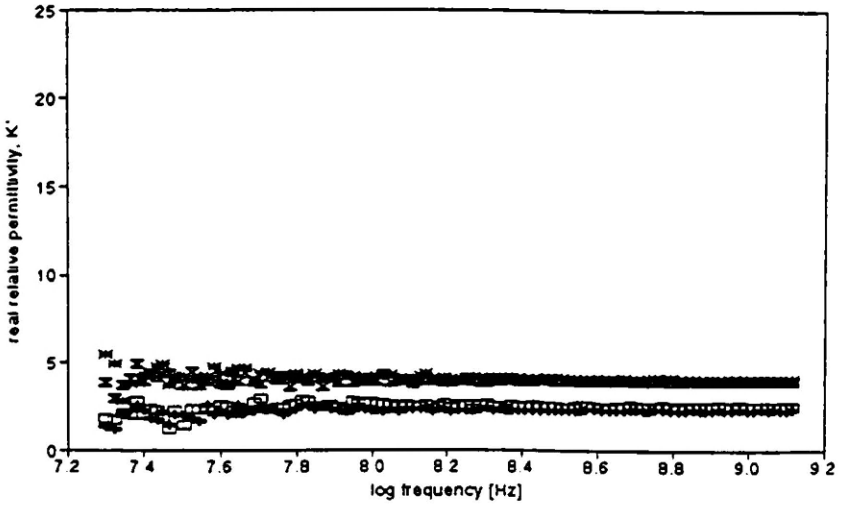
real relative permittivity, K'
25
20
15
10
5
0
7.2
7.4
7.6
7.8
8.0
8.2
8.4
8.6
8.8
9.0
9.2
log frequency [Hz]

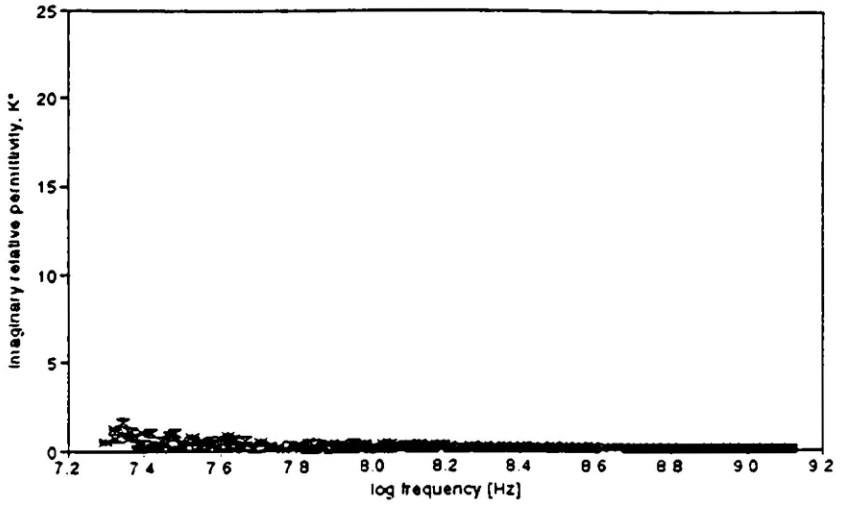
imaginary relative permittivity, K"
25
20
15
10
5
0
7.2
7.4
7.6
7.8
8.0
8.2
8.4
8.6
8.8
9.0
9.2
log frequency [Hz]

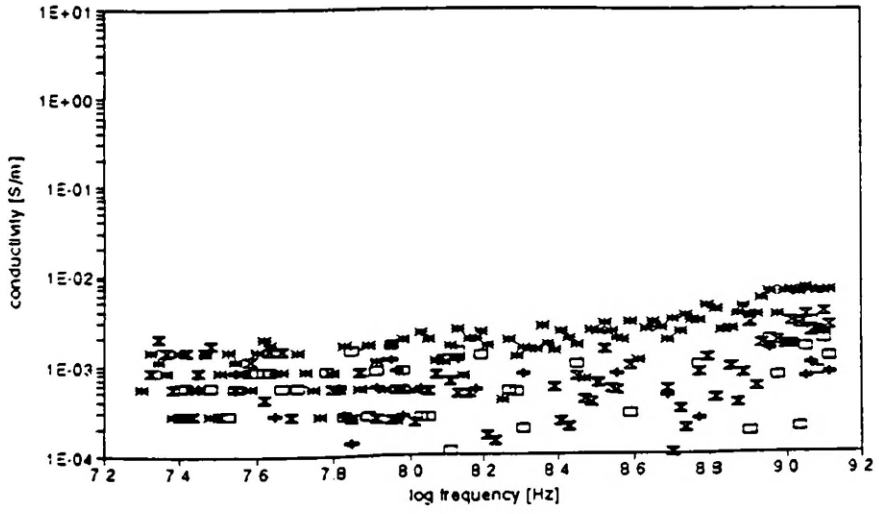
conductivity [S/m]
1E+01
1E+00
1E-01
1E-02
1E-03
1E-04
7.2
7.4
7.6
7.8
8.0
8.2
8.4
8.6
8.8
9.0
9.2
log frequency [Hz]

G6

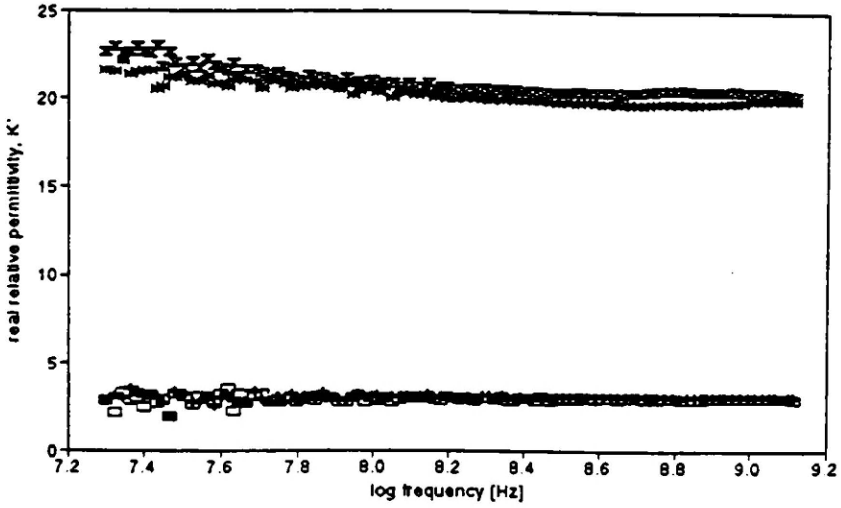
real relative permittivity, K'
25
20
15
10
5
0
7.2
7.4
7.6
7.8
8.0
8.2
8.4
8.6
8.8
9.0
9.2
log frequency [Hz]

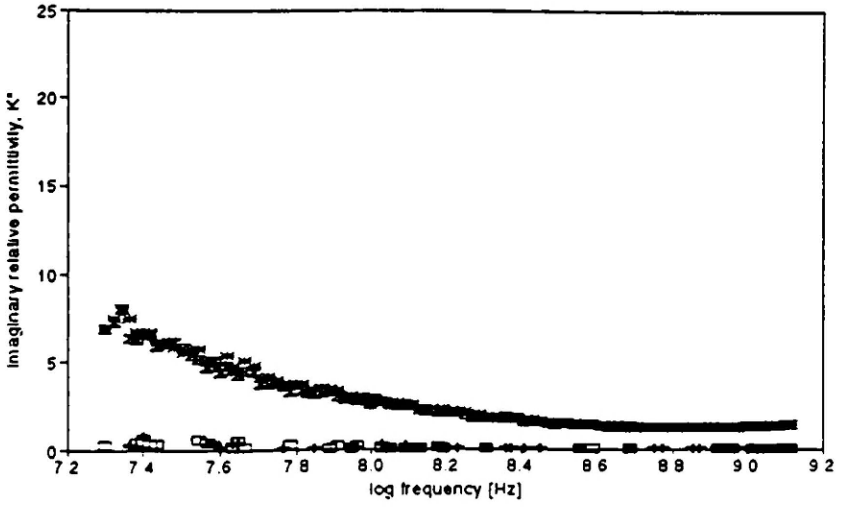
imaginary relative permittivity, K"
25
20
15
10
5
0
7.2
7.4
7.6
7.8
8.0
8.2
8.4
8.6
8.8
9.0
9.2
log frequency [Hz]

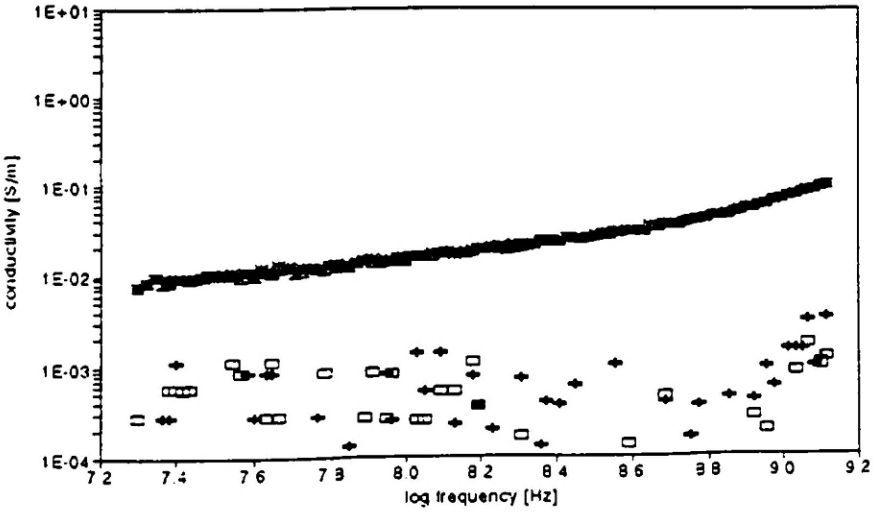
conductivity [S/m]
1E+01
1E+00
1E-01
1E-02
1E-03
1E-04
7.2
7.4
7.6
7.8
8.0
8.2
8.4
8.6
8.8
9.0
9.2
log frequency [Hz]

G7

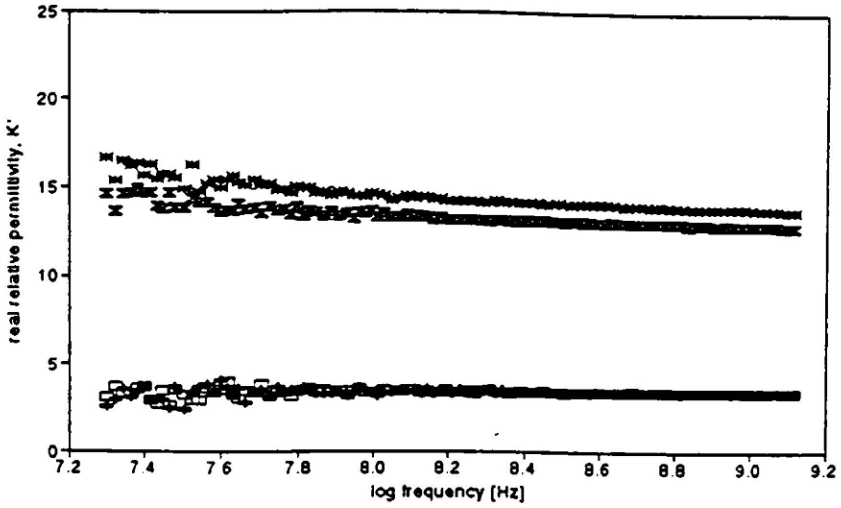
real relative permittivity, K'
25
20
15
10
5
0
7.2
7.4
7.6
7.8
8.0
8.2
8.4
8.6
8.8
9.0
9.2
log frequency [Hz]

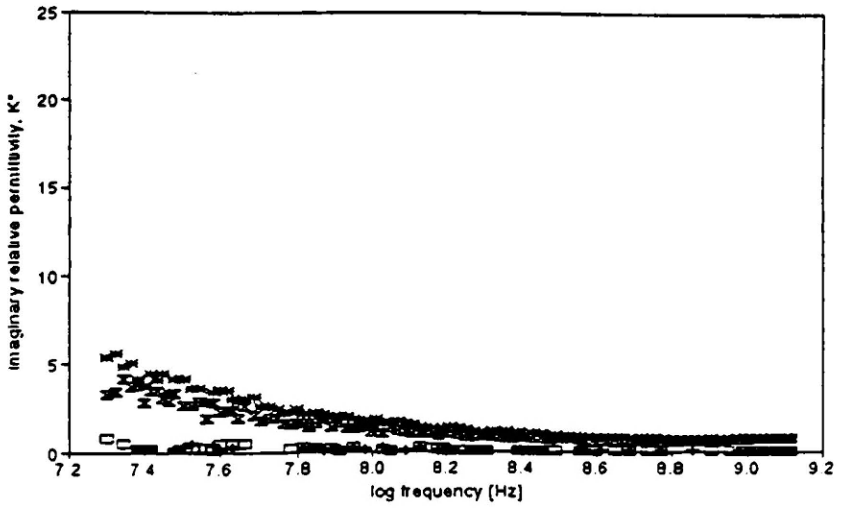
imaginary relative permittivity, K"
25
20
15
10
5
0
7.2
7.4
7.6
7.8
8.0
8.2
8.4
8.6
8.8
9.0
9.2
log frequency [Hz]

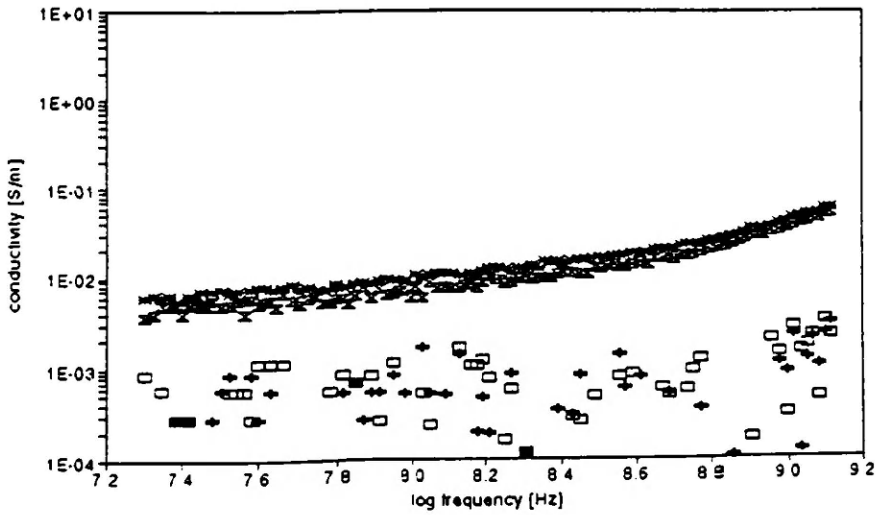
conductivity [S/m]
1E+01
1E+00
1E-01
1E-02
1E-03
1E-04
7.2
7.4
7.6
7.8
8.0
8.2
8.4
8.6
8.8
9.0
9.2
log frequency [Hz]

G8

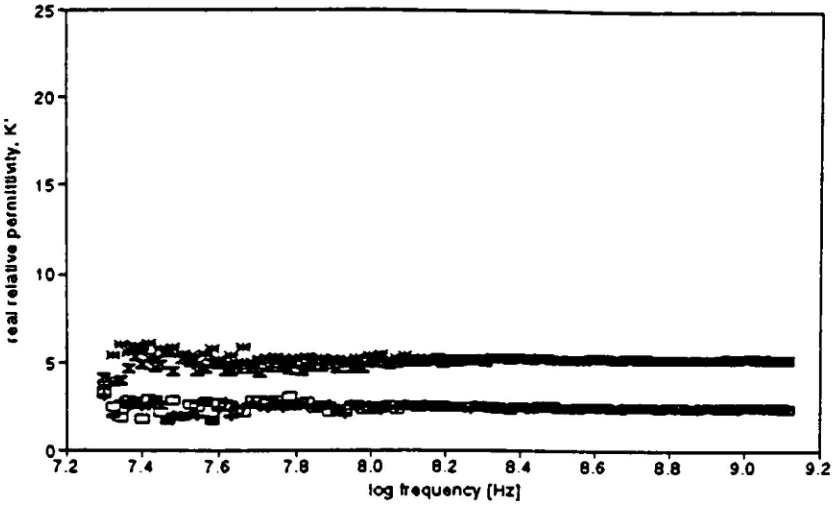
real relative permittivity, K'
25
20
15
10
5
0
7.2
7.4
7.6
7.8
8.0
8.2
8.4
8.6
8.8
9.0
9.2
log frequency [Hz]

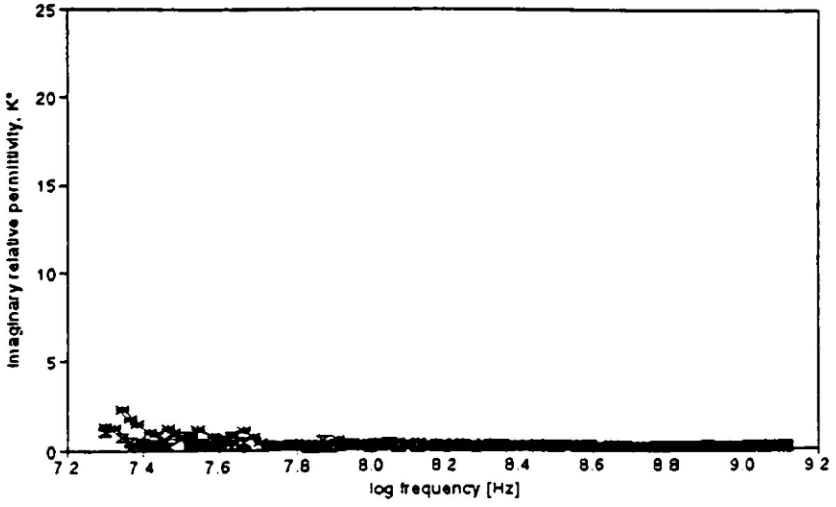
imaginary relative permittivity, K"
25
20
15
10
5
0
7.2
7.4
7.6
7.8
8.0
8.2
8.4
8.6
8.8
9.0
9.2
log frequency [Hz]

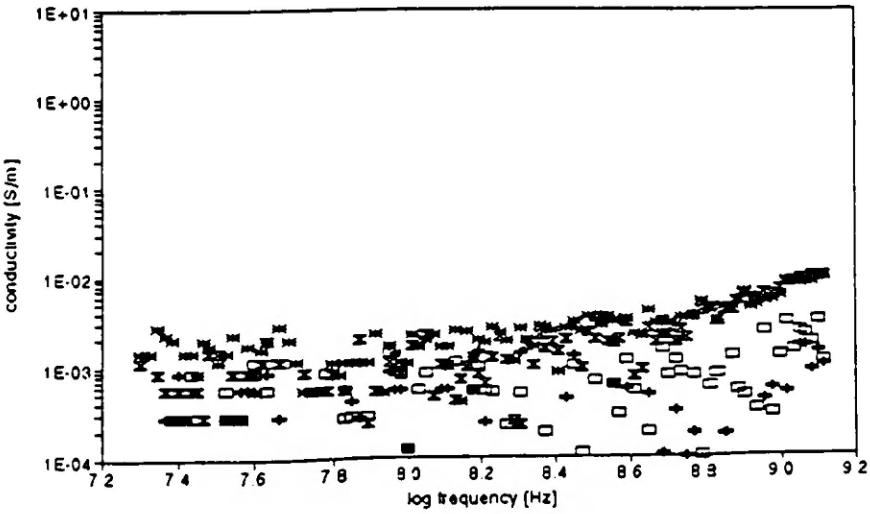
conductivity [S/m]
1E+01
1E+00
1E-01
1E-02
1E-03
1E-04
7.2
7.4
7.6
7.8
8.0
8.2
8.4
8.6
8.8
9.0
9.2
log frequency [Hz]

G9

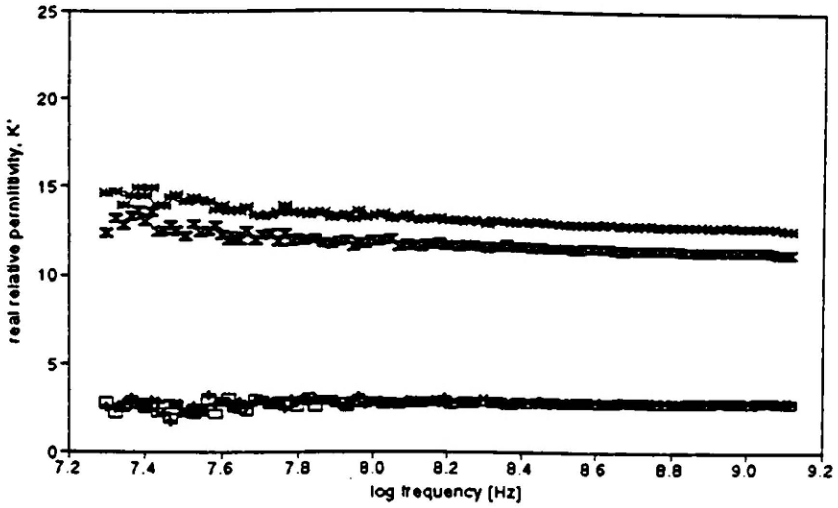
real relative permittivity, K'
25
20
15
10
5
0
7.2
7.4
7.6
7.8
8.0
8.2
8.4
8.6
8.8
9.0
9.2
log frequency [Hz]

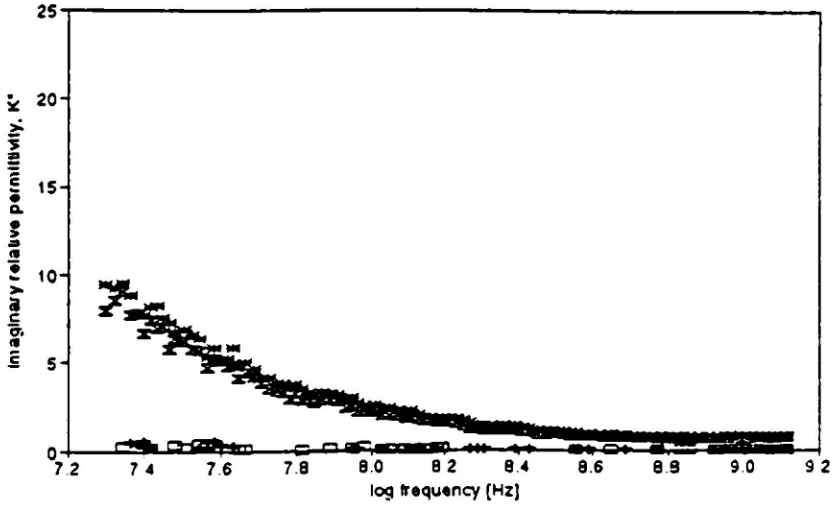
Imaginary relative permittivity, K"
25
20
15
10
5
0
7.2
7.4
7.6
7.8
8.0
8.2
8.4
8.6
8.8
9.0
9.2
log frequency [Hz]

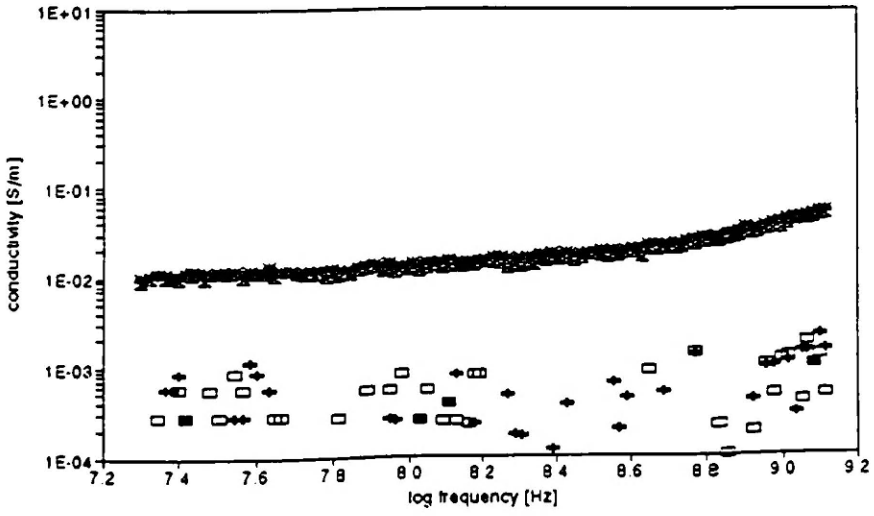
conductivity [S/m]
1E+01
1E+00
1E-01
1E-02
1E-03
1E-04
7.2
7.4
7.6
7.8
8.0
8.2
8.4
8.6
8.8
9.0
9.2
log frequency [Hz]

G10

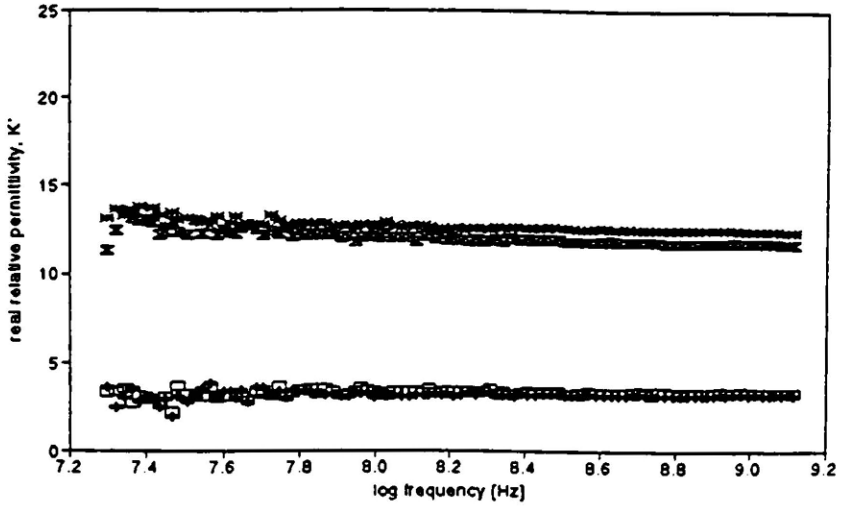
real relative permittivity, K'
25
20
15
10
5
0
7.2
7.4
7.6
7.8
8.0
8.2
8.4
8.6
8.8
9.0
9.2
log frequency [Hz]

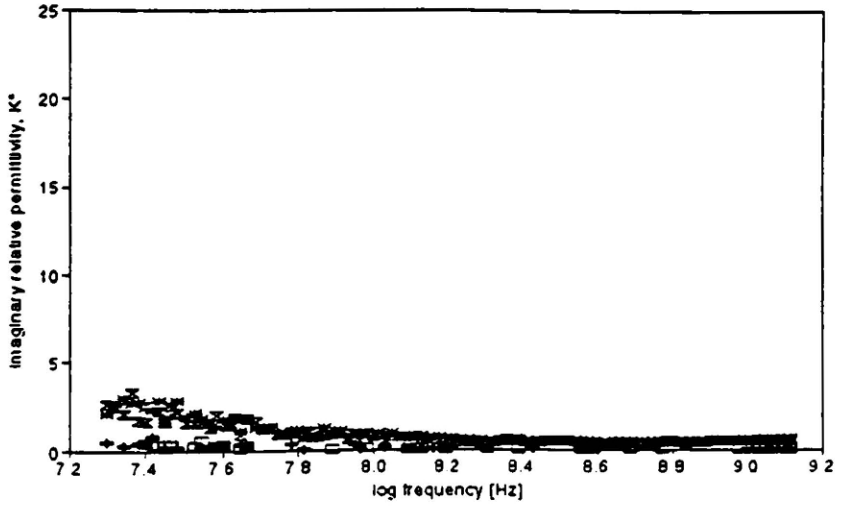
imaginary relative permittivity, K"
25
20
15
10
5
0
7.2
7.4
7.6
7.8
8.0
8.2
8.4
8.6
8.8
9.0
9.2
log frequency [Hz]

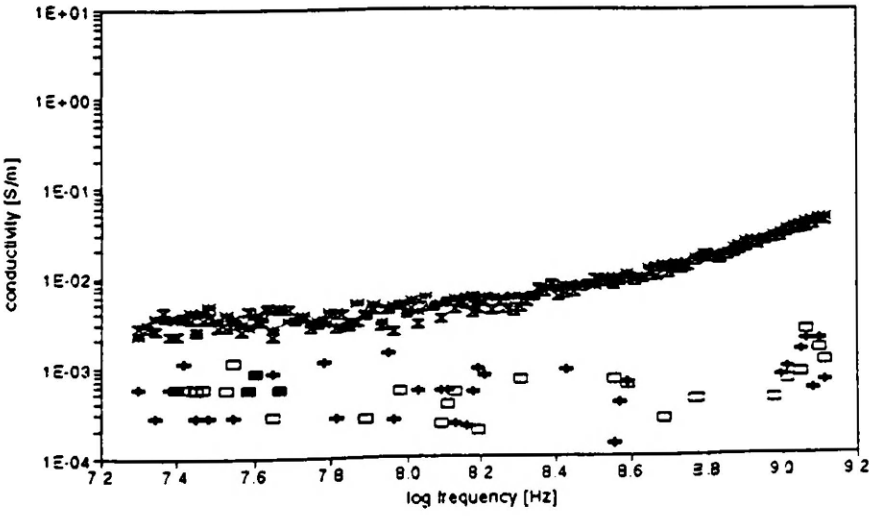
conductivity [S/m]
1E+01
1E+00
1E-01
1E-02
1E-03
1E-04
7.2
7.4
7.6
7.8
8.0
8.2
8.4
8.6
8.8
9.0
9.2
log frequency [Hz]

G11

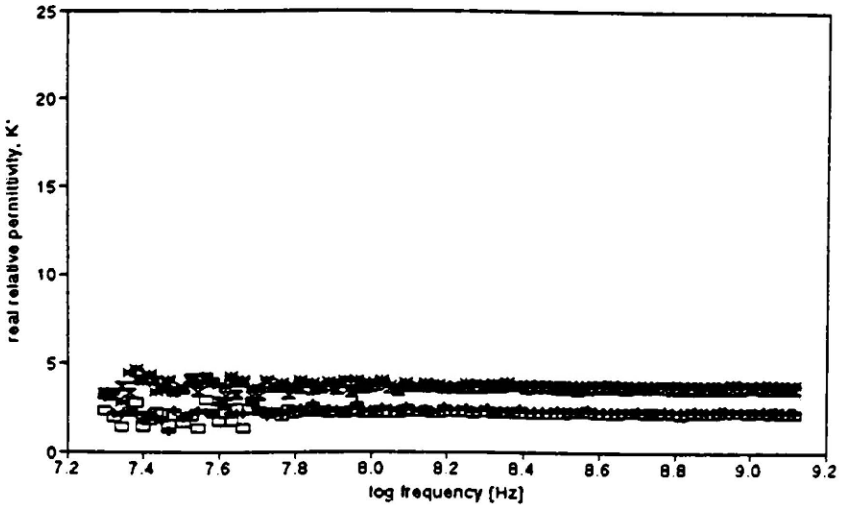
real relative permittivity, K'
25
20
15
10
5
0
7.2
7.4
7.6
7.8
8.0
8.2
8.4
8.6
8.8
9.0
9.2
log frequency [Hz]

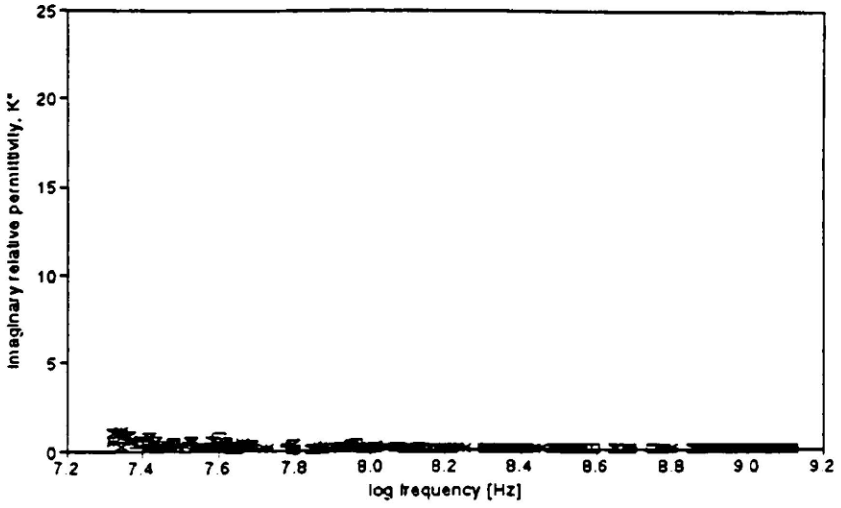
imaginary relative permittivity, K"
25
20
15
10
5
0
7.2
7.4
7.6
7.8
8.0
8.2
8.4
8.6
8.8
9.0
9.2
log frequency [Hz]

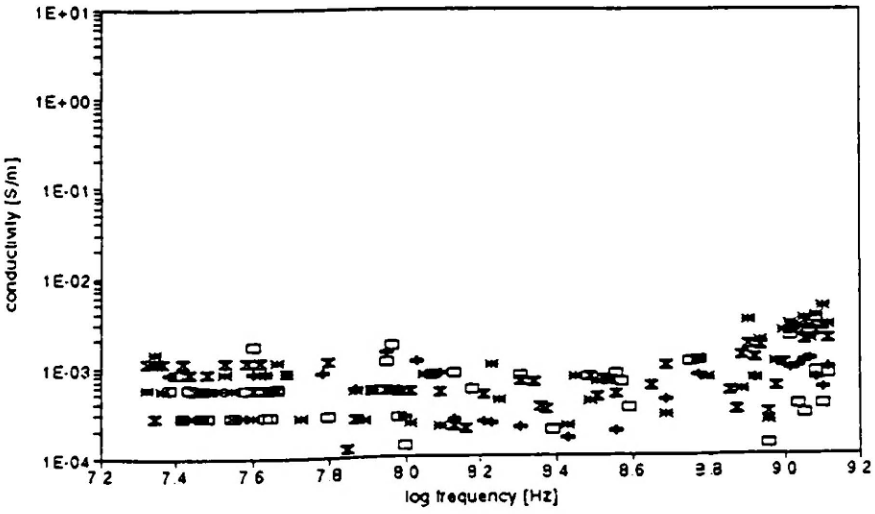
conductivity [S/m]
1E+01
1E+00
1E-01
1E-02
1E-03
1E-04
7.2
7.4
7.6
7.8
8.0
8.2
8.4
8.6
8.8
9.0
9.2
log frequency [Hz]

G12

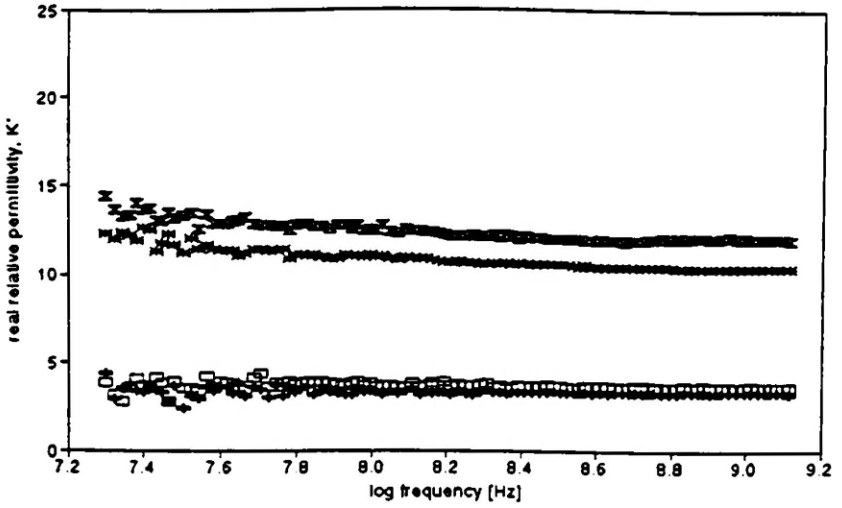
real relative permittivity, K'
25
20
15
10
5
0
7.2
7.4
7.6
7.8
8.0
8.2
8.4
8.6
8.8
9.0
9.2
log frequency [Hz]

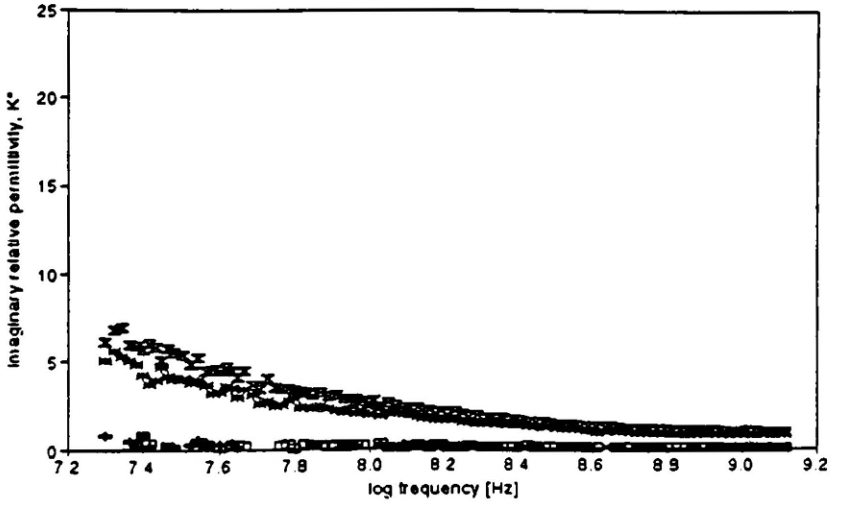
imaginary relative permittivity, K"
25
20
15
10
5
0
7.2
7.4
7.6
7.8
8.0
8.2
8.4
8.6
8.8
9.0
9.2
log frequency [Hz]

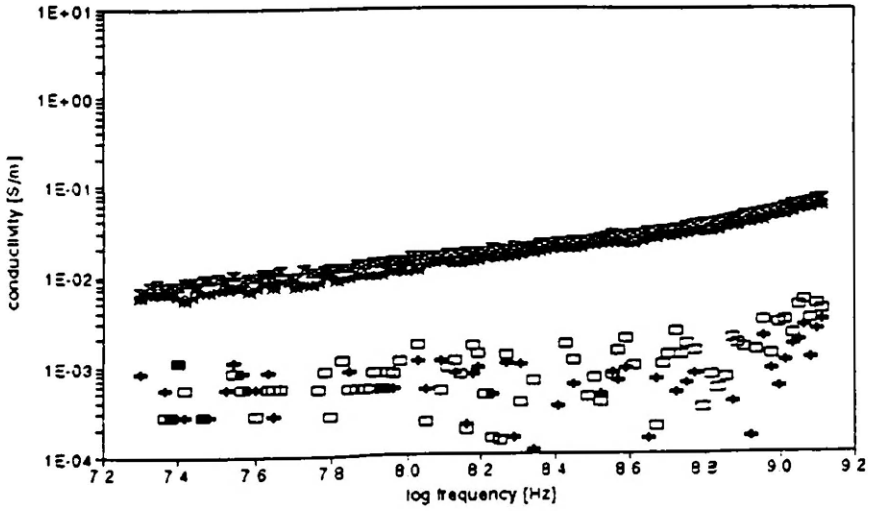
conductivity [S/m]
1E+01
1E+00
1E-01
1E-02
1E-03
1E-04
7.2
7.4
7.6
7.8
8.0
8.2
8.4
8.6
8.8
9.0
9.2
log frequency [Hz]

G13

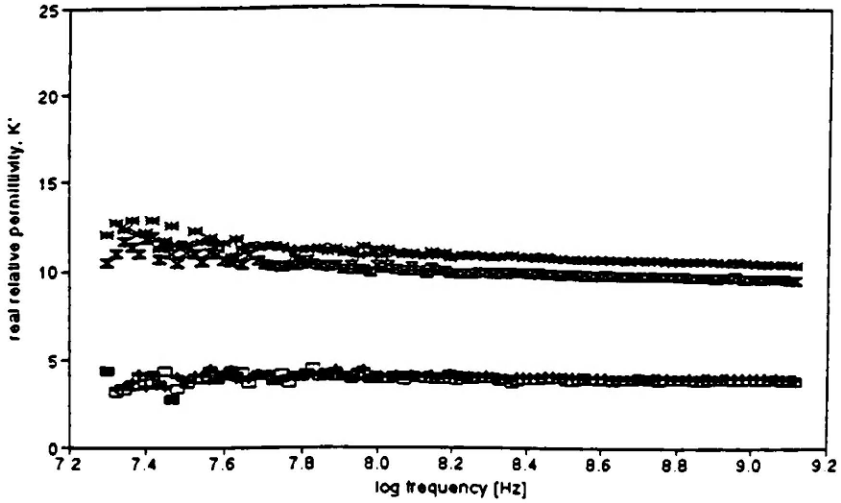
real relative permittivity, K'
25
20
15
10
5
0
7.2
7.4
7.6
7.8
8.0
8.2
8.4
8.6
8.8
9.0
9.2
log frequency [Hz]

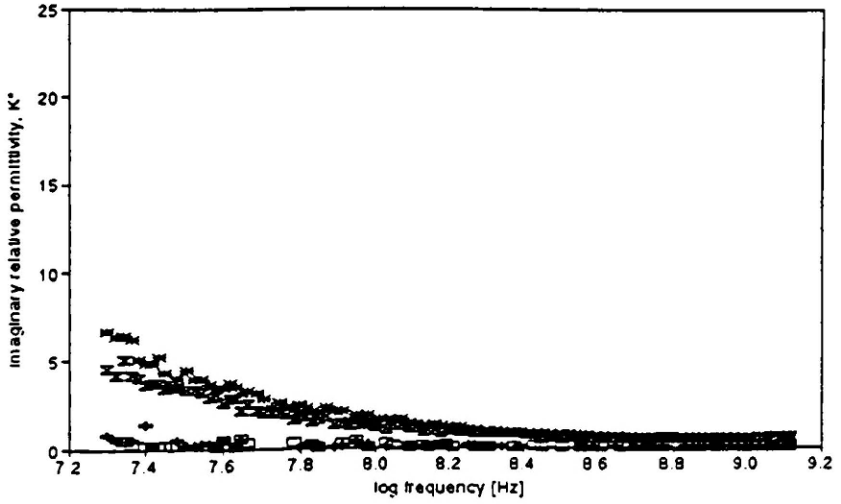
imaginary relative permittivity, K"
25
20
15
10
5
0
7.2
7.4
7.6
7.8
8.0
8.2
8.4
8.6
8.8
9.0
9.2
log frequency [Hz]

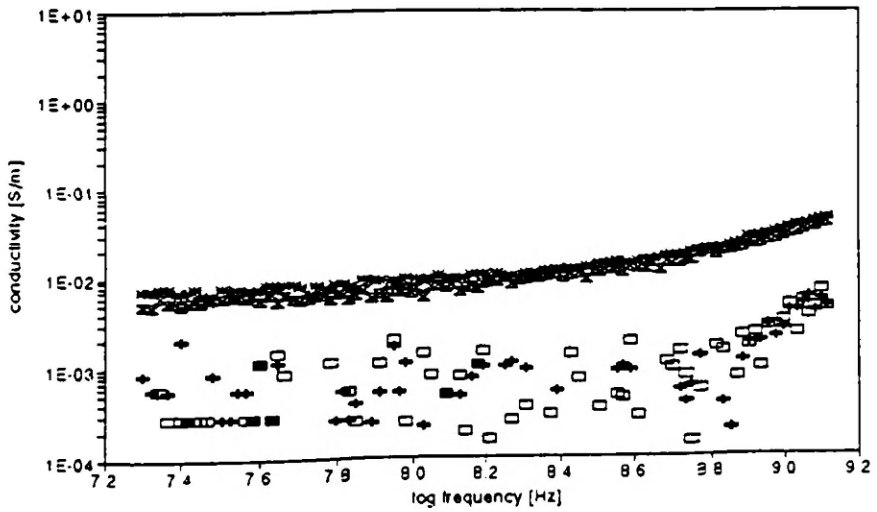
conductivity [S/m]
1E+01
1E+00
1E-01
1E-02
1E-03
1E-04
7.2
7.4
7.6
7.8
8.0
8.2
8.4
8.6
8.8
9.0
9.2
log frequency [Hz]

G14

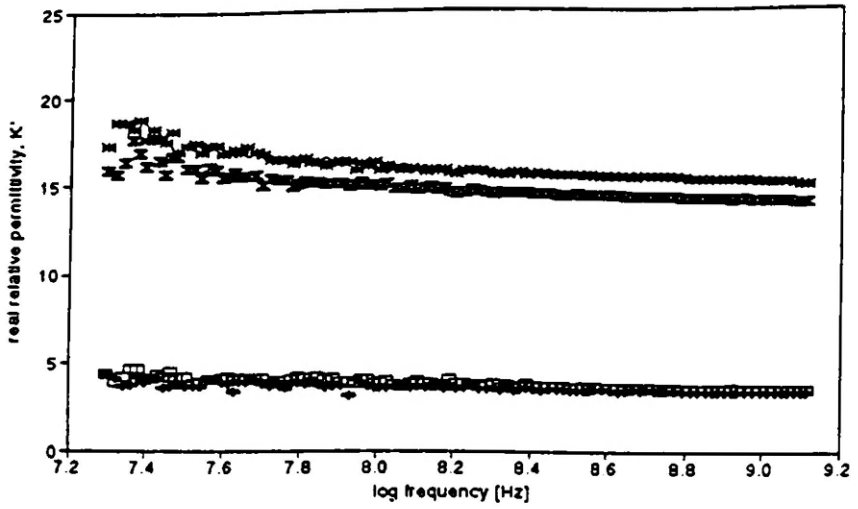
real relative permittivity, K'
25
20
15
10
5
0
7.2
7.4
7.6
7.8
8.0
8.2
8.4
8.6
8.8
9.0
9.2
log frequency [Hz]

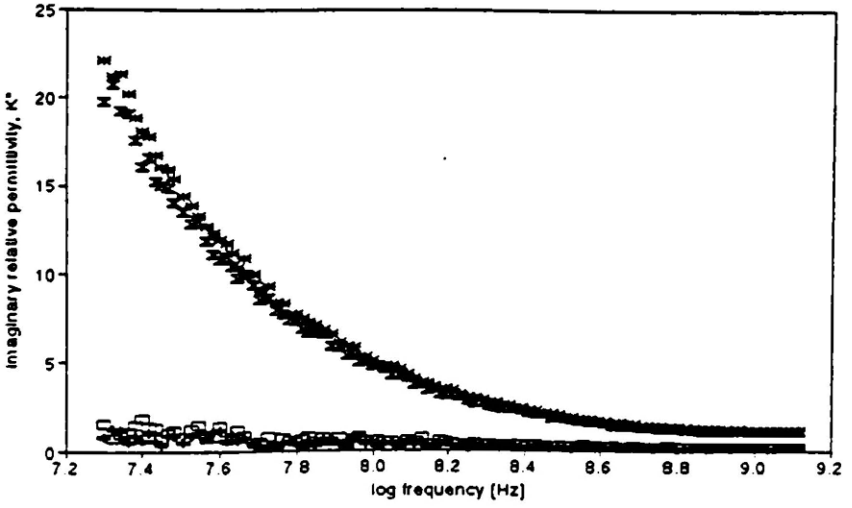
imaginary relative permittivity, K"
25
20
15
10
5
0
7.2
7.4
7.6
7.8
8.0
8.2
8.4
8.6
8.8
9.0
9.2
log frequency [Hz]

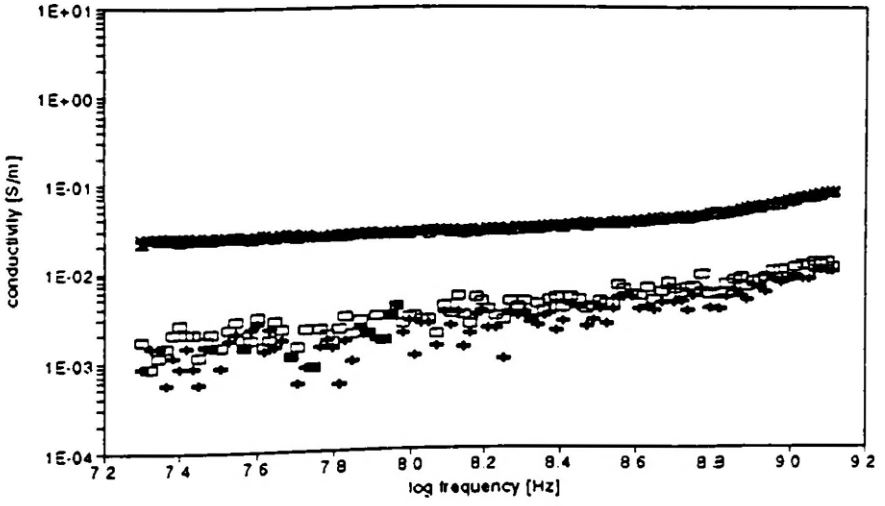
conductivity [S/m]
1E+01
1E+00
1E-01
1E-02
1E-03
1E-04
7.2
7.4
7.6
7.8
8.0
8.2
8.4
8.6
8.8
9.0
9.2
log frequency [Hz]